RESIDUAL GAS ANALYSIS USING MINIATURE QMS SYSTEMS

Thesis submitted in accordance with the requirements of the University of Liverpool for the degree of Doctor in Philosophy

By

Neil France

20 February 2009

Residual Gas Analysis using miniature QMS systems

ABSTRACT

Recent trends in miniaturisation have resulted in many of the more common forms of mass spectrometer being made available in reduced sizes. This is because reduction in size of analyzers offers several advantages including lower manufacturing costs, the possibility of operation at higher pressures (due to shorter length of the ion mean free path), lower power consumption for RGA systems with possibility of battery operation, the potential for the whole mass spectrometry system (mass spectrometer and associated vacuum system) to be portable.

In this thesis the miniaturisation of a quadrupole mass spectrometer is specifically considered. A major application area for such an instrument is in the field of residual gas analysis (RGA) and this is the principle application of the portable QMS systems investigated. The problems of miniaturisation include the need for improved ion source design and efficiency due to the difficulty of coupling ions into a miniature quadrupole mass filter (QMF).

Ion source simulation tools (CPO and SIMION) are compared and evaluated. For the design of the miniature EI source, SIMION was preferred. Stable and controlled electron emission from carbon nanotubes was achieved which allows the possibility of a low power cold cathode source, however stable ion production and optics proved to be problematic.

Smaller QMS systems require the use of specialist electronic control units and the development of use of such an ECU is described. Alternative methods of QMF realisation are described including wire cut (EDM) and digital light processing (DLP) to produce miniature hyperbolic form mass filters which were then fabricated and tested. Tests using a portable commercial QMS system and novel methodology for heliobacter pylori detection were successfully performed in patient trials in conjunction with the Royal Liverpool University Hospital (RLUH). Finally, conclusions and suggestions for future work and are made.

ACKNOWLEDGMENTS

I would like to thank all the people who have helped and inspired me during my doctoral study.

I especially want to thank my supervisor Dr. Steve Taylor for his guidance and support and for the opportunity to work on this interesting topic.

I would also like to thank Tom Hogan for his help and advice and Dr Boris Brkić for his time spent proof reading my chapters and Paul Aden for his help working with carbon nanotubes.

Also it's been great working with SS Scientific my industrial sponsor, and I would like to thank Robin, Jane, Steve, Antony and Nicol for making me feel welcome during my visits.

Financial support from the Engineering and Physical Sciences Research Council (EPSRC) is also gratefully acknowledged.

Finally, I would like to thank my family for their continuous support and encouragement.

20 February 2009

Neil France

LIST OF ABBREVIATIONS

BEM	Boundary Element Method
CCP	Capacitively Coupled Plasma
CEM	Channel Electron Multiplier
CI	Chemical Ionisation
CVD	Chemical Vapor Deposition
DLP	Digital Light Processing
EDM	Electro Discharge Machining
EI	Electron Impact
ESI	Electrospray ionisation
FDM	Finite Difference Method
FEM	Finite Element Method
ICP	Inductively Coupled Plasma
MEMS	Micro Electro Mechanical Systems
RGA	Residual Gas Analysis
QMF	Quadrupole Mass Filter
QMS	Quadrupole Mass Spectrometry

CONTENTS

Introduction

Residual Gas Analysis (RGA) is an analytical technique used for identifying the gases present in vacuum systems and environments. The most commonly used RGA is the quadrupole mass spectrometer (QMS), though other forms of mass spectrometer (e.g. magnetic sector instruments) are also used. Miniaturised (including microengineered) versions of RGA's have been developed in recent years and are finding increased application in field conditions and in harsh environments (e.g. spacecraft) where low power, low weight and portability are key requirements.

The quadrupole mass spectrometer operates by creating a beam of ions from samples of the gas being analysed. The resulting mixture of ions are then separated into individual species through their charge-to-mass ratios. To accomplish these, a typical QMS has three major parts, namely, an ionizer, a mass analyzer, and an ion detector. The output of an QMS is a spectrum that shows the relative intensities of the various species present in the gas. This output is known as a mass scan or mass spectrum. An introduction to the QMS is given in Chapter 1 with a more detailed description of operation (including mathematical description) is presented in Chapter 3. The molecules of the gas being analysed in the RGA are ionised in the ion source. Ionisation may be accomplished through a variety of different methods and techniques. These are reviewed and compared in Chapter 1.

Simulation of component parts of the RGA is extremely important and in Chapter 2, two commercial simulation packages are investigated: SIMION and CPO. The two packages investigated use two different methods to calculate ion trajectories under the influence of electrostatic and electromagnetic fields and they can be applied to ion sources, ion traps and RF quadrupole mass filters. SIMION uses the Finite Difference Method (FDM) while CPO uses the Boundary Element Method (BEM). The mathematics underlying FDM and BEM are described in Chapter 2. Both programs where used to obtain ion trajectories of a single trapped

ion in an endcap ion trap, these trajectories are then used to calculate ion secular frequencies which are compared to previously measured (and published) values and thus allow evaluation of the packages. Using the SIMION package a 4 plate electron impact (EI) ion source suitable for coupling to a miniature QMS was designed, optimised and tested.

Chapter 3 introduces the Quadrupole Mass Filter (QMF) and explains its operation and the underlying mathematical equations used to describe electromagnetic fields produced in the ideal (hyperbolic field) case. Ion stability within QMF is discussed in terms of the Mathieu Stability Diagram and how this relates to instrument sensitivity and resolution. An in-house custom software simulation program (QMS2-Hyperbolic) was used to simulate ion trajectories in a QMF, and to further optimise ion source design for highest resolution and transmission. The 4 plate ion source designed in Chapter 2 was coupled to a miniature hyperbolic QMF constructed using Electro Discharge Machining (EDM) and a second QMF that was constructed using Digital Light Processing (DLP). Mass spectra from QMS instruments constructed using these two novel QMF assemblies are described.

In Chapter 4 a novel method of electron emission using deposited Carbon nanotubes is investigated. This method has the potential to replace an electron impact ion source with a cold cathode source which operates at lower power and is thus to be preferred for miniature and/or field portable RGAs. The results obtained and problems entailed with this approach are described.

In Chapter, 5 a commercially available portable QMS RGA system used for a novel medical application is described and documented. The tests were conducted on a number of patients at the Royal Liverpool University Hospital over a period of 4 months from August 2007. The RGA is used to detect Helicobacter pylori, a microaerophilic bacterium that inhabits various areas of the stomach and duodenum and is indicative of the presence of a gastric or duodenal ulcer.

Discussion of the results obtained and conclusions drawn are undertaken throughout the thesis but these are brought together and summarised in Chapter 6 and some suggestions for further work and study are made. A list of the publications arising from or in conjunction to the work described is included. Finally a comprehensive set of appendices giving further details of the electronics and computer programs used is also provided.

Chapter 1

Mass Spectrometry

1.1 Introduction to Mass Spectrometry

Mass spectrometry is an analytical technique, widely used in chemistry, biochemistry, physics and the medical field. It operates by separating atomic and molecular ions according to their mass-to-charge ratios (m/z). The mass of an ion m is usually given in Daltons (Da) or atomic mass units (amu), where 1 Da = 1 amu = $1.6605402 \times 10^{-27}$ kg. The total charge of an ion q is expressed by the formula $q = ze$, where z represents the number of electron charges of an ion and e is the electron charge ($e = 1.60217653 \times 10^{-19}$ C) [1].

A mass spectrometer consists of four main components, which are:

1. Inlet – allows atoms and molecules from the sample to enter the ionisation source.
2. Ion source – creates atomic and/or molecular ions.
3. Mass analyser or filter – for separation of ions according their mass-to-charge ratio.
4. Detector – detects the quantity of ions passing through the mass spectrometer, usually by measuring the ion current at a given mass/charge ratio.

The sample to be analysed is introduced via a suitable inlet into the ion source. The ion source then creates ions from the neutral atoms of the sample using different methods of ionisation. Commonly used ionisation methods are: electron impact (EI) ionisation, chemical ionisation (CI), electrospray ionisation (ESI), capacitively coupled plasma (CCP), and inductively coupled plasma (ICP).

After the ions have been created in the source they are injected into the mass analyser where the ions are separated according to their mass-to-charge ratios using one of the following methods: electric field, magnetic field or time of flight necessary for a given ion to pass a certain distance. Since the pioneering work of Paul [2], the quadrupole mass filter (QMF) is widely used and separates ions based on their mass-to-charge ratios (m/z) and the stability of the trajectories in an applied radio-frequency (RF) and DC electromagnetic field. A review of quadrupole mass spectrometry up to 1976 is given by Dawson and this still provides a standard reference text [3]. A survey of quadrupole ion trap mass spectrometry to 2005 is provided by Wineforder [4]

The final step is the detection of ions successfully transmitted through the mass filter. Commonly used methods to achieve this are: Faraday cups, electron multipliers, and photon multipliers. In the case of Faraday detection each ion passing through the mass filter produces a corresponding electron as it strikes the detection plate which is usually configured in the form of a cup or bucket to aid ion collection. In a multiplier detector, each ion passing through the mass filter strikes and enters a channel electron multiplier (CEM). This is a hollow horn-shaped tube made of a proprietary semiconducting glass coating as shown in Figure 1.1

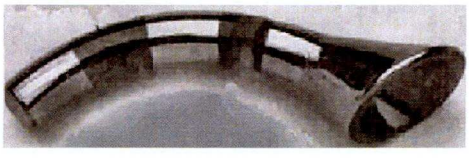

Figure 1.1: Channel Electron Multiplier (photo courtesy of Detech Inc)

This type of multiplier uses a process known as secondary electron emission. The surface of the device is coated with a material such that when ions strike the surface secondary electrons are released. The number of secondary electrons released depends on several factors, such as the type of ions, the angle at

which they strike the surface, their energy, and most importantly the characteristics of the surface coating.

The secondary electrons are then accelerated through an electric field, which is generated by applying a voltage of the correct polarity to the surface of the tube. The electric field causes the secondary electrons to collide with the CEM tube walls, and these electrons in turn cause further electron emission. The result is an avalanche of electrons at the collector which is responsible for the detector gain.

1.2 Comparison of ion sources

A good review of the many different types of ion source is provided by Wolf [5]. A description of those types of ion source which are most relevant to residual gas analysis (RGA) and miniature QMS is given below.

1.2.1 Electron Impact ionisation

Electron Ionization (EI) also known as electron impact ionization is one of the oldest ionization methods and has been extensively studied [5, 6]. A schematic diagram of a typical EI source is shown in Figure 1.2.

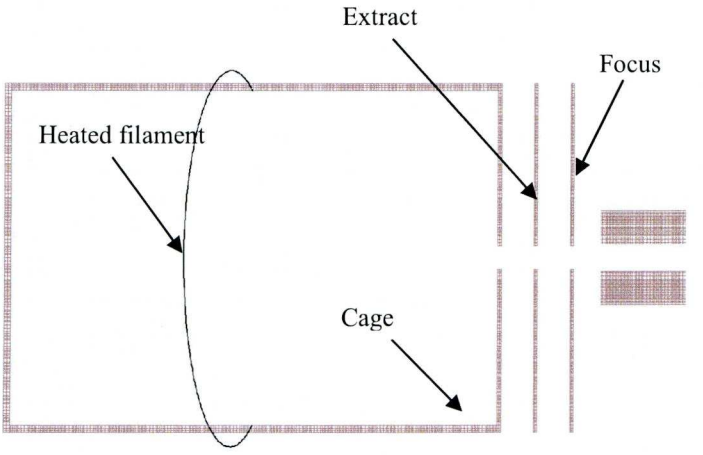

Figure 1.2: Electron impact ionization source

In a typical EI source an electrically heated filament (e.g. tungsten or thoria) thermionically emits high energy electrons. Thermal electron emission from a metal surface can be described by the Richardson-Dushman equation:

$$J = CT^2 \cdot \exp\left(-\frac{\Phi}{kT}\right) \tag{1.1}$$

where J is the current density of emitted electrons, C a constant (independent of the filament material), T the temperature and Φ the work function of the filament material. The temperature of the filament is typically in the region of 2500 K. The emitted electrons have a kinetic energy distribution of around 1-2eV due to the filament temperature and the electrical potential applied to the heated filament. Therefore after acceleration to 70eV the ionising electrons have a kinetic energy of 70 ± 1eV. These high energy electrons are accelerated into the gas region inside the cage and collide with the neutral (sample) gas molecules. Since the energy of these electrons is greater than the binding energy of electrons in the neutral gas atoms than on collision, electrons will be removed from the neutral gas, resulting in positive ion formation. Usually the ion will be singly charged, but electron impact with sufficient energy can also generate ions with multiple charges. Since the states

of electrons in an atom or molecule are to some extent correlated, the colliding or outgoing electron can interact with further electrons and cause the removal of more than one electron. The probability of multiple ionization, however, is usually only a few percent compared to single ionization, as shown in figure 1.3.

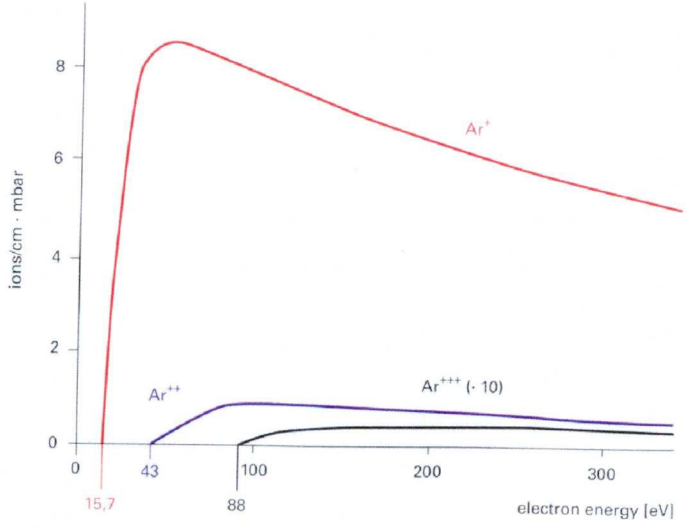

Figure 1.3: Ionisation of Argon by electron impact as a function of incident electron energy [7].

The cage within the ion source is at a positive potential with respect to the filament and it's this potential which determines the energy of the ions produced and subsequently enter the mass filter.

The number of ions produced by electron impact ionization depends mainly on the number and energy of the ionising electrons, the type and concentration (pressure) of sample gas atom/molecules present. The ionization potential of each gas species determines the minimum energy the bombarding electrons must have to remove an outer electron. The ionisation cross section is a measure of the ionisation probability, it may be thought of as an effective area of the atom or molecule in which impact occurs. For example if an electron collides inside this area, ionisation

takes place, while for a collision outside this is not deemed to be the case. The resulting ion current may be given by:

$$i_k^+ = i^- \cdot I \cdot s \cdot p_k \quad [A] \tag{1.2}$$

where

i^- = Electron (emission) current [A]

I = Mean free path of the electrons [cm]

s = Differential ionization of the gas $\frac{1}{[cm \cdot mbar]}$

P_k = Partial pressure of species k [mbar]

It can be seen from Figure 1.3 that the cross section for single ionisation begins at 15.7eV increases up to a value around 50eV and then decreases. This curve represents the ionisation efficiency as a function of the collision energy and is called an ion yield curve. The ionisation cross section at 50eV roughly corresponds to the actual geometrical cross section of the molecule.

The decrease at higher energy is simply a consequence of the fact that the energy of the primary electrons differs from the energy of the outer electrons in the target, resulting in a less effective interaction. Most molecules have maximum ionisation cross sections near 50-55eV. For that reason most EI sources usually operate at 65-70eV electron impact energy. Typical EI sources operate in the pressure range 10^{-4} to 10^{-10} mbar and can produce ion currents in the order of 1mA of ion current at operating powers of less than 10W. They are widely used in residual gas analysers (RGA) and QMS, and quadrupole ion trap instruments.

1.2.2 Plasma ion sources

1.2.2.1 Capacitively coupled ion sources

In a capacitively coupled ion source a plasma of ionized gas is excited and sustained by applying an RF voltage between the two electrodes. The term capacitively coupled plasma comes from the way the energy is coupled into the plasma. The plasma forms "sheaths", regions of very low electron density near solid surfaces. The RF voltage appears mostly across these sheaths as if they were the dielectric region of a capacitor, with the electrode and the plasma forming the two plates [8-9].

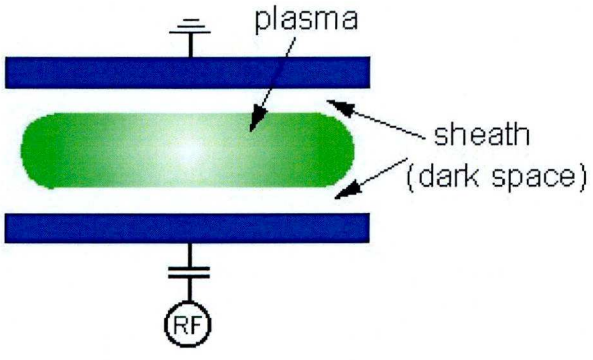

Figure 1.4: Capacitively coupled plasma schematic [9].

To sustain the plasma, electrons must be generated at a rate which is large enough to offset the loss of electrons to the chamber walls, recombination with positive ions and/or electron attachment reactions. Another mechanism which generates electrons is bombardment of the electrode surfaces by energetic particles (ions or electrons), which causes high energy secondary electrons to be ejected back into the plasma [9].

The system pressure is typically between about 0.133 mbar and 13.3 mbar. The electrode "gap" is an important parameter; it varies from about 0.5 cm to 10 cm, generally getting smaller for higher pressure operation. Typical gaps are a few hundred times the mean free path, so electrons undergo many collisions but do not

have time to transfer their energy to the neutral gas. However, practical limitations on chamber size generally lead to increasing ratios, and "hotter" plasmas at higher pressures [10].

The voltage necessary to initiate a discharge is a function of the product of the spacing between electrodes and the pressure (Paschen's Law) [11]. The law essentially states that at higher pressures (above a few mbar) the breakdown characteristics of a gap are a non linear function of the product of the gas pressure and the gap length, usually written as V= f(*pd*), where *p* is the pressure and *d* is the gap distance. Extensive additional experiments for different materials, lower pressures, different gases and a variety of electrode shapes have been carried out. The Paschen curve in air for two flat parallel copper electrodes for pressures between $4x10^{-2}$ mbar and 800 mbar is shown in Figure 1.5. As the pressure is reduced below a few mbar the curve of breakdown voltage versus pressure reaches a minimum, and then, as pressure is further reduced, rises steeply again.

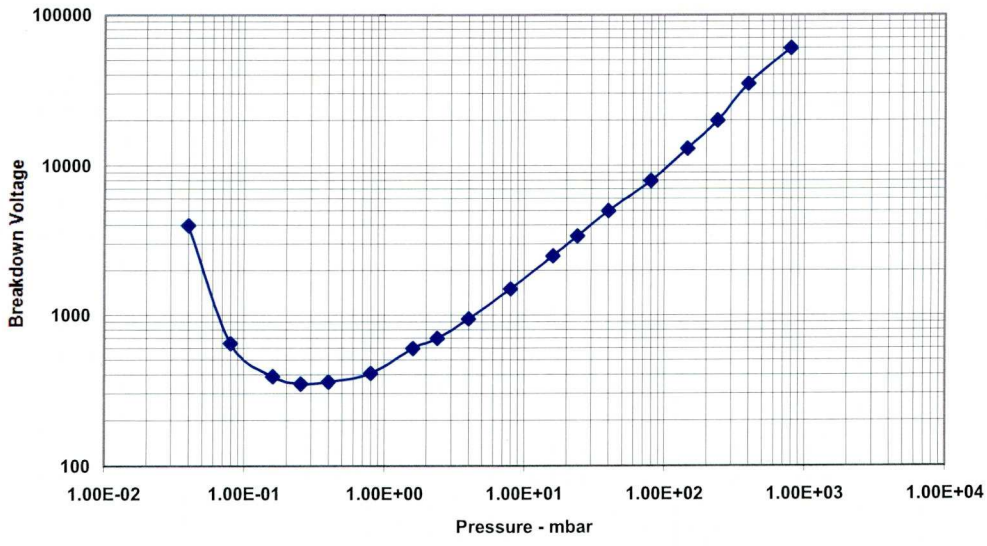

Figure 1.5: Paschen curve showing breakdown voltage for air for a gap of 2.54cm versus pressure [11].

At higher pressures, the discharge voltage increases, making it difficult to start the plasma if the electrode spacing is large. At very low pressure (or more properly pressure-distance product), there are too few collisions and electrons traverse the chamber and strike the walls without causing ionization. Again the voltage for initiating the discharge increases. For typical chamber geometries, it is very difficult to initiate a capacitive discharge at pressures less than 13-20 mbar, though it is often possible to "strike" the discharge at higher pressure and then operate at only a few mbar. This high breakdown voltage is exploited in making dark space shields, grounded plates placed within a few mm of a powered electrode to localize the plasma above the electrode [12].

The plasma is sustained by hot electrons which strike molecules to knock off another electron, creating an ion. At very low frequencies (<10 KHz) the mechanism for creating these hot electrons is very similar to that operating in DC plasmas, where the large sheath voltage present at the cathode accelerates the secondary electrons, which gain enough energy to ionize molecules in the plasma. This is an inefficient process since very large sheath voltages (400-700 V) are required, and much of the electron energy is dissipated in non-ionizing collisions [12].

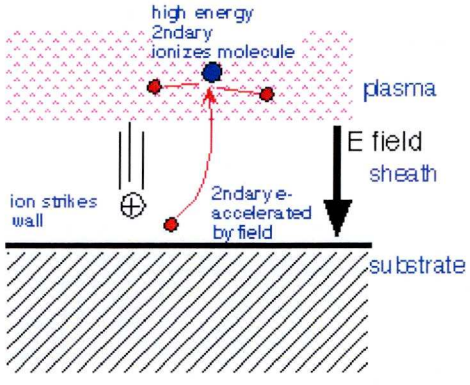

Figure 1.6: Diagram showing plasma sheath [12].

As frequency increases into the MHz range, two new mechanisms for transferring energy to electrons become important. First, the change in sheath sizes with each RF cycle requires that charge move back and forth through the plasma, therefore a displacement current flow must exist. This displacement current, like any other current, encounters some resistance as it flows in the plasma, and leads to a voltage and thus heat dissipation. Since the current is proportional to frequency, and the power is proportional to the square of the current, the amount of power dissipated scales as the square of the frequency [12].

1.2.2.2 Inductively coupled plasma

When a solenoidal coil is wrapped around a dielectric chamber (e.g. a quartz tube), and an RF voltage is applied, the current flow in the coil generates a magnetic field in the vertical (z) direction:

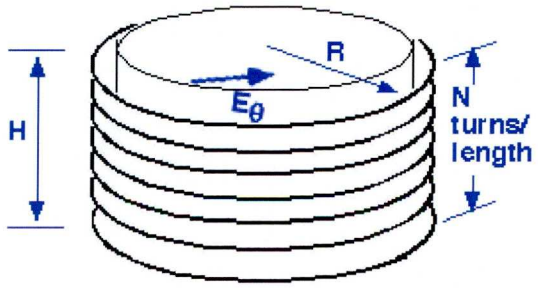

Figure 1.7: Inductively coupled plasma source [12].

This time-varying magnetic field creates a time-varying azimuthal electric field (wrapping around the axis of the solenoid). The field strength is proportional to the radial distance and the frequency.

The azimuthal electric field induces a circumferential current in the plasma. The electrons thereby accelerated gain energy, creating enough hot electrons to create and sustain plasma through ionization [13-15].

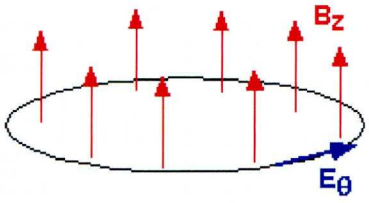

Figure 1.8: Field lines of an inductively coupled plasma source [12]

Once the plasma forms, the magnetic fields are screened by the induced currents, just as in a metal, in operation, the magnetic field penetrates into the chamber to a depth determined by the magnetic skin depth, which is in turn set by the plasma conductivity and thus by the plasma density and the pressure [16].

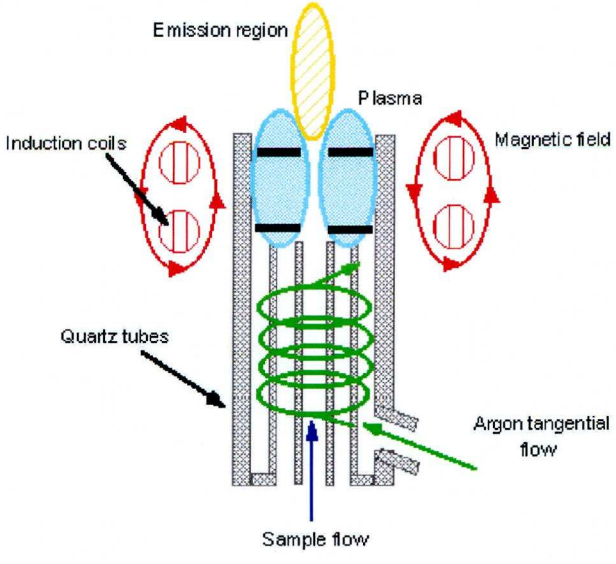

Figure 1.9: Inductively coupled plasma (ICP) torch [16].

The ICP plasma torch consists of three concentric quartz tubes; the outer tube, middle tube and sample injector. The torch can either be one piece with all three tubes connected, or it can be a demountable design in which the tubes and the sample injector are separate. In order to prevent short-circuiting as well as meltdown the plasma is insulated from the quartz tubes by the continuous flow of gases through the system.

The outer gas, normally Argon or Nitrogen flows between the outer and middle tubes at a rate of 12–17 L/min, this gas is used to maintain the plasma and thermally isolate the plasma from the outer tube. A second gas flow passes between the middle tube and the sample injector at rate of 1 L/min, this is called the auxiliary gas flow, and its purpose is to change the position of the base of the plasma relative to the tube and the injector. A third gas flows inside the sample injector also at a rate of 1 L/min, this flow carries the sample, in the form of a fine-droplet aerosol to the centre of the plasma [17, 18].

A spiral flow of argon gas is directed between the outer and middle tube of ICP quartz torch. A load coil, usually copper, surrounds the top end of the torch and is connected to a radio frequency generator. When RF power (typically 750–1500 W, depending on the sample) is applied to the load coil, an alternating current oscillates within the coil at a rate corresponding to the frequency of the generator. In most ICP generators this frequency is either 27 or 40 MHz. This RF oscillation of the current in the coil produces an intense electromagnetic field at the top of the torch.

Initially, in an ICP system there are no free electrons to respond to the induced electric field so a high voltage spark is applied to the gas, which causes some electrons to be stripped from their argon atoms. These electrons are then accelerated in the magnetic field and collide with other argon atoms and cause a chain reaction where more argon atoms are ionized and more electrons are produced, which forms the inductively coupled plasma discharge. The ICP

discharge can then be sustained as long as the RF energy is continually transferred to it through the inductive coupling process and the gas flow is maintained [17].

The more important consideration is the coupling efficiency of the RF generator to the coil. The majority of modern solid-state RF generators are on the order of 70–75% efficient. Some of the older vacuum tube–designed generators were notoriously inefficient, experiencing more than a 50% power loss. Another important criterion to consider is the way the matching network compensates for changes in impedance produced by the sample matrix components. In older crystal-controlled generators, this was usually done with servo driven capacitors. They worked very well with most sample types, but because they were mechanical devices, they struggled to compensate for very rapid impedance changes produced by some samples. As a result, the plasma was easily extinguished, particularly during aspiration of volatile organic solvents. These problems were partially overcome by the use of free-running RF generators, in which the matching network was based on electronic tuning of small changes in frequency brought about by the sample solvent or matrix components. The major benefit of this approach was that compensation for impedance changes was virtually instantaneous because there were no moving parts. This allowed for the successful analysis of many sample types that would probably have extinguished the plasma of a crystal-controlled generator [15].

1.2.3 Cold cathode ion sources

Rather than using a cathode that is heated to induce thermionic emission of electrons, a cold cathode source takes advantage of field emission which is a mechanism for generating free electrons from a cold metallic (or semiconducting) surface. If a sufficiently high field is applied then electrons can overcome the work function of the cathode material and be extracted from their atomic orbitals and emitted. An early form of mass spectrometer with a spark gap ion source has been reported [21]. The spark was formed by both an RF and high voltage DC generated

discharge. Cold cathode ion sources have also been used recently for low power and/or miniature ion sources [19-20].

Such sources cannot operate if the ions generated by the cathode recombine before reaching the anode target. If the mean-free path of the gas within the gauge is smaller than the source dimensions, then the electrode current will essentially vanish. A practical upper-bound to the operating pressure of such sources is of the order of 10^{-2} mbar.

Similarly, cold cathode sources may be reluctant to start at very low pressures (10^{-9} mbar). This because the near-absence of a gas makes it difficult to establish an electrode current. Cold cathode electrodes are usually finely tapered to facilitate the field emission of electrons. Many of the approaches to achieve this are based on photolithography and micromachining fabrication in order to achieve the desired electrode separation. Most are in the experimental stage and some are proprietary. A recent method that is being explored is to fabricate arrays of sharpened silicon whiskers that have been coated with diamond deposited by CVD [19].

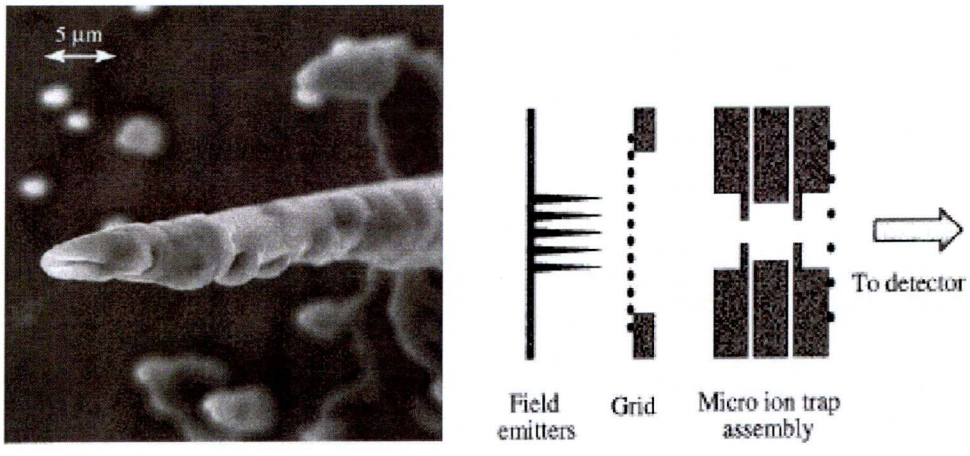

Figure 1.10 Scanning Electron Micrograph of a diamond coated silicon whisker (left) and schematic diagram of a cold cathode ion source [19](right).

Close to the tips of the whiskers, electrons can be extracted from the whiskers and currents greater than 1 μA/tip have been reported with a threshold external electric field as low as 1.5 $V\mu m^{-1}$. The whiskers have been grown in random arrays or with regular spacing with separations from 16 to 100 μm.

The theoretical basis for electron emission from diamond in general and from diamond-coated whiskers is still controversial. The negative electron affinity of hydrogen-passivated diamond surfaces undoubtedly is important in reducing the threshold field [19]. Other forms of carbon electrodes such as nanotubes, and diamond-like carbon also show field emission behavior and this will be revisited in a later chapter.

1.3 Miniaturisation of mass analyzers

Miniaturisation of mass analyzers is usually done by using microelectromechanical systems (MEMS) technology, which is mainly based on semiconductor microengineering with metal deposits. Since complex electrode geometries like hyperbolic cannot be machined at micro-scale using MEMS, simpler geometries like cylindrical and planar are used to give an approximation to the ideal hyperbolic field. One of the first miniature analyzers constructed using MEMS was a quadrupole mass filter (QMF) with cylindrical electrodes [22]. Other successfully built miniature mass analyzers include time-of-flight mass filter [23] and several types of ion traps: cylindrical micro ion traps that can easily form arrays [24–26], rectilinear ion trap with planar electrodes [27] and halo ion trap [28]. The final goal in much of this research is a reliable and fully integrated mass spectrometer with all of its components built as one part. Significant progress has already been made in that direction with building a time-of-flight mass spectrometer on a chip [23].

References

[1] P. J Mohr and B. N. Taylor, *CODATA recommended values of the fundamental physical constants 1998*, *Rev. Mod Phys.*, **72**, (4), 351 (2000) and http://www.kayelaby.npl.co.uk/units_and_fundamental_constants/1_2/1_2_3.html

[2] W. Paul and H. Steinwedel, *Ein neues Massenspektrometer ohne* Magnetfeld *Z. Naturforschung,* **8a** , 448 (1953).

[3] P.H. Dawson, *Quadrupole Mass Spectrometry and its Applications.* Elsevier, Amsterdam, (1976).

[4] J.D. Wineforder (Editor), *Quadrupole Ion Trap Mass Spectrometry,* Hoboken, NJ, (2005).

[5] B. Wolf (Editor), *Handbook of Ion Sources,* CRC Press, (1995).

[6] I.G. Brown (Editor), *The Physics and Technology of Ion Sources*, Wiley VCH (2005).

[7] Pfeiffer Vacuum Manual, pg 12, (2002-2004)

[8] Daniel M. Dobkin - Capacitive Plasmas http://www.batnet.com/enigmatics/semiconductor_processing/CVD_Fundamentals/plasmas/capacitive_plasma.html.

[9] Dr Paul May, Bristol University - Plasmas and Plasma-Surface Interactions http://www.chm.bris.ac.uk/~paulmay/misc/msc/msc1.htm.

[10] Daniel M. Dobkin - Alternative Discharges: Fields and Waves http://www.batnet.com/enigmatics/semiconductor_processing/CVD_Fundamentals/plasmas/Other_plasmas.html.

[11] F. Paschen, *Ueber die zum Funkenübergang in Luft, Wasserstoff und Kohlensäure bei verschiedenen Drucken erforderliche Potentialdifferenz*, Annalen der Physik **273** (5): 69-75, (1889)

[12] Daniel M. Dobkin - Effects of Operating Parameters on Capacitive Plasmas http://www.batnet.com/enigmatics/semiconductor_processing/CVD_Fundamentals/plasmas/Cap_parameters.html

[13] Robert Thomas - A Beginner's Guide to ICP-MS Part IV: The Interface Region http://www.spectroscopymag.com/spectroscopy/article/articleDetail.jsp?id=1097

[14] Traci Bradford and M. Nicole Cook - Inductively Coupled Plasma http://www.cee.vt.edu/program_areas/environmental/teach/smprimer/icp/icp.html

[15] Robert Thomas - A Beginner's Guide to ICP-MS Part III: The Plasma Source http://www.spectroscopymag.com/spectroscopy/article/articleDetail.jsp?id=1096

[16] Daniel M. Dobkin - Alternative Discharges: Fields and Waves http://www.batnet.com/enigmatics/semiconductor_processing/CVD_Fundamentals/plasmas/Other_plasmas.html

[17] Robert Thomas - A Beginner's Guide to ICP-MS Part IV: The Interface Region http://www.spectroscopymag.com/spectroscopy/article/articleDetail.jsp?id=1097

[18] Traci Bradford and M. Nicole Cook - Inductively Coupled Plasma http://www.cee.vt.edu/program_areas/environmental/teach/smprimer/icp/icp.html

[19] Oleg Kornienko, Peter T. A. Reilly, William B. Whitten, and J. Michael Ramsey, *Field-Emission Cold-Cathode EI Source for a Microscale Ion Trap Mass Spectrometer*, *Analytical Chem.* **72,** 559-562 (2000).

[20] Amaratunga, G. A. J. and Silva, S. R. P. *Nitrogen containing hydrogenated amorphous carbon for thin film field emission cathodes,* Appl. Phys. Lett. **68,** 2529-2531 (1996)

[21] Jeffrey R. Bacon, Allan M. Ure, *Spark-source Mass Spectrometry: Recent Developments and Applications*, Analyst, October 1984, Vol. 109

[22] Taylor, S.; Tindall, R. F.; Syms, R. R. A. Silicon based Quadrupole Mass Spectrometry using Microelectromechanical Systems. *J. Vac. Sci. Technol.* **B 19,** 557-562. (2001)

[23] Wapelhorst, E.; Hauschild, J. P.; Müller, J. Complex MEMS: a Fully Integrated TOF Micro Mass Spectrometer. *Sensors and Actuators A* **138,** 22-27, (2007)

[24] Blain, M. G.; Riter, L. S.; Cruz, D.; Austin, D. E.; Wu, G.; Plass, W. R.; Cooks, R. G. Towards the Hand-Held Mass Spectrometer: Design Considerations, Simulation, and Fabrication of Micrometer-Scaled Cylindrical Ion Traps. *Int. J. Mass Spectrom.* **236,** 91-104, (2004)

[25] Pau, S.; Pai, C. S.; Low, Y. L.; Moxom, J.; Reilly, P. T. A.; Whitten, W. B.; Ramsey, J. M. Microfabricated Quadrupole Ion Trap for Mass Spectrometer Applications. *Phys. Rev. Lett.* **96,** 120801 (2006)

[26] Van Amerom, F. H. W.; Chaudhary, A.; Cardenas, M.; Bumgarner, J.; Short, R. T. Microfabrication of Cylindrical Ion Trap Mass Spectrometer Arrays for Handheld Chemical Analyzers. *Chem. Eng. Comm.* **195,** 98-114, (2008)

[27] Song, Y.; Wu, G.; Song, Q.; Cooks, R. G.; Ouyang, Z.; Plass, W. Novel Linear Ion Trap Mass Analyzer Composed of Four Planar Electrodes. *J. Am. Soc. Mass Spectrom.* **17,** 631-639, (2006)

[28] Austin, D. E.; Wang, M.; Tolley, S. E.; Maas, J. D.; Hawkins, A. R.; Rockwood, A. L.; Tolley, H. D.; Lee, E. D.; Lee. M. L. Halo Ion Trap Mass Spectrometer. *Anal. Chem.* **79,** 2927-2932, (2007)

Chapter 2

Ion source simulation and modelling

2.1 Numerical modelling techniques

Two and three dimensional (2D and 3D) modelling of the ion sources used in mass spectrometry and the modeling of the mass analyser itself requires electrostatic field solving. In the absence of free charges the electrostatic field and potential may be found by solution of the Laplace equation:

$$\nabla \underline{E} = 0 \tag{2.1}$$

where $\underline{E}$ the electric field and ' ∇ 'is the vector operator ('del') such that:

$\nabla \underline{E} = \partial \underline{E} / \partial x + \partial \underline{E} / \partial y + \partial \underline{E} / \partial z$ .The electric potential V may be obtained from the field which is given by:

$$\underline{E} = -\nabla V \tag{2.2}$$

Although analytical solutions of the electric field from the Laplace equation are possible in some cases [1], the vast majority of cases and designs used in instruments require a numerical approach. This may be done to high accuracy using Finite Difference Methods (FDM) and/or Finite Element Methods (FEM) [2]. FDMs approximate the solutions to differential equations by replacing derivative expressions with approximately equivalent difference quotients. The FDM method is explained below.

Consider a region of potential V as shown in figure 2.1:

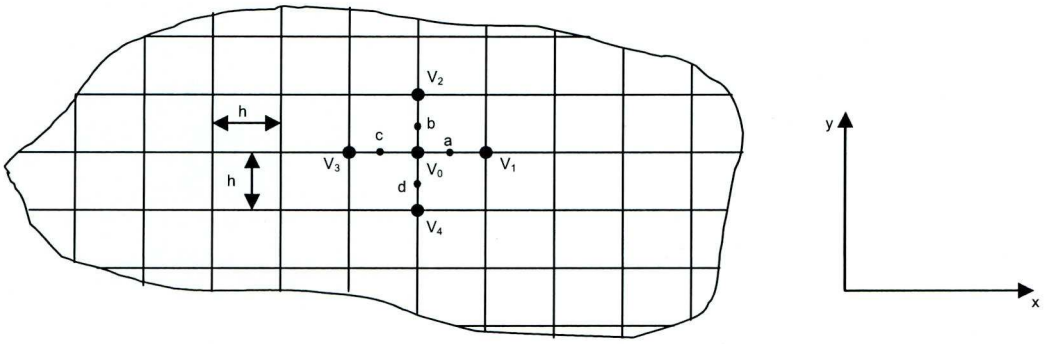

Figure 2.1: Finite Difference Method of electrostatic field analysis.

For point "a" midway between nodes 0 and 1, provided h is small:

$$\left.\frac{\partial V}{\partial x}\right|_a \approx \frac{1}{h}(V_1 - V_0) \tag{2.3}$$

Similarly for point "c": $\left.\frac{\partial V}{\partial x}\right|_c \approx \frac{1}{h}(V_0 - V_3)$

So that

$$\left.\frac{\partial^2 V}{\partial x^2}\right|_o \approx \frac{1}{h}\left[\left.\frac{\partial V}{\partial x}\right|_a - \left.\frac{\partial V}{\partial x}\right|_c\right] \approx \frac{1}{h^2}\left[(V_1 - V_0) - (V_0 - V_3)\right]. \tag{2.4}$$

Similarly considering potentials along the y-axis:

$$\left.\frac{\partial^2 V}{\partial y^2}\right|_o \approx \frac{1}{h^2}\left[(V_2 - V_0) - (V_0 - V_4)\right], \tag{2.5}$$

and substituting (2.4) and (2.5) in Laplace's equation:

$$\frac{\partial^2 V}{\partial X^2} + \frac{\partial^2 V}{\partial y^2} \approx \frac{1}{h^2}\left[(V_0 - V_1) - (V_3 - V_0) + (V_0 - V_2) + (V_0 - V_4)\right] = 0$$

$$\therefore -4V_0 - V_1 - V_3 - V_2 - V_4 \approx 0 \quad \text{and} \quad V_0 \approx \frac{1}{4}(V_1 + V_2 + V_3 + V_4). \tag{2.6}$$

Thus, if the potentials at V1, V2, V3 and V4 are known then V0 may be found by successive approximation. This formula is an example of a Finite Difference Method (FDM), used here for potential (V) determination. Electric fields may be found provided that the distance between adjacent nodes of the electrode structure (x_1-x_2) is known, according to:

$$\underline{E} = - \Delta V/\Delta x = - (V_2 - V_1) / (x_2 - x_1). \qquad (2.7)$$

The differences between FEM and FDM are that the FDM is an approximation to the differential equation; the FEM is an approximation to its solution. The most attractive feature of the FEM is its ability to handle complex geometries (and boundaries) with relative ease. The most attractive feature of FDM is that it can be very easy to implement. A useful comparison of the two methods is given in reference [3].

Since the 1980's the Boundary Element Method (BEM) has become increasingly popular for solution of electromagnetic fields [4]. The BEM is highly accurate and has unique advantages being well-suited to space-charge, cathode problems and nano-structures in the presence of large electrodes. Adaptive surface meshes can be reduced where accuracy is critical. This method is sometimes referred to as the Surface Charge Method or the Integral Equation Method. The BEM also simulates fine meshes and non-enclosed systems. Low-frequency oscillations, such as in a quadrupole, may also be simulated.

The principle of the BEM is simple. The method is based on the fact that in a system of conducting electrodes, real charges appear on the surfaces of the electrodes when potentials are applied to them. In the absence of leakages, these charges will remain when the leads that have carried the applied voltages are removed. These surface charges are then the sources of all the potentials and fields in the system. In the BEM the electrodes are effectively replaced by these charges.

Consider for example an isolated conducting sphere of radius R. If it has a potential V then its total charge q is:

$$q = (4 \pi \varepsilon_0) R V, \tag{2.8}$$

(in SI units) which is uniformly distributed on its surface, as illustrated in Figure 2.2.

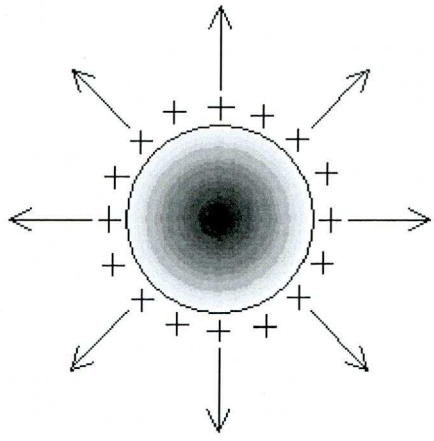

Figure 2.2: Surface charges and external field of an isolated conducting sphere.

The external potential φ and radial field $\underline{E}$ at a distance r from the centre of the sphere are:

$$\varphi(r) = q / (4 \pi \varepsilon_0 r); \quad \underline{E}(r) = q / (4 \pi \varepsilon_0 r^2) \tag{2.9}$$

The potential and field are due to the surface charges on the sphere. If the sphere could be removed without disturbing the surface charges then the potential and field would remain unchanged.

As stated above, the surface charges are the sources of all the potentials and fields in any electrostatic system. If all the surface charges are known then all the potentials and fields are also known. In the BEM the surface charges are deduced from the potentials applied to a set of electrodes.

2.2 Comparison of commercial field solvers: SIMION and CPO

SIMION [5] is a commercial software program for performing charged particles optics simulations. It calculates 2D/3D electrostatic and certain magnetic fields and calculates the trajectories of charged particles through those fields. Low frequency (quasistatic) fields such as in the oscillating voltages on a quadrupole are supported as well. Ion collision and other special effects can also be simulated. SIMION provides a programming, visualization and data recording environment for these simulations.

SIMION uses FDM with optimized over-relaxation and multimesh methods to solve the Laplace equation. In order to calculate ion (ray) trajectories which are variations in ion spatial position with time, SIMION uses Runge-Kutta to solve the necessary ordinary differential equations (ODEs). A workbench strategy allows multiple meshes or possibly different mesh size and symmetry to be used in the same simulation. The user programming feature allows these methods to be extended. Geometries can be defined via multiple methods. SIMION is thus versatile and low cost. It is used widely for the design of mass spectrometer components and lens systems. SIMION was originally developed by David Dahl at what is now Idaho National Labs and is now developed by Scientific Instrument Services, Inc. (SIS).

The CPO (Charged Particle Optics) programs [6] use the BEM described earlier and double precision to give the highest possible accuracy in solving the main matrix equation. Results are usually accurate to better than 10^{-13}. In CPO the electrodes are automatically divided into triangles or rectangles by the program. The User chooses the total number of segments, the maximum number of which depends on the memory space available to the User, and is typically 6000. The User also chooses an 'inaccuracy level' for the ray tracings (i.e. trajectory integrations). A low level can be used for the initial runs, to save time, and then the highest level for the final runs. Techniques exist for extrapolating the final results to an infinite number

of segments and a zero ray inaccuracy. These techniques do not usually exist with commercially available programs that use other methods

Which package to use in the design of a miniature ion source? For the purposes of comparison these two simulation packages SIMION and CPO were used to simulate the results obtained from an ion trap for which experimental details (geometries) and ion oscillation frequencies were already published. The ion trap was used for experiments at the National Physical Laboratory in the UK. Since very small numbers of ions were used in the experiments the effects of space charge could be neglected. CPO and SIMION were used to solve the electrostatic fields for the traps and calculate the ion secular frequencies which were then compared with the published experimental values [7].

An ion in a RF field will undergo oscillations at frequencies related to its mass/charge ratio, the trap geometry and the applied RF excitation frequency. These ion motional frequencies are normally called secular frequencies since ion micromotion within a trap is very small compared to secular motion and its influence can be neglected for high frequencies. The expression for angular secular frequencies is an algebraic progression and it is given by [8]:

$$\omega_{u,n} = \left(n \pm \frac{\beta_u}{2} \right) \Omega, \qquad 0 \le n < \infty, \tag{2.10a}$$

where n represents the frequency order, Ω is the angular frequency equal to $2\pi f$ and β_u is a trapping parameter, which determines the speed of ion motion and it is defined with a_u and q_u, so that $0 < \beta_u < 1$ must hold. In order to obtain the exact value of β_u, a continued fraction in terms of a_u and q_u must be used. The fourth order approximation for β_u is given by [9]:

$$\beta_u = \left[a_u - \frac{(a_u - 1) q_u^{\,2}}{2(a_u - 1)^2 - q_u^{\,2}} - \frac{(5a_u + 7) q_u^{\,4}}{32(a_u - 1)^3 (a_u - 4)} \right]^{1/2}. \tag{2.10b}$$

The angular secular frequency at $n = 0$ is:

$$\omega_u = \frac{\beta_u}{2}, \tag{2.11}$$

and it is called the fundamental frequency, having the lowest value of all orders and the highest power spectrum.

The NPL ion trap shown in Figure 2.3a consists of two inner endcap electrodes and two outer endcap electrodes concentric with inner ones. The outer endcaps are moved back to allow sufficient space for laser access.

To produce an ideal quadrupole field, equal RF voltages are applied to the inner endcaps, while small DC voltages can be applied to the outer endcaps, which are normally grounded. In effect, the inner endcaps confine ions in the axial (z) direction, while the outer endcaps prevent ions from escaping in the radial (x,y) direction. The equipotential lines in zx/zy planes produced using CPO are shown in Figure 2.3b.

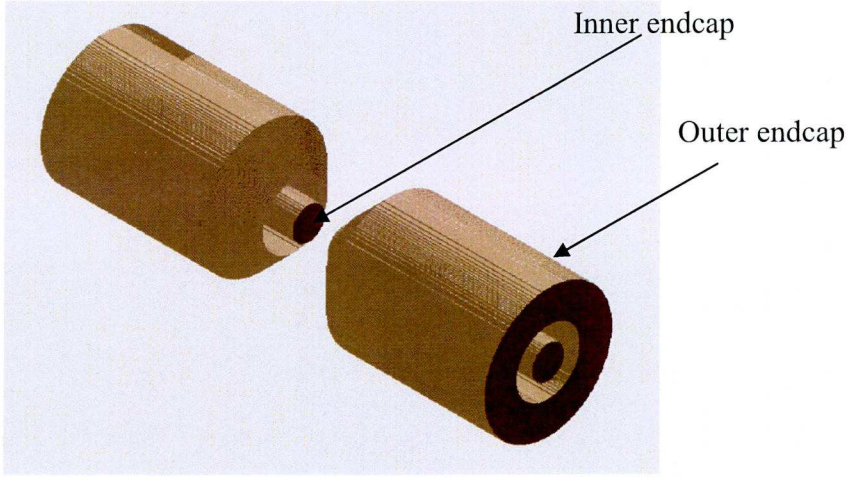

Figure 2.3a: NPL endcap trap model.

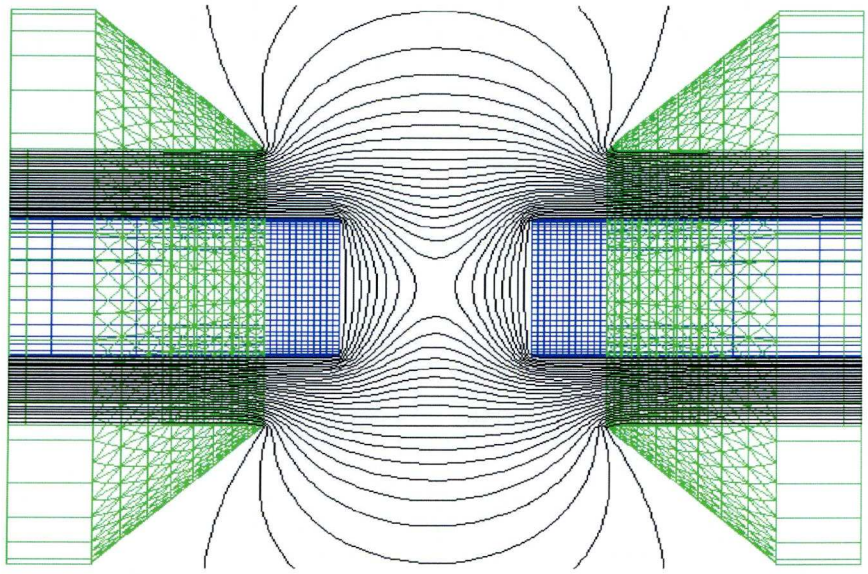

Figure 2.3b: Equipotential contours in zx(zy) plane for the NPL endcap trap (above) calculated using CPO.

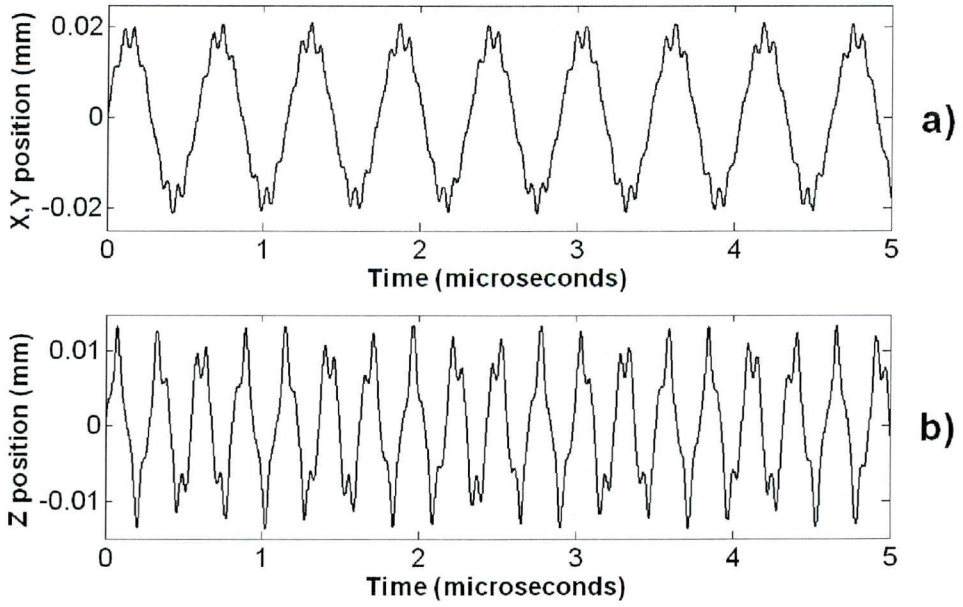

Figure 2.4: Trajectories of a $^{88}Sr^{+}$ ion with respect to time, trapped within the NPL endcap trap generated using CPO. The trap is driven with 245 V RMS at 15.936 MHz.

If now an ion is injected into the trap (given a set of starting coordinates) with a specific energy, then for a given set of applied voltages its trajectory can be calculated by Runge-Kutta numerical solution of Newton's second law ($F = m\, d^2u/dt^2$) where u = x(t) or y (t). Individual coordinate plots (trajectories) with respect to time are shown in Figure 2.4. Ion micromotion is here clearly visible at the peaks of the plots. It exists in all three dimensions due to an RF field from the inner endcaps directly applied in the axial direction, which spreads to the outer endcaps and has components in the radial direction.

Five sets of simulations were carried out with CPO and with SIMION using the same voltages and conditions that had been previously used to obtain the published experimental data. Figures 2.5 to 2.9 below show the individual frequency responses (power spectra) determined from the Fourier transform of the resulting ion trajectories for the five sets of parameters. The MATLAB code used to obtain the power spectra is given in Appendix 2.1. The right hand graphs are simply magnified versions of the left hand graphs so as to enable accurate determination of the fundamental frequency from the ion secular frequency in each case.

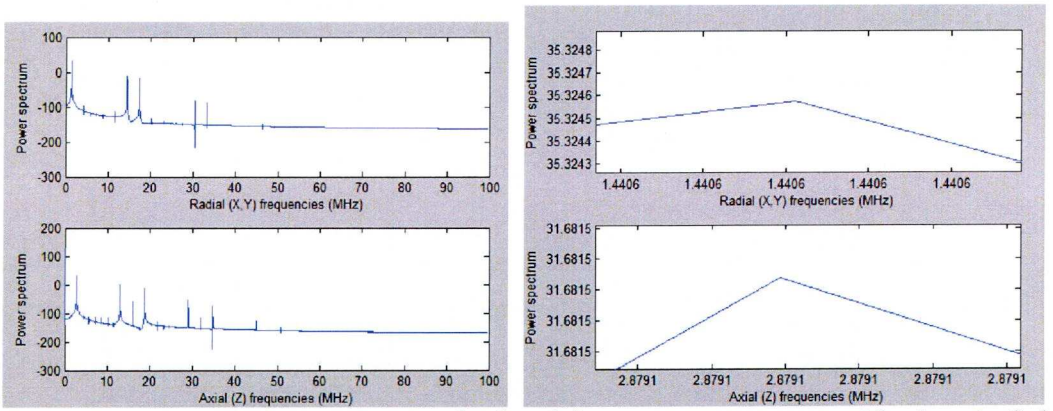

Figure 2.5: Set 1 Power spectra calculated from ion trajectories with electric field determined using SIMION for the NPL trap shown in Figure 2.3 Trap voltages V_{RF} = 199 V (rms) and V_{DC} = 2.12 V.

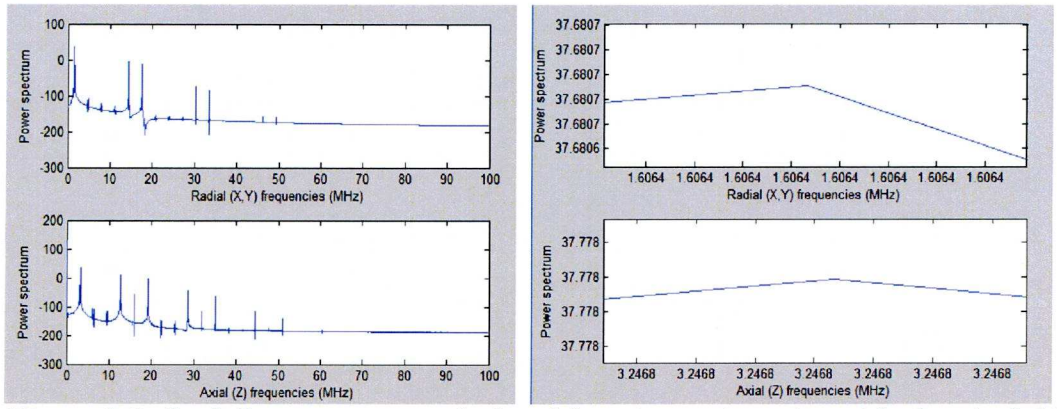

Figure 2.6: Set 2 Power spectra calculated from ion trajectories with electric field determined using SIMION for the NPL trap shown in Figure 2.3. Trap voltages V_{RF} = 221 V (rms) and V_{DC} = 2.55 V.

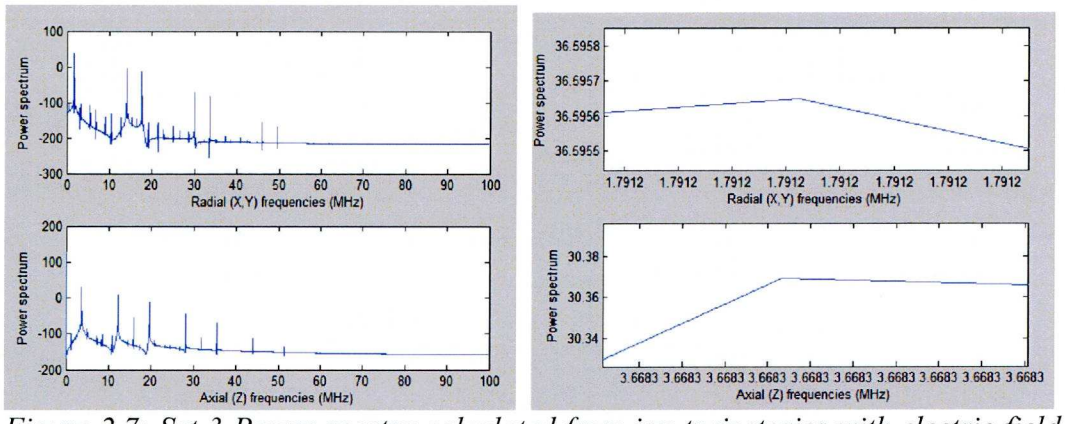

Figure 2.7: Set 3 Power spectra calculated from ion trajectories with electric field determined using SIMION for the NPL trap shown in Figure 2.3 Trap voltages V_{RF} = 245 V (rms) and V_{DC} = 3.31 V.

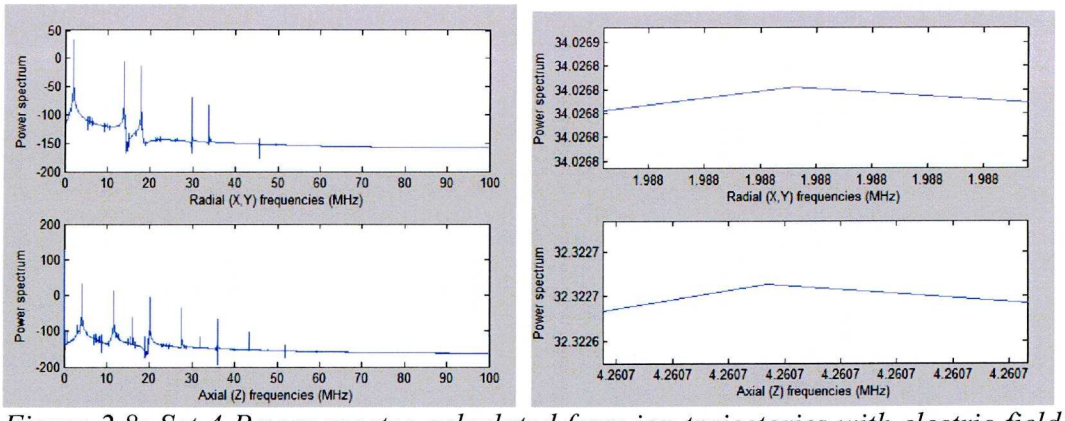

Figure 2.8: Set 4 Power spectra calculated from ion trajectories with electric field determined using SIMION for the NPL trap shown in Figure 2.3. Trap voltages V_{RF} = 274 V (rms) and V_{DC} = 2.39 V.

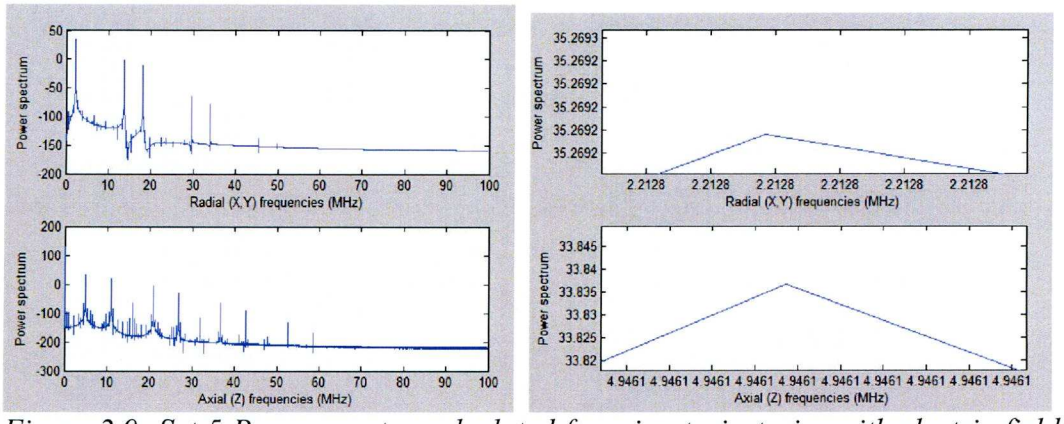

Figure 2.9: Set 5 Power spectra calculated from ion trajectories with electric field determined using SIMION for the NPL trap shown in Figure 2.3 Trap voltages V_{RF} = 304 V (rms) and V_{DC} = 2.38 V.

The results above are summarised in Table 2.1 (taken from reference [7]) and show that the secular frequencies calculated with both SIMION and CPO are accurate to within 4% in every case with the published experimental secular frequencies.

Secular frequencies	**Method**	**1st set**	**2nd set**	**3rd set**	**4th set**	**5th set**
		199 V RMS	221 V RMS	245 V RMS	274 V RMS	304 V RMS
		15.955 MHz	15.948 MHz	15.936 MHz	15.925 MHz	15.910 MHz
		2.12 V DC	2.55 V DC	3.31 V DC	2.39 V DC	2.38 V DC
$\omega_{x,y}/2\pi$	Experiment	1.395 MHz	1.590 MHz	1.800 MHz	1.980 MHz	2.230 MHz
$\omega_z/2\pi$	Experiment	2.985 MHz	3.360 MHz	3.795 MHz	4.340 MHz	5.070 MHz
$\omega_{x,y}/2\pi$	BEM	1.403 MHz	1.596 MHz	1.789 MHz	1.980 MHz	2.227 MHz
$\omega_z/2\pi$	BEM	2.939 MHz	3.265 MHz	3.767 MHz	4.281 MHz	4.960 MHz
$\omega_{x,y}/2\pi$	FDM	1.441 MHz	1.606 MHz	1.791 MHz	1.988 MHz	2.213 MHz
$\omega_z/2\pi$	FDM	2.879 MHz	3.247 MHz	3.668 MHz	4.261 MHz	4.946 MHz

Table 2.1 Taken from reference [7] showing a comparison between experimental data and secular frequencies calculated using CPO (BEM) and SIMION (FDM).

It can be seen from Table 2.1 that CPO is more accurate than SIMION, however the simulation time for SIMION was more than an order of magnitude faster (minutes compared to hours) for the same trap modelled in CPO. For this reason, therefore, SIMION was used to design and simulate the electron impact ion source described in rest of this chapter and to determine optimum design and operation conditions when coupled to a miniature QMS.

2.3 Design of electron impact (EI) ion source for a miniature QMS

Some commercially obtained EI sources use 3-electrode plates to achieve injection of ions into the mass analyser. For small aperture mass analyzers (e.g. miniature QMS) it is important to achieve maximum extraction efficiency of ions from the source so as to maximise the instrument sensitivity. The aim of this investigation was to quantify the efficiency improvement obtained in using an EI source with 4-electrode plates instead of 3. As part of this investigation, a number of different plate thicknesses and plate distances were also tested to determine the optimum operating conditions.

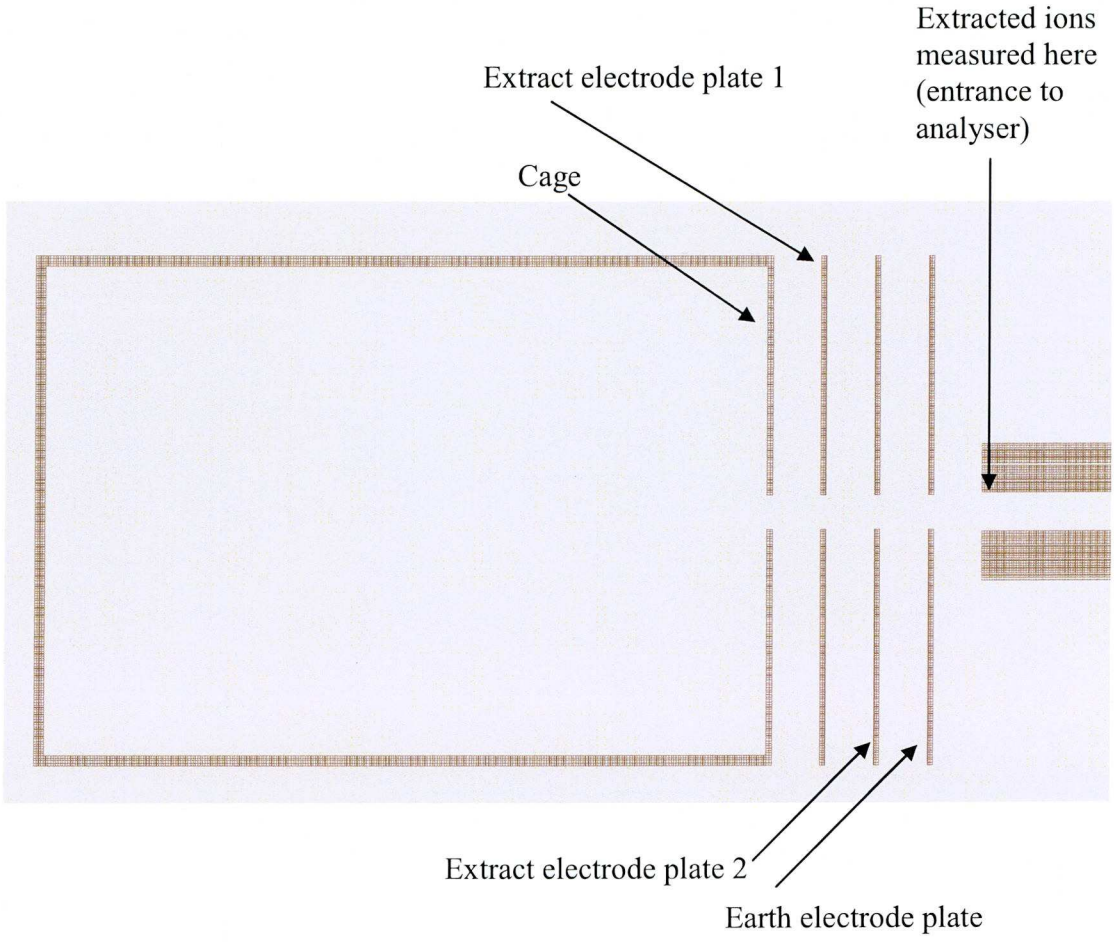

Figure 2.10 Schematic diagram of the 4 electrode plate EI ion source simulated in SIMION.

The SIMION model used is shown in Figure 2.10, showing the ionisation volume within the cage on the left hand side and extraction optics (2 extraction electrode plates and an earth plate) on the right hand side. The grid spacing used for the SIMION simulations was 0.05mm, with a cylindrical geometry assumed. A total of 250 ion trajectories were simulated in each case originating from 5 different locations (planes) within the ionisation volume (see Figure 2.14).

2.3.1 Variation of electrode plate thickness

The results shown in figures 2.10 to 2.12 below were obtained from SIMION using three different plate thicknesses (0.1, 0.4, and 0.8mm). This test was performed to determine if increasing the plate thicknesses would have a positive effect on extraction efficiency and beam collimation. Further results can be seen in Appendix 2.2.

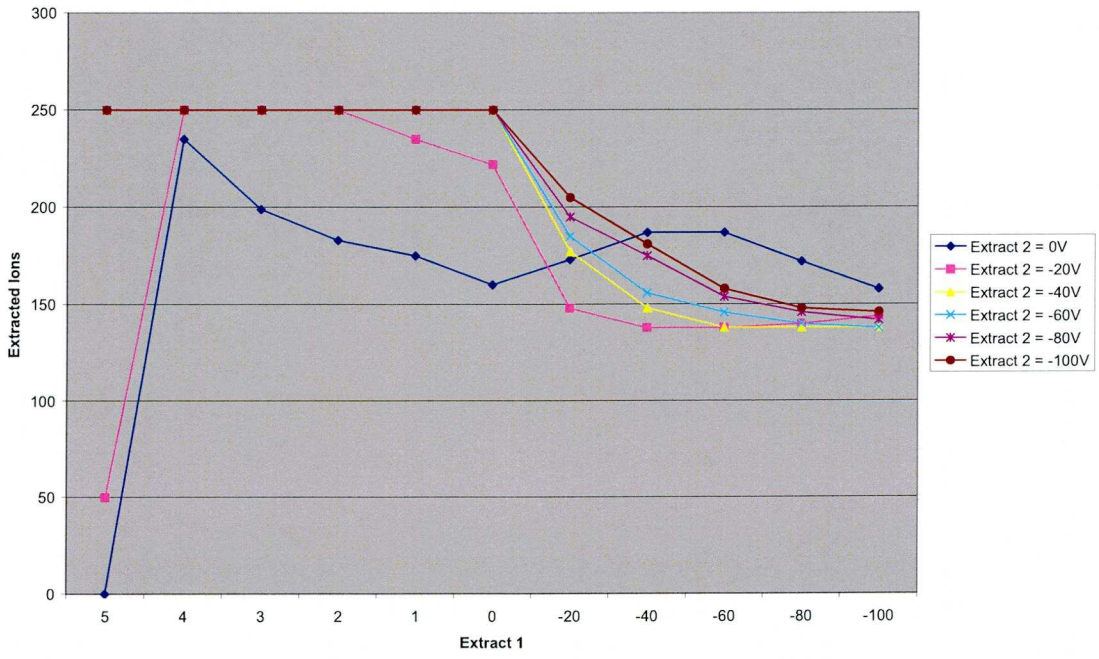

Figure 2.10: Variation of number of extracted ions versus extract electrode potentials for electrode plate thickness = 0.1mm.

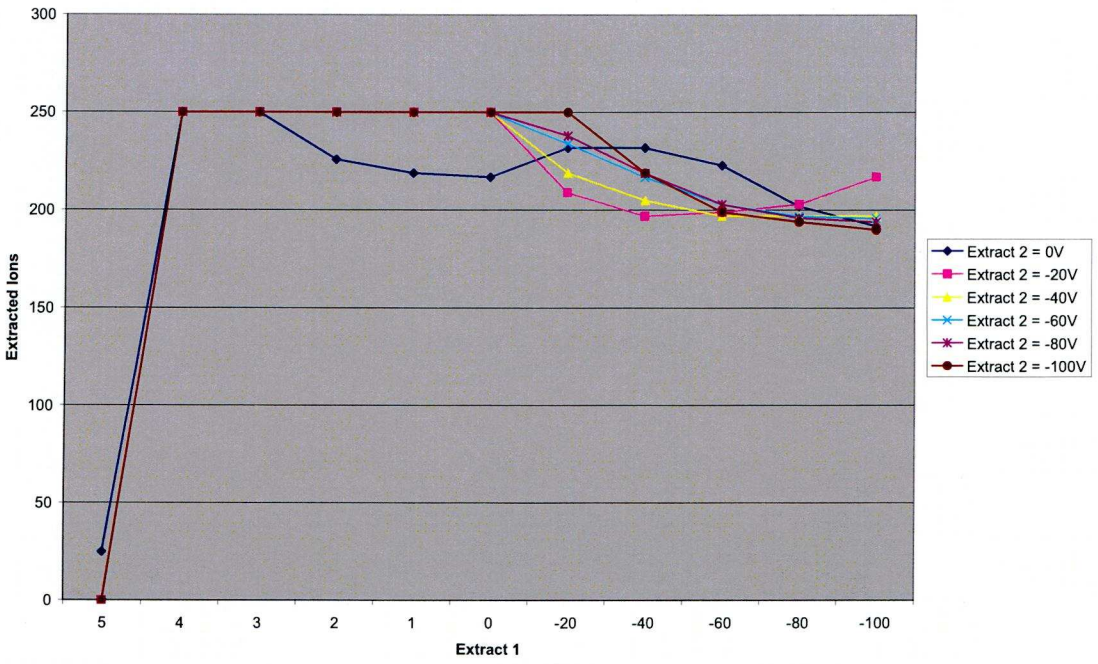

Figure 2.11: Variation of number of extracted ions versus extract electrode potentials for electrode plate thickness = 0.4mm.

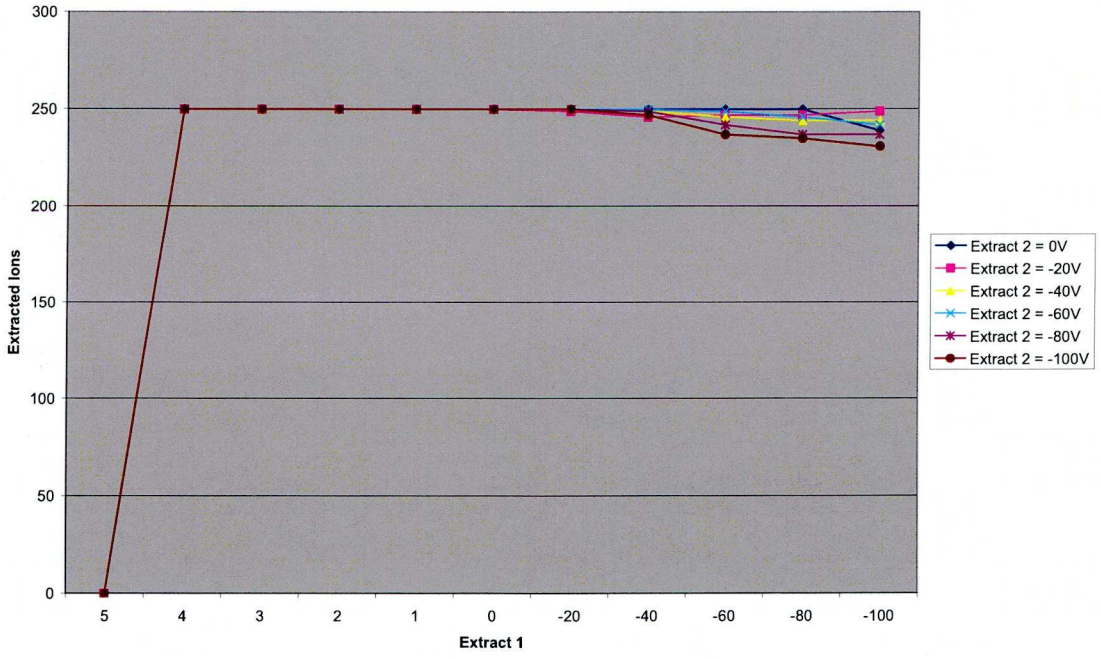

Figure 2.12: Variation of number of extracted ions versus extract electrode potentials for electrode plate thickness = 0.8mm.

From the results, it can be seen that as the thicknesses of the plates are increased the extraction efficiency (number of ions reaching the analyser) is also increased. It is also clear from the results that the 0.8mm thick plate (Figure 2.12) produced the best results in terms of number of ions extracted reaching to almost 100% of the ions being extracted across the range of extract electrode potentials. Further results shown in Appendix 2.2 show the 3 different plate thicknesses plotted on the same graph for multiple Extract 2 voltages.

2.3.2 Variation of individual plate thicknesses

The following results were obtained by varying the thickness of each of the plates to determine if the increase in extraction efficiency seen with 0.8mm plates is due to the cumulative effect of increasing the thickness of all the plates, or if any particular electrode plate is responsible for the increase in ion extraction efficiency.

Table 2.2 lists the 9 different plate thickness combinations used in the simulation. The results are plotted in Figure 2.13, where each combination is corresponds to the Index Number 1 to 9 shown on the table below.

Cage (mm)	Extract 1 (mm)	Extract 2 (mm)	Earth (mm)	Index Number
0.1	0.1	0.1	0.1	1
0.1	0.1	0.1	0.4	2
0.1	0.1	0.1	0.8	3
0.1	0.1	0.4	0.1	4
0.1	0.1	0.8	0.1	5
0.1	0.4	0.1	0.1	6
0.1	0.8	0.1	0.1	7
0.4	0.1	0.1	0.1	8
0.8	0.1	0.1	0.1	9

Table 2.2 Different combinations of extract electrode plate thicknesses.

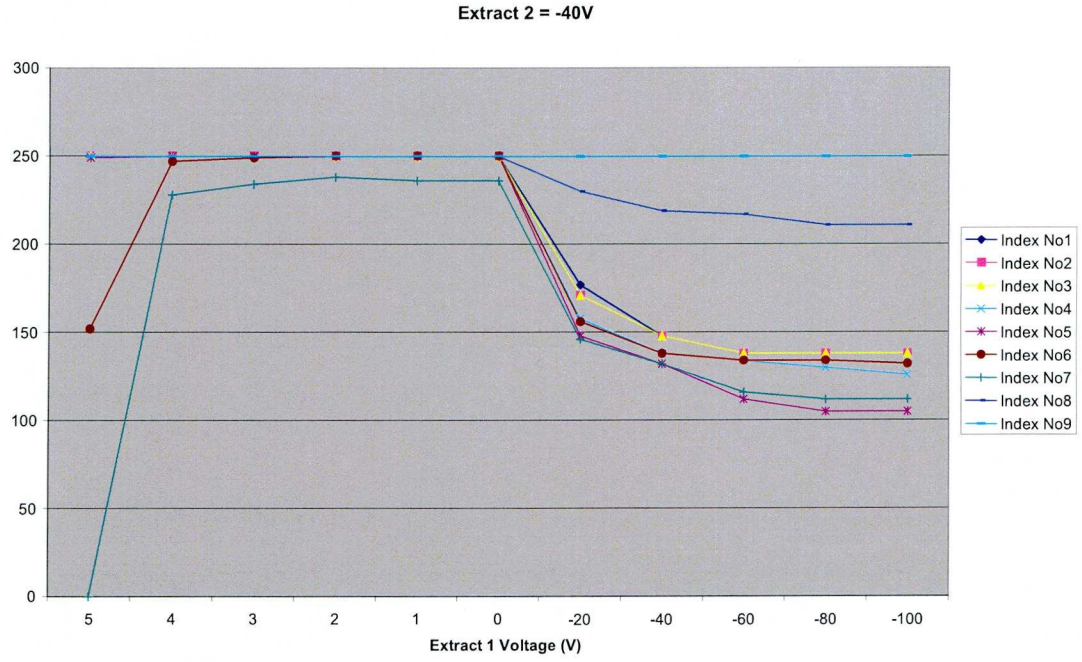

Figure 2.13: Variation of number of extracted ions versus extract electrode 1 potentials for varying electrode plate thicknesses as per Table 2.2.

From Figure 2.13, it can be clearly seen that two of the combinations (index number 8 and 9) have much higher extraction efficiencies than the rest of the results. These two results correspond to the cage plate thickness variation, with cage plates of 0.4mm and 0.8mm producing higher extraction efficiencies.

Figures 2.14 and 2.15 are screen shots that show the extracted ion rays (trajectories) for the two combinations of plate thicknesses that produce the best results (index numbers 8 and 9). The ion rays originate from 5 different locations along the length of the ionization volume as explained earlier. The simulation shows that in both cases a good collimated beam of ions entering the mass analyser is created, especially using the 0.8mm thick cage plate. The results for the other combinations (Index Number 1 - 7) are shown in Appendix 2.3

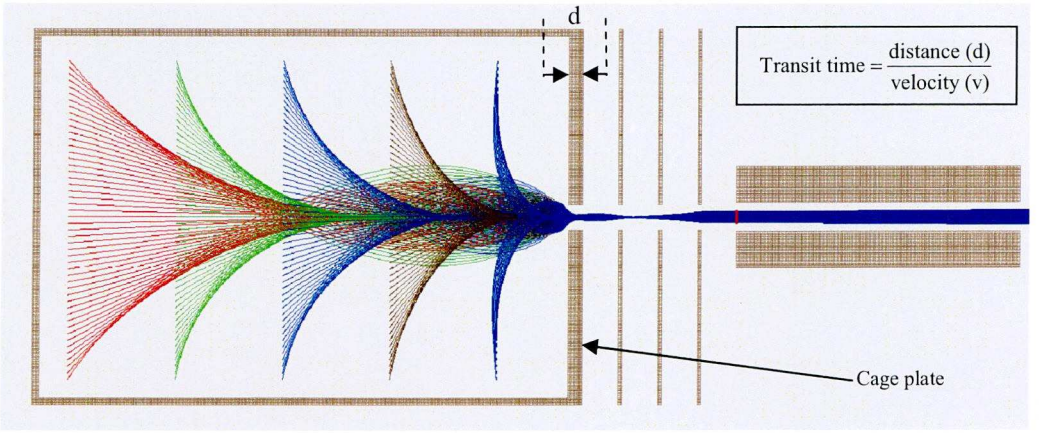

Figure 2.14: SIMION output showing ion trajectories (rays) and beam profile for Index Number 8 of Table 2.2 (Cage = 0.4mm, Extract1 = 0.1mm, Extract2 = 0.1mm, Earth = 0.1mm) with potentials: Cage = +5V Extract 1 = +4V Extract 2 = -40V.

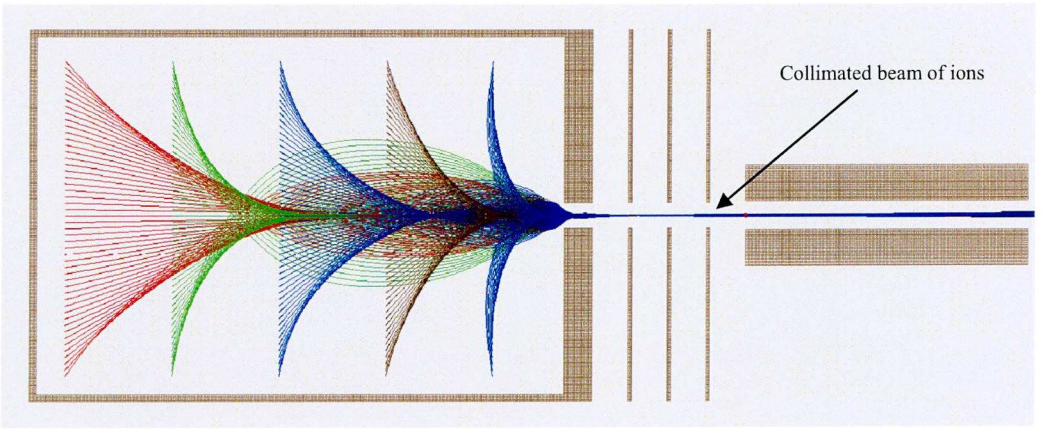

Figure 2.15: SIMION output showing ion trajectories (rays) and beam profile for Index Number 9 of Table 2.2 (Cage = 0.8mm, Extract1 = 0.1mm, Extract2 = 0.1mm, Earth = 0.1mm) with potentials: Cage = +5V Extract 1 = +4V Extract 2 = -40V.

2.3.3 Variation of distance between plates

The final simulation performed on this 4 plate ion source was to see the effect of varying the distance between the electrode plates. The plate thickness was kept constant at 0.8mm for all the plates in this test. The distances used were 0.5, 1.0, 1.5, and 3.0mm. The results are shown below in Figure 2.16.

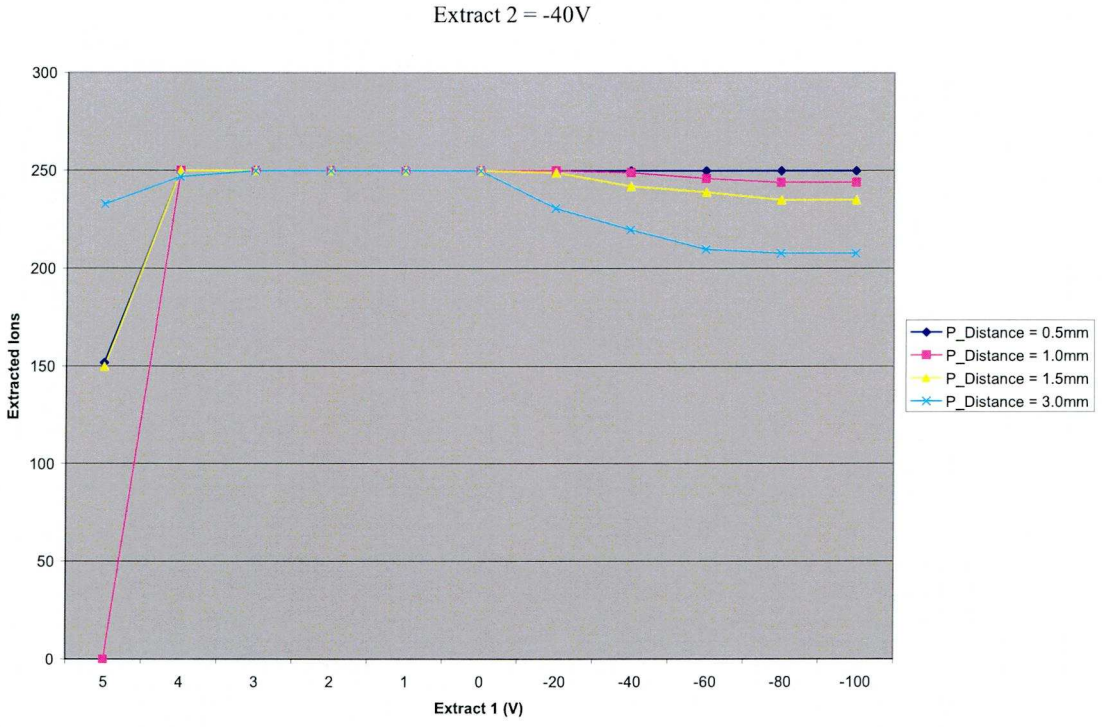

Figure 2.16: Variation of number of extracted ions versus extract electrode 1 potential for varying distances between electrode plates. Extract 2=-40V.

From Figure 2.16 the only significant effect is seen when the distance between plates is increased to 3.0mm and at this point there is a reduction in extraction efficiency of between 10% to 24%, which varies depending upon the voltage applied to Extract 2. However, even when the distance between the plates is 3.0mm there is only a significant drop in extraction efficiency when the voltage applied to Extract 1 is in the range of 0V to -100V, and at these voltages the beam produced is non ideal anyway since it is not collimated. Simulations were also carried out with a 3-plate EI source. In general, the control of the extraction efficiency was more difficult and although similar extraction efficiencies could be obtained for certain voltage combinations the beam collimation was significantly worse for the 3-plate source.

2.3.4 Optimum design of 4-plate EI source

From the previous simulations, the optimum design of the 4 plate ion source was found to be: electrode plate distance D: $0.5 < D < 1.0$mm, cage electrode plate thickness t = 0.8mm, extract/earth electrode plate thickness t=0.1mm, Extract 1 potential $V_{P1} = 0 < V_{P1} < 4$V, and Extract 2 potential $V_{P2} = -20 < V_{P2} < -60$V. The greater transit time of the thicker cage plates produced a more collimated beam of ions. This can be seen by comparing figures 2.14 and 2.15 (above) with Appendix 2.3 Figure A, the distance "d" marked on figure 2.14 is the cage thickness, the thicker this is the longer the transit time. Electrode plate separations of less than 1.0mm were found to give the optimum results in terms of beam collimation, due to reduced beam spreading in the space between the plates.

2.4 Conclusions

In this chapter, the theory underlying two numerical methods (FDM and BEM) commonly used in electrostatic field solving has been explained and compared. Two commercially available software packages SIMION and CPO have been evaluated by comparing simulations with published experimental results (secular frequencies) for the NPL endcap ion trap. Good agreement to the published secular frequencies was obtained for both simulation packages with CPO being more accurate, but this was at the expense of greatly increased computing simulation times. SIMION was therefore deemed to be a better choice for design and simulation of a miniature EI source. SIMION simulations of a 4-electrode plate EI source allowed the best geometry and operating conditions to be determined.

References

[1] W.Hayt and J.A Buck, *Engineering Electromagnetics*, 6th Edition, McGraw-Hill, New York (2001).

[2] K.W. Morton and D.F. Mayers, *Numerical Solution of Partial Differential Equations, An Introduction*. Cambridge University Press (2005).

[3] Clough, Ray W.; Edward L. Wilson, *Early Finite Element Research at Berkeley*, Fifth U.S. National Conference on Computational Mechanics, Aug. 4-6, 1999

[4] L. C. Wrobel and M. H. Aliabadi *The Boundary Element Method*. New Jersey: Wiley. (2002).

[5] http://www.simion.com/info/SIMION.

[6] http://www.electronoptics.com/More.htm.

[7] B.Brkic, S.Taylor, J.F.Ralph and N.France, *High fidelity simulations of ion trajectories in miniature ion traps using the boundary-element method*, Physical Review **A 73,** 012326 (2006).

[8] R. E. March, *An Introduction to Quadrupole Ion Trap Mass Spectrometry*, J. Mass. Spec. **32**, 351 (1997).

[9] E. DeHoffmann and V. Stroobant, *Mass Spectrometry: Principles and Applications (2nd edition),* John Wiley and Sons Inc (2001).

Chapter 3

The Quadrupole Mass Filter (QMF)

3.1 Introduction

In this chapter the theory of operation of the ideal Quadrupole Mass Filter (QMF) is developed from first principles and the governing equations are presented. The operation of a Quadrupole Mass Spectrometer (QMS) is reviewed and the QMS simulation program (QMS-2H) used in the work in this thesis is explained. Using QMS-2H the optimum exit aperture of a miniature ion source is obtained. Two novel approaches are described for realisation of miniature hyperbolic form QMFs: the first method considered uses Electrode Discharge Machining (EDM) to construct the QMF. The second method uses the Digital Light Processing (DLP) to construct the QMF. There follows an experimental section in which testing of QMS instruments constructed using these novel QMFs is described. In the final part of the chapter the experimental spectra for two novel types of QMS mass filter are obtained and the results are simulated theoretically using QMS-2H.

3.2 Theory of the QMF

Consider a three-dimensional electric field described by the potential variation:

$$\Phi(x,y,z) = \Phi_0 \frac{(x^2 - y^2)}{2r_0^2} \tag{3.1}$$

This potential distribution satisfies the Laplace equation, and is invariant along the z axis. For a particular value of Φ_0, the equipotentials (lines of constant potential) in

the xy plane are four rectangular hyperbolas with asymptotes at 45° to the Cartesian axes, as indicated in the figure 3.1 below:

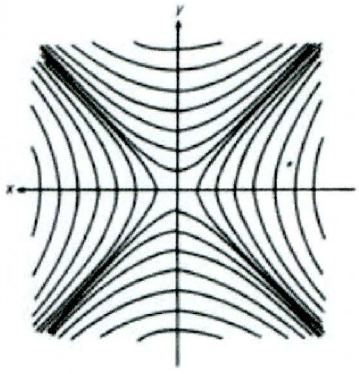

Figure 3.1: Equipotentials in the xy plane as described by equation 3.1

A potential distribution of this form may be set up by means of 4 hyperbolic electrodes in quadrupolar arrangement as shown in figure 3.2 or, more conveniently and to a good approximation, by the use of cylindrical electrodes with the correct spacing [1].

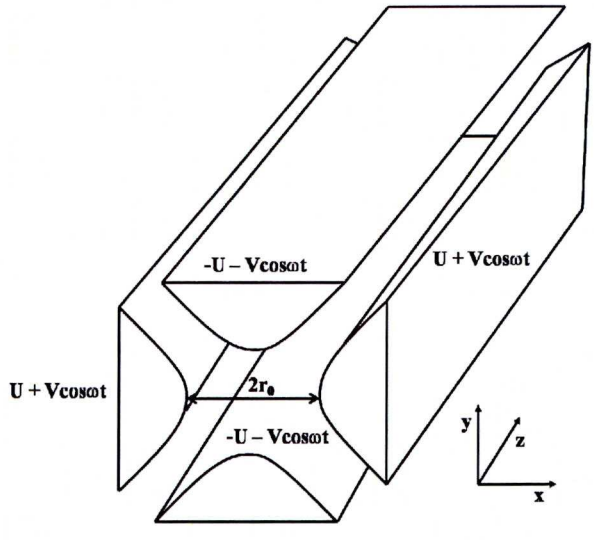

Figure 3.2: Hyperbolic electrodes

Consider the motion of an ion of mass m and charge q, subjected to the electric field given by equation (3.1):

Following Dawson [1] we obtain three independent differential equations:

$$\frac{d^2x}{dt^2}+\left(\frac{e}{mr_0^2}\right)\Phi_0 x=0$$

$$\frac{d^2y}{dt^2}-\left(\frac{e}{mr_0^2}\right)\Phi_0 y=0$$

$$\frac{d^2z}{dt^2}=0 \qquad (3.2)$$

If the axial velocity is constant on entering the QMF then there is no acceleration along the z axis and the resulting motion in the x and y directions depends on the variation with time of the potential Φ_0.

For the QMF a combination of direct and alternating voltage is chosen as shown in figure 3.2 such that:

$$\Phi_0 = U - V\cos(2\pi ft) \qquad (3.3)$$

Substituting equation (3.3) into (3.2), the equation of motion for the ion then becomes:

$$\frac{d^2x}{dt^2}+\left(\frac{e}{mr_0^2}\right)\left(U-V\cos(2\pi ft)\right)x=0$$

$$\frac{d^2y}{dt^2}-\left(\frac{e}{mr_0^2}\right)\left(U-V\cos(2\pi ft)\right)y=0 \qquad (3.4)$$

Stable solutions of this pair of equations correspond to transmission of ions by the mass filter and are obtained only for certain values of m, r_0, f, U and V.

By making the substitutions:

$$a = \frac{4eU}{mr_0^2\omega^2} \quad \text{and} \quad q = \frac{2eV}{mr_0^2\omega^2}$$

$$\xi = \omega t/2 = \pi f t \tag{3.5}$$

then both equations (3.4) for 'a' and 'q' can be written in the form:

$$\frac{d^2u}{d\xi^2} + \left(a - 2q\cos\left(2\xi\right)\right)u = 0 \tag{3.6}$$

This equation is the standard form of Mathieu equation. The solutions form the boundaries in (a, q) space between stable and unstable regions as shown in figure 3.3. This diagram is called the a-q stability diagram for the Mathieu equation along a single co-ordinate direction. The shaded areas result in 'stable' ion trajectories where the ion displacement always remains finite.

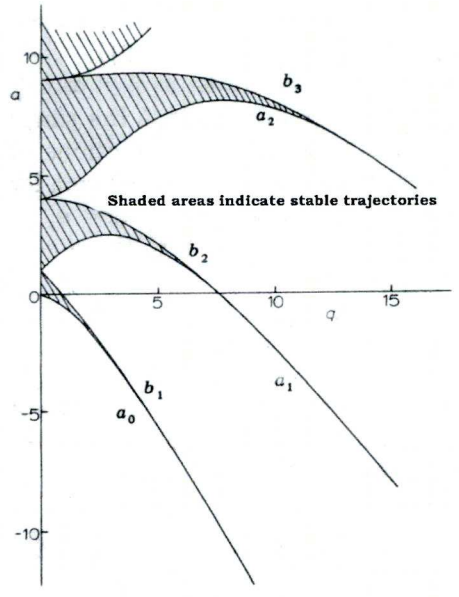

Figure 3.3: Mathieu Stability Diagram

The condition for simultaneous stability in both x and y directions therefore can be represented as seen in Figure 3.4:

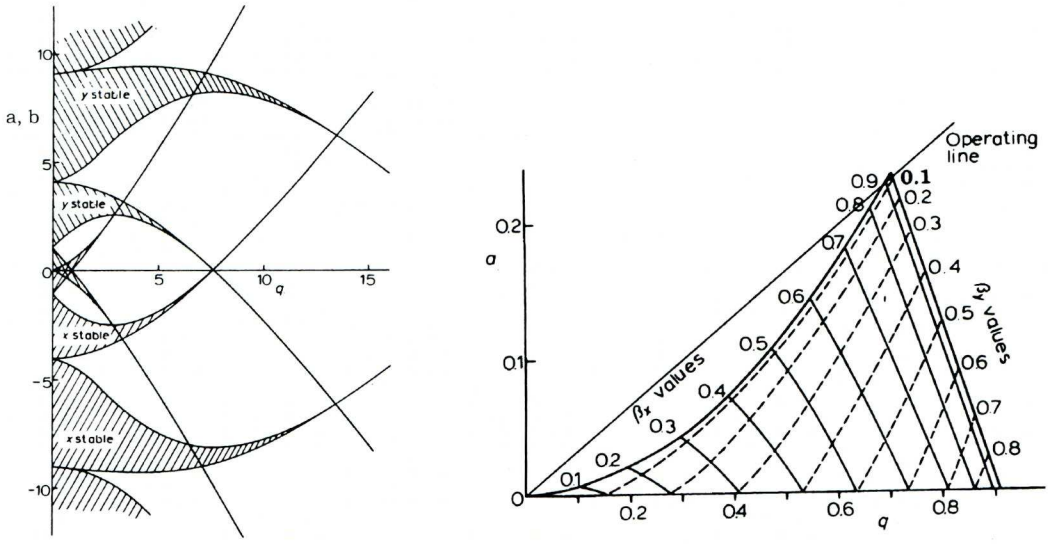

Figure 3.4: Stability in both x and y directions[1].

Figure 3.4 shows the lower stability region normally used in mass filter operation showing iso-β lines for the x and y directions and a typical operation line. For fixed values of r_0, ω, U and V all ions of the same m/e have the same operating point (a, q) in the stability diagram. Since a/q is equal to 2U/V and does not depend on m/e, the operating points for all ions lie on the same line of constant a/q, passing through the origin of the stability diagram. This is called the mass scan line, mass sampling line or operating line.

When $a \neq 0$ only those ions with operating points lying between the intersections of the mass scan with $\beta_y=0$ and $\beta_x=1$ will have stable trajectories in both x and y directions and only those ions will pass through the filter. By increasing the U/V ratio the mass scan line approaches closer to the tip of the stable region and only a narrow range of m/e values will be associated with stable trajectories.

Ions of lower mass will be unstable in x direction and ions of higher mass unstable in y direction. The ions with unstable trajectories will strike the hyperbolic electrodes or exit laterally from the field. The mass number corresponding to the stable region can be changed (the mass spectrum can be scanned) by varying the magnitudes of U and V but maintaining their ratio constant in order to maintain a constant mass resolution.

3.3 Practical operation of a QMS

Ions leaving the source enter the arrangement of 4 electrodes which comprise the QMF (Figure 3.2). Ideally these electrodes are hyperbolic in shape but in practice a good approximation to a hyperbolic field is provided by circular electrodes (rods) with the correct spacing [1]. Two opposite rods have an applied potential of $(U+V\cos(\omega t))$ and the other two rods have a potential of $-(U+V\cos(\omega t))$, where U is a dc voltage and $V\cos(\omega t)$ is an ac voltage of frequency $f = \omega/2\pi$.

The applied voltages affect the trajectories of individual ions travelling down the flight path centered between the four rods. For given dc and ac voltages, only ions of a certain mass-to-charge ratio pass through the rods and reach the detector with all other ions being rejected. The arrangement thus behaves as a mass filter with the pass band tuneable according to the values of U and V. A mass spectrum is obtained by monitoring the ions passing through the QMF as the voltages on the rods are varied. There are two methods: varying ω and holding U and V constant, or varying U and V (U/V) fixed for a constant ω.

3.3.1 Mass range and instrument resolution

The two important operating characteristics of a quadrupole, mass range and mass resolution are dependent on five basic parameters. These are the length and diameter of the rods, the maximum supply voltage to the rods, the rf supply frequency and the ion injection energy.

The mass range or rather the maximum mass is given Eq. (3.7):

$$M_m = \frac{7x10^6 V_m}{f^2 r_0^2} \tag{3.7}$$

where V_m is the rf voltage applied between adjacent rods, r_0 (meters) is the inscribed radius of the rods and M_m is the maximum mass is measured in amu [1]. QMS resolution (R) is defined as the reciprocal of the ratio of the width of the transmitted mass spectrum peak at a defined level of transmission (usually 5%, 10% or 50%) at a particular mass M as shown in Figure 3.5:

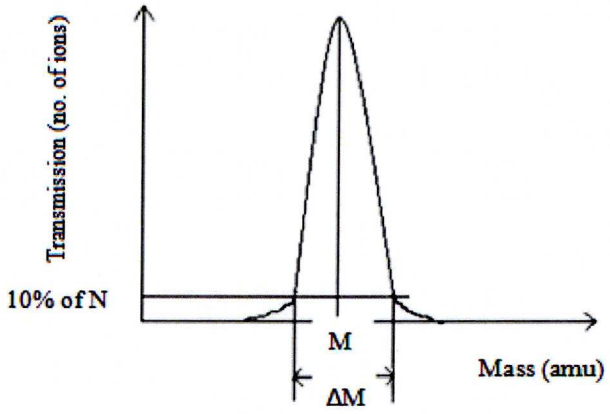

Figure 3.5: Resolution R = M/ΔM where ΔM is measured at a stated % of peak height (transmission) in this case 10%.

The relationship of resolution and mass range to the fundamental instrument parameters is shown in Figure 3.6. The selection of mass range sets a limit to the resolution that can be obtained throughout the operating range.

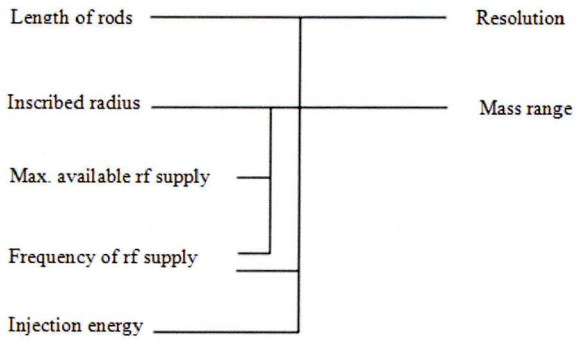

Figure 3.6: Relationship of QMF resolution and mass range to fundamental instrument parameters[1].

The finite length of the quadrupole electrodes limits the time spent by the ions in the focussing field and hence limits the resolution that can be obtained. It is well established that the resolution limit is governed by the number of cycles of rf field to which ions are exposed.

A good representation of the relationship between mass and resolution is [1]:

$$\frac{M}{\Delta M} = \frac{1}{K} N^n \tag{3.8}$$

where N is the number of cycles of the rf field to which the ions are exposed, ΔM is the width of the peak at mass M. It has been experimentally established that n is close to or exactly 2 and K can be assumed to be about 20 for all practical purposes. However the precise value of K must depend upon the method used to define ΔM.

In a given instrument, the number of cycles, N, and hence the limiting resolution can be determined in terms of the following:

(i) the length of the quadrupole rods (L);

(ii) the rf frequency (f); and

(iii) the ion injection energy (V_z)

The relationship between mass and resolution can be written as [1]:

$$\frac{M}{\Delta M} = 0.05\left\{ fL\sqrt{\frac{M}{2eV_z}} \right\}^2 \tag{3.9}$$

where e is the electron charge in Coulombs, V_z is the ion injection energy in electron volts, M the atomic mass and ΔM are measured in kg. Assuming the above values for K and n then we have:

$$\frac{M}{\Delta M} = \frac{0.05 f^2 L^2 M}{2eV_z} \qquad \text{Or} \qquad \Delta M = \frac{40eV_z}{f^2 L^2} \tag{3.10}$$

Simplifying and expressing ΔM in amu gives:

$$\Delta M = \frac{4x10^9 V_z}{f^2 L^2} \tag{3.11}$$

The range of values of ion injection energy is narrow in practical instruments. The lower limit of the order of 2eV, cannot easily be extended because of the difficulties of efficient injection of ions into the QMF. For a conventional QMF the following values are typical L=0.2m, f=2MHz, V_z=5eV in which case Eqn. (3.11) can be simplified to:

$$\Delta M = 0.125 amu \tag{3.12}$$

The above equation shows that an adequate resolution for analytical work is possible. It is also emphasizes that neglecting second-order effects such as field

imperfections, the minimum attainable width ΔM is independent of ion mass in a given operation.

The interrelation between mass range and resolution can be found by rearranging the terms in equation (3.7) and (3.11). Eliminating f gives the following relationship between ΔM and M_m:

$$\Delta M = \frac{570 r_0^2 V_z M_m}{L^2 V_m} \tag{3.13}$$

Clearly the peak width ΔM is directly proportional to M_m, which means that in a given instrument the theoretical maximum resolution given by:

$$\frac{M_m}{\Delta M} = \frac{L^2 V_m}{570 r_0^2 V_z} \tag{3.14}$$

This is independent of the operating frequency.

3.4 QMS simulation

The performance of the QMS investigated in this thesis was simulated by using QMS2-Hyperbolic and QMS2-Ion programs. QMS2-Hyperbolic (QMS2-H) is a trajectory simulation program for a hyperbolic rod quadrupole mass filter and QMS2-Ion simulates the ion entry conditions. The input parameters to QMS2-H are:

- QMF length (l),
- frequency (f),
- QMF inscribed radius (r_0),
- QMF exit radius,
- nominal ion energy (E)
- ion source exit radius (Rie)

these are entered via the GUI shown in figure 3.7.

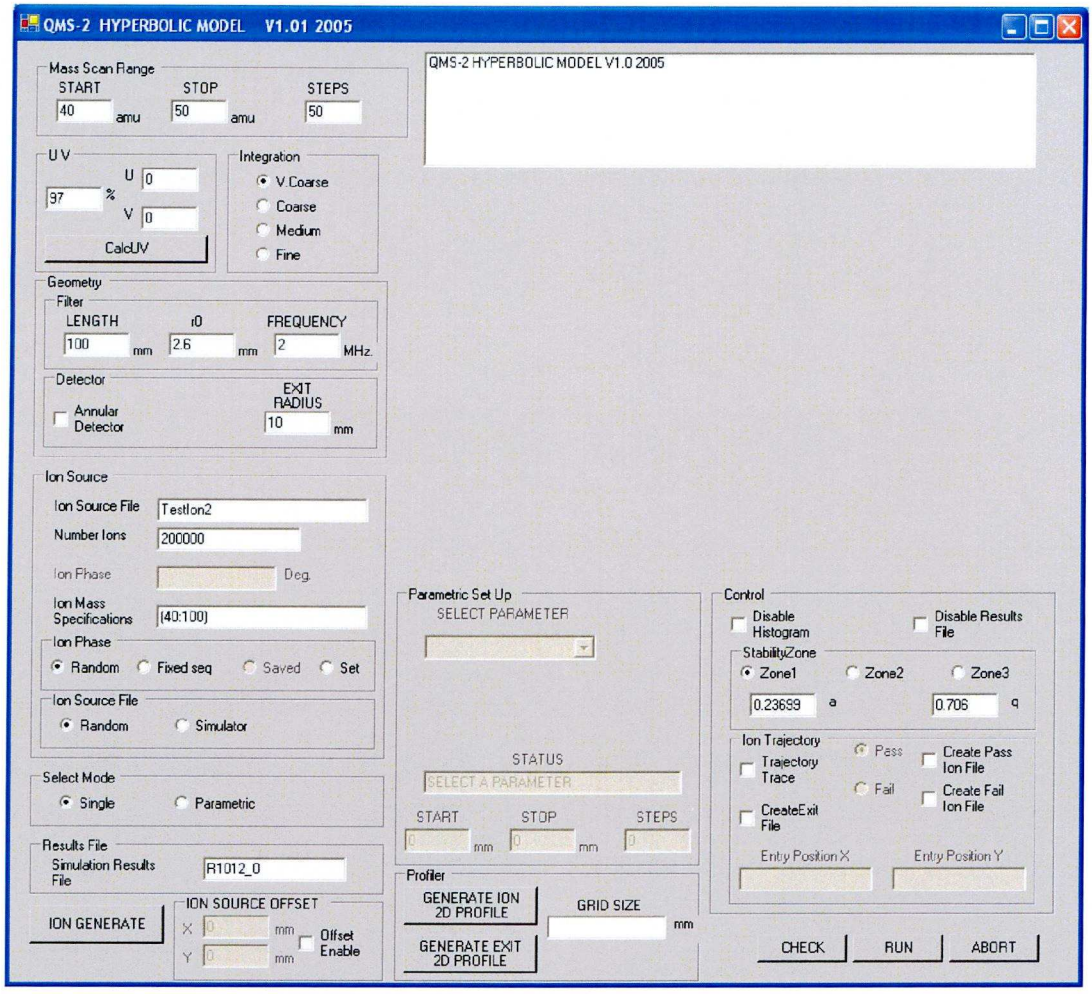

Figure 3.7: Graphical User Interface (GUI) for QMS2-H QMF simulation program.

QMS-2H works by numerically calculating the individual ion trajectories for a large number of ions (typically > 10^7) which are injected into the QMF [2,3]. The program uses a 4^{th} order Runge-Kutta algorithm to numerically solve equations (3.4) for ions injected at a given (x, y) point on the QMF entrance plane. The injection of ions is random in space and time for a given ion source exit aperture using QMS2 –Ion. QMS2-Ion is also able to vary the ion velocity (ie. ion speed and direction) and thus simulate the effect of beam spread. Using the software it is possible to model an individual mass spectrum for one gas or mass spectra from a mixture of up to three gases at one time. For more complex gas mixtures (e.g. air) the simulation has to be run several times. In chapter 2 the optimum dimensions

(plate size, separation and excitation) for a miniature EI source suitable for coupling to a miniature QMF were determined. For best results from a miniature QMS it is necessary also to determine the ion source exit radius for optimum operation and this was done using QMS2-H.

This validity of this approach was established by comparing the numerical model with experimental QMS results for helium. All the main features of the experimental spectra including instrument resolution and transmission with varying ion energy were adequately simulated by the model [5].

The numerical model was also used to compare in detail the performance of QMF's with hyperbolic and circular electrodes [3,6]. The work showed that the hyperbolic form electrodes were superior both in resolution and transmission (sensitivity) for a given set of experimental conditions. For ions that experience more that 60 cycles of RF excitation, the resolution is improved by a factor of 3 using hyperbolic electrodes as opposed to circular ones [6]. The simulations also showed the 'long tail' on the low mass side of the peak was worse for circular than for hyperbolic electrodes, leading to improved abundance sensitivity. More recent simulation work has examined the effect of positional errors in electrode spacing due to tolerances in manufacturing [7]. This has been extended recently to include the 3rd stability region of QMS operation ($a \approx 3.16$ and $q \approx 3.23$) [8].

3.4.1 Optimisation of ion source exit aperture size

The 4 plate miniature EI ion source to be optimised was described in Chapter 2. QMS2-H was used to investigate the effect of the exit aperture size (Rie) of the ion source and how it affects the resolution and transmission of the QMF. Simulations were performed uniformly injecting 10^6 ions into the QMF for ion source exit radii sizes of 0.9mm down to 0.075mm. In each case the number of ions used has been calculated to maintain a constant ion current density for all the aperture sizes investigated. Figure 3.8 shows simulated mass spectra of Ar^+ ions transmitted through a miniature hyperbolic QMF for different ion source exit radii.

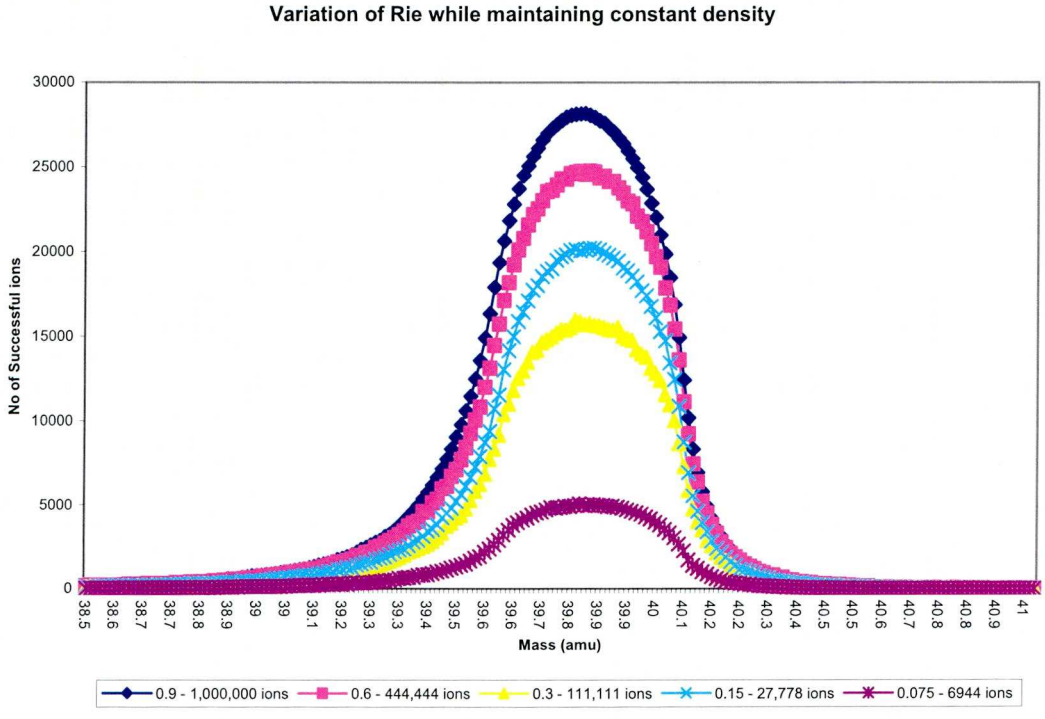

Figure 3.8: Simulated mass spectra of Ar^+ ions transmitted through a miniature hyperbolic QMF.

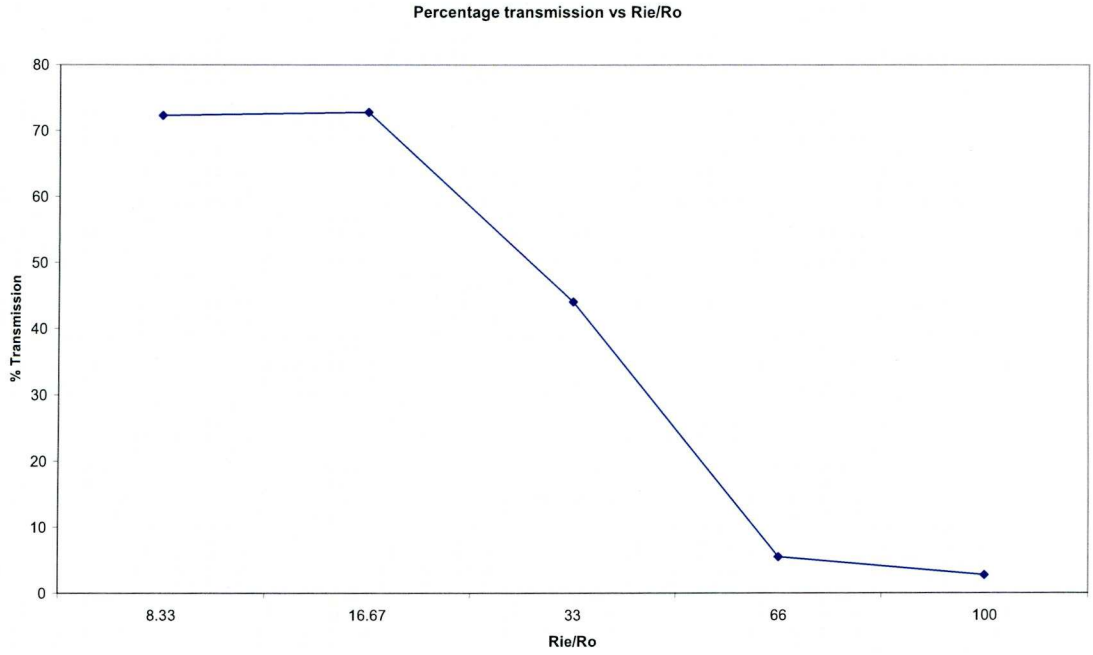

Figure 3.9: Percentage transmission through the QMF as a function of Rie/Ro ratio.

Figure 3.9 is calculated from Figure 3.8 and shows the percentage ion transmission as Rie/Ro is varied. Figure 3.9 shows that as Rie/Ro increases (i.e. Rie approaches Ro) the transmission of ions through the mass filter is reduced. The reason for this is because as Rie is increased the percentage of ions exiting the ion source and entering the QMF closer to the electrodes is increased. Ions closer to the QMF electrodes are much more likely to hit one of the electrodes and not be transmitted. Figure 3.10 shows the resolution at 10% of peak height calculated from the spectra of figure 3.8. The results show that the resolution does improve for smaller apertures, however the change is not significant. Clearly ions injected near the centre of the QMF have a greater chance of successful transmission than ions injected further from the centre.

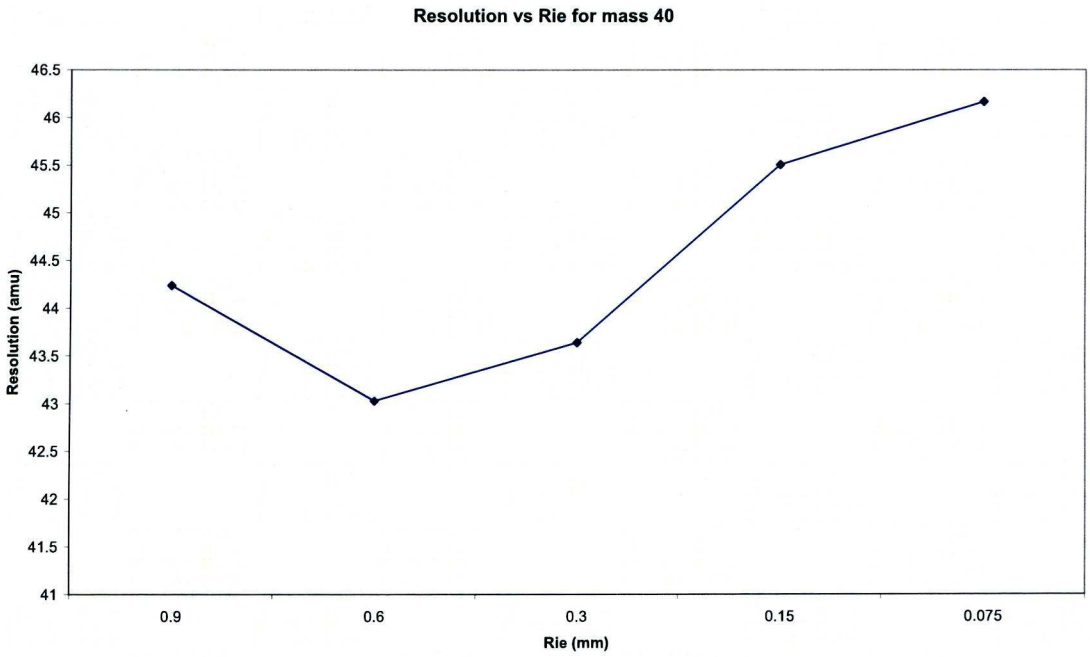

Figure 3.10: Resolution versus Rie for m/z = 40 spectra of Figure 3.8.

Figure 3.11 shows the importance of having a correctly configured lens system with the correct voltages applied to ensure a good collimated beam of ion is produced by the ion source. It is clear that even a small beam spread (e.g. half angle of 12°) significantly reduces the number of ions transmitted through the filter and therefore reduces the instrument sensitivity.

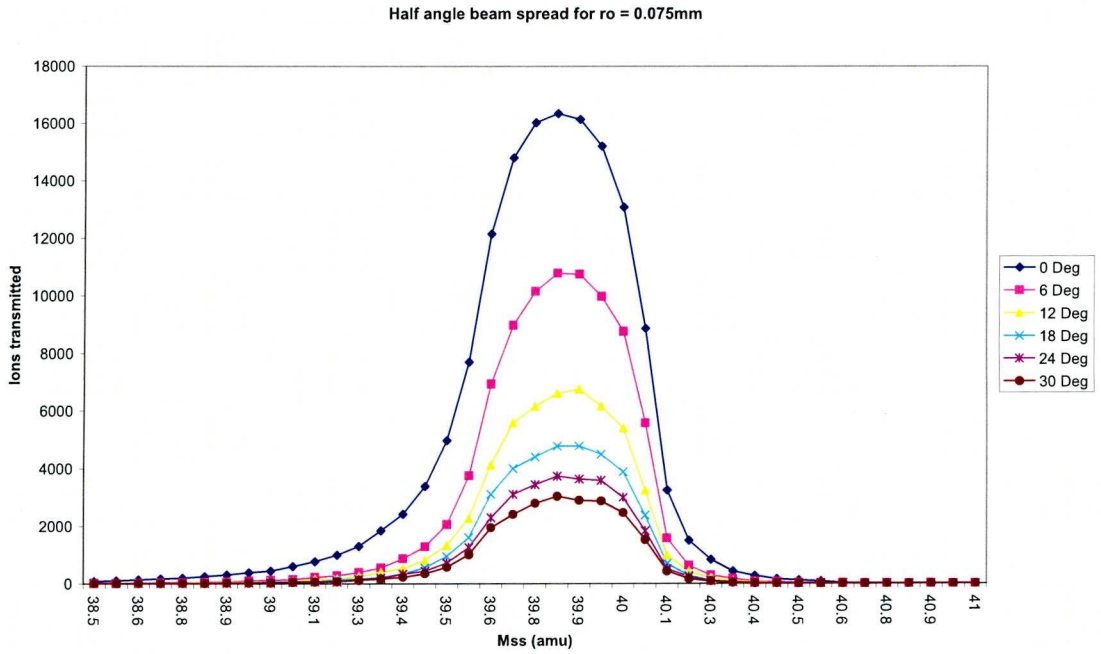

Figure 3.11: Effect of beam spread on m/z = 40 mass spectra (Ro=0.075mm).

3.5 Experimental

Two QMF hyperbolic mass filters were built, tested and then the results were simulated using the QMS2-H program. The first QMF was a miniature hyperbolic QMF constructed using Electro Discharge Machining (EDM) with length 40mm and r_o=0.9mm. The second was a QMF constructed using the Digital Light Processing (DLP) technique (described later), of length 55mm and also r_o=2mm. Both QMF's are shown in figure 3.12.

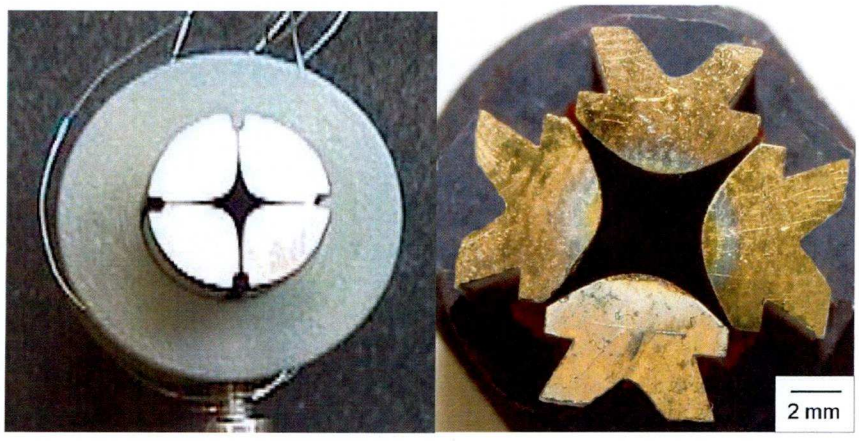

Figure 3.12 (left) EDM QMF (r_o=0.9mm) (right) DLP QMF (r_o= 2mm) fabricated using gold coated PMMA electrodes in insulating PMMA housing.

Both QMFs were assembled onto standard 2.75 inch vacuum flanges with EI ion sources (described below) to make functioning QMS instruments. In the case of the EDM QMS a multiplier option was available and used in addition to Faraday cup detection. These QMS were then incorporated into a vacuum system pumped by a rotary vacuum and Edwards Turbo combination (base pressure 1.5x 10^{-7} bar). The same electronic control unit (ECU) was used to test both instruments. The specifications for the ECU are given in appendix 3.1. The optimised ion source described and simulated earlier was coupled to the miniature EDM QMF (r_o= 0.9mm), for the DLP QMF (r_o=2mm) a standard commercially available 2 plate ion source was used.

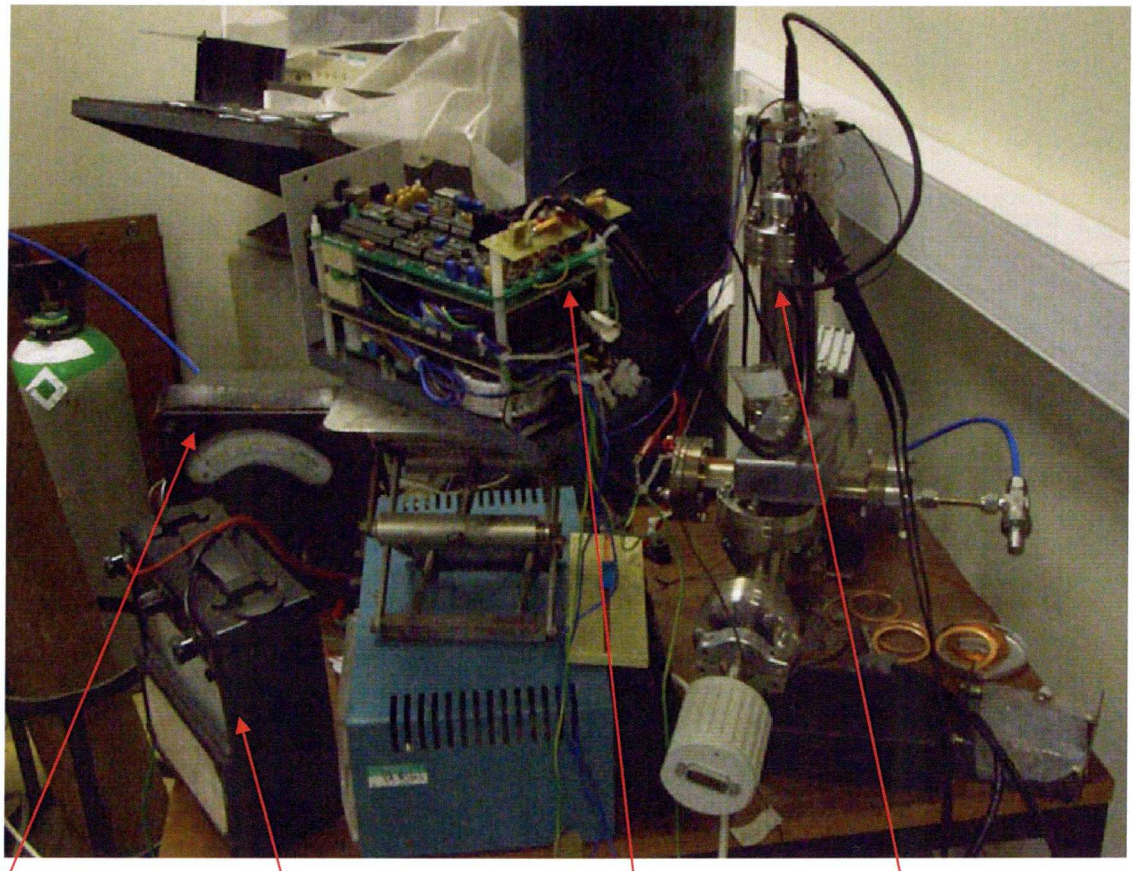

Figure 3.13 Experimental set up used for testing the hyperbolic QMF.

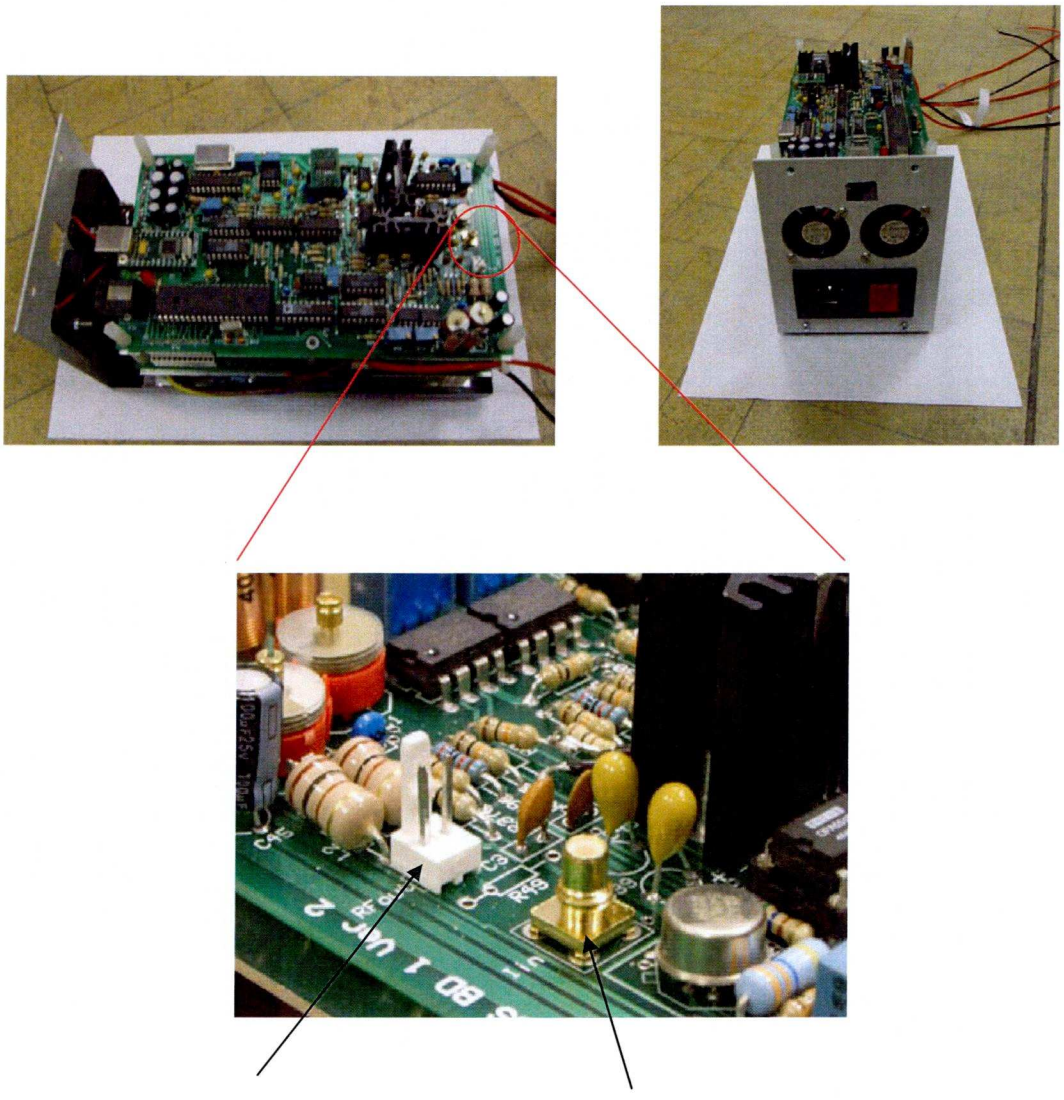

Figure 3.14: Photos of ECU used for hyperbolic QMS testing (operating frequency 3.686 MHz). The ECU was coupled via a USB port and controlled from a PC.

3.5.1 Results for EDM QMF (R_0= 0.9mm)

3.5.1.1 Coupling of miniature ion source to EDM QMF

Mass spectra were obtained for a range of ion source operating conditions and the effect on QMS resolution and sensitivity were investigated. The experiment was carried out using 3 different ion energies (3eV, 5eV, 7eV). The following voltages were applied to the plates: extract potential 0 to -25V (5V increments), focus potential: 0 to -30V (5V increments)

Figure 3.15 shows the raw data obtained from the experiment for 5eV. The full set of individual plots can be seen in appendix 3.2. It can be seen in figure 3.15 that there is a problem with baseline drift which was found to affect all the scans. To calculate the correct resolution and sensitivity, post processing of the raw data was performed in Excel to correct the baseline drift and figure 3.16 shows the corrected spectra. A facility to zero the baseline was subsequently added to the ECU control software removing the need to perform any post processing on the recorded data.

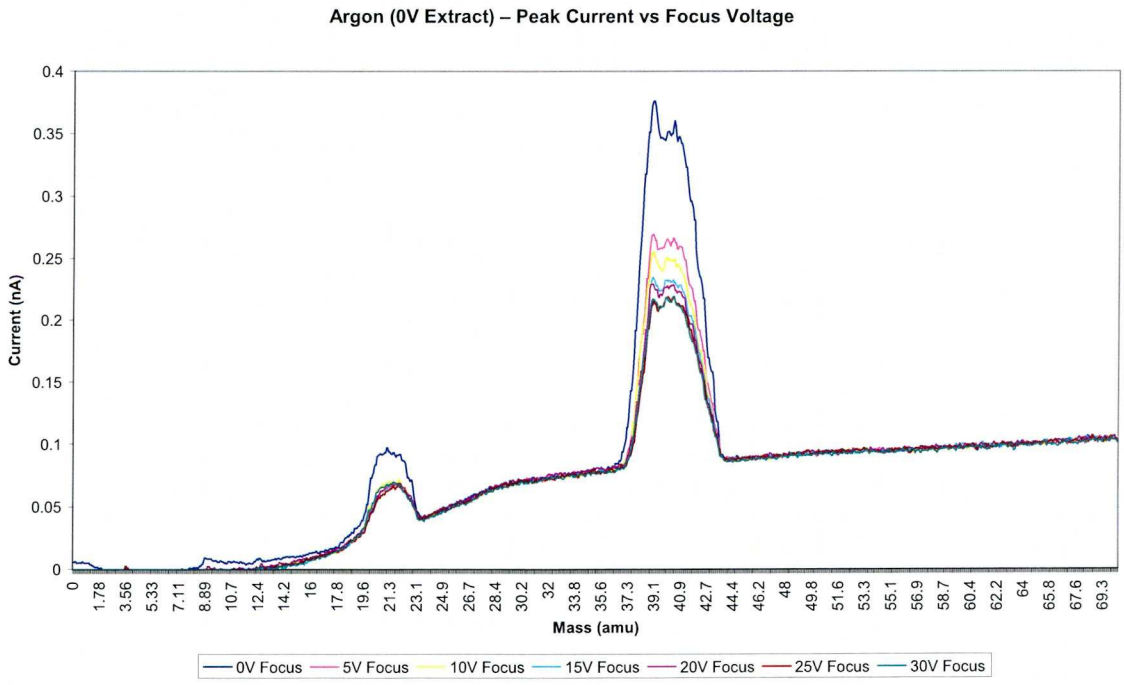

Figure 3.15: Argon spectra (raw data) before post processing to correct baseline drift.

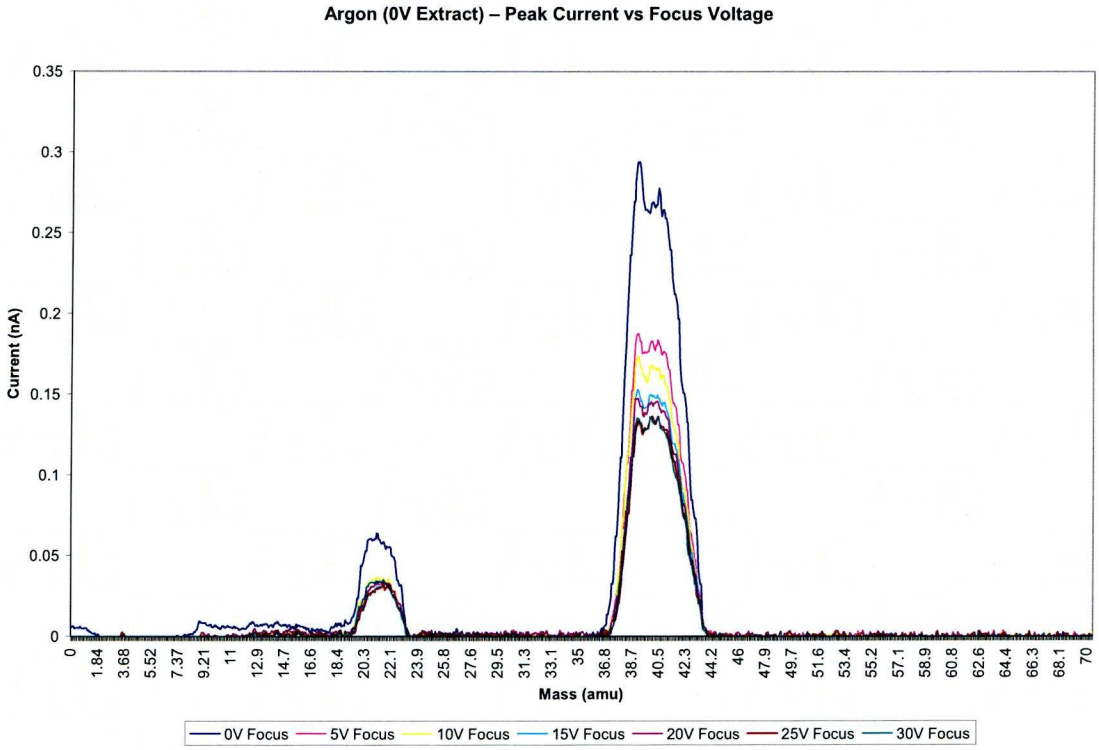

Figure 3.16: Corrected spectra for Argon obtained using the EDM hyperbolic QMF.

Figures 3.17 and 3.18 show the resolution and sensitively for each of the 42 test voltage combinations used. This data was used to optimise the ion source coupling to the EDM QMF, e.g. for optimum resolution -25V for the extract and -20V for the focus is necessary.

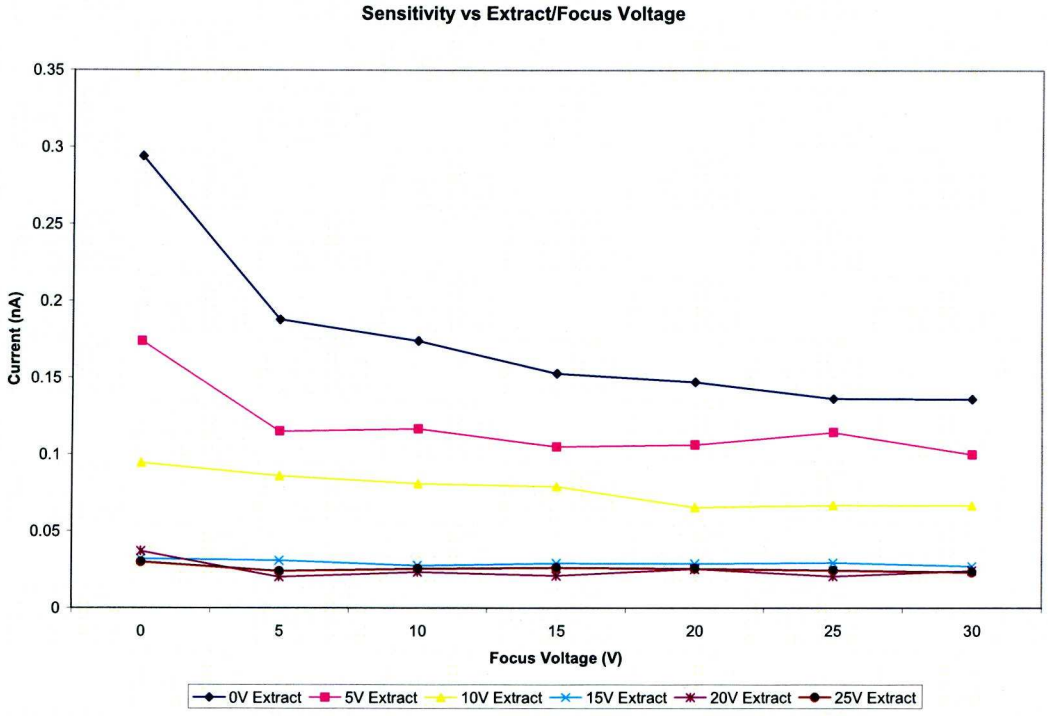

Figure 3.17: Detector ion current as a function of ion source conditions.

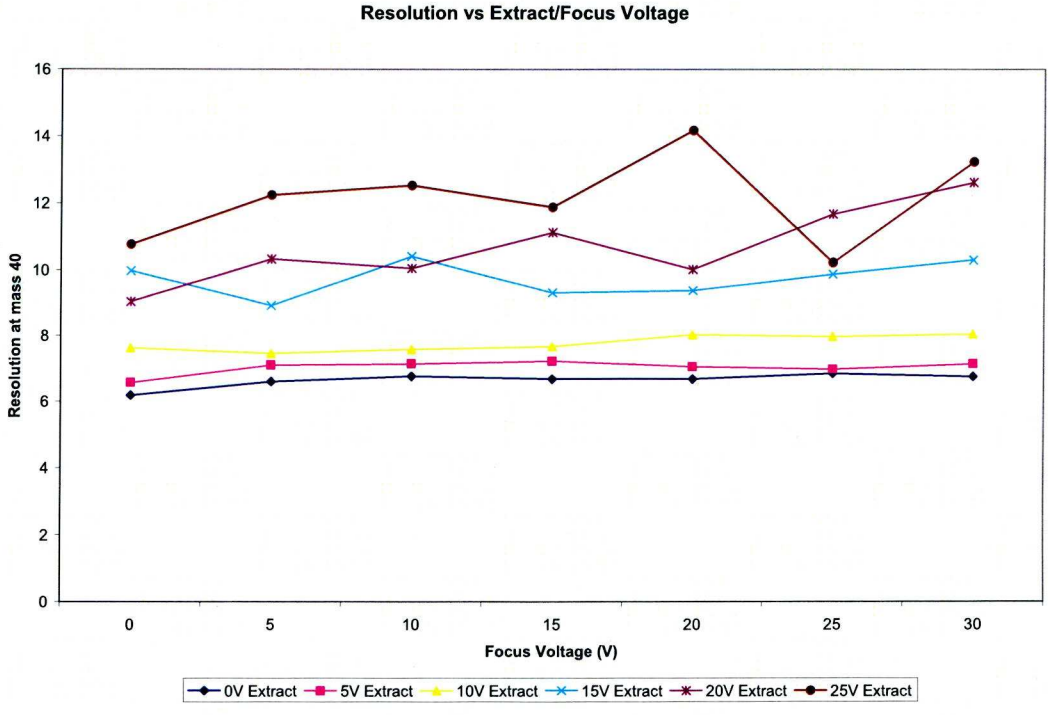

Figure 3.18: QMS Resolution for EDM QMF as a function of ion source conditions

The resolutions above are quite low, since the aim of this experiment was not to achieve the maximum resolution but instead to characterize the ion source and observe the relative differences depending on the voltages applied to the lenses.

3.5.1.2 Mass spectra obtained using the EDM hyperbolic QMF

Figure 3.19 shows the spectrum for a helium/air /argon gas mixture obtained using the EDM hyperbolic QMF operated in Zone 1 of the Matthieu stability diagram. Resolution obtained was about 30 with clear peak separation between m/z = 28 and m/z = 32, which is typical for miniature and microengineered systems.

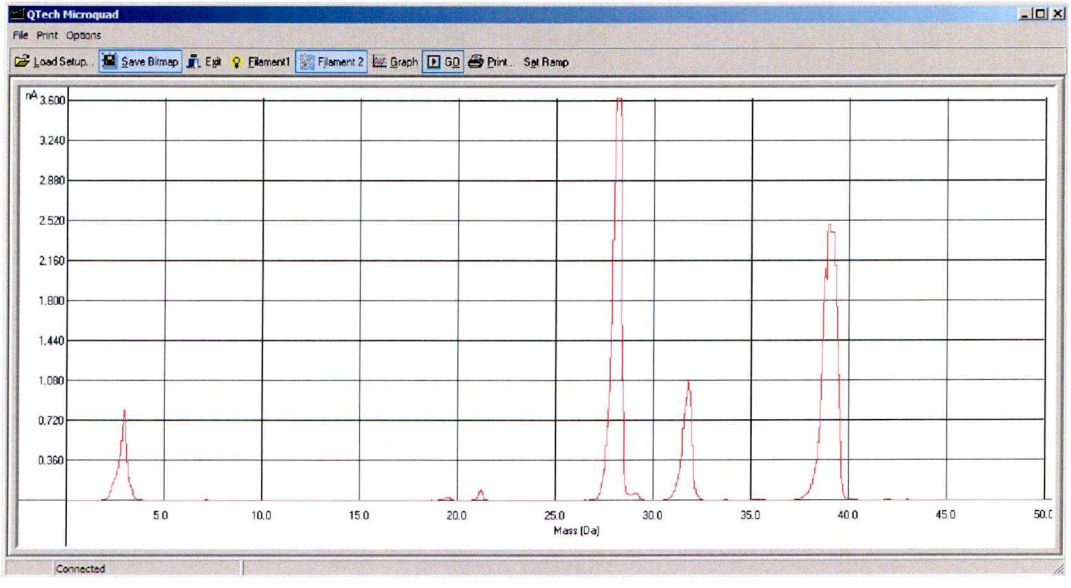

Figure 3.19: Screenshots from the ECU software for helium/air/argon mixture. Pressure = 6.67x10^{-5} mbar. Ion source conditions: extract: -15V focus: -10V.

Mass spectra were also obtained for Zone 3 operation of the EDM QMF. Because of the higher AC and DC voltages required to achieved a zone 3 scan Helium was used because of its low mass and therefore low voltage requirements. Zone 3 spectra are known to differ from zone 1 in the following ways (i) higher resolution can be achieved but at the expense of sensitivity (ii) the instrument can be operated at higher ion energies without significant affect on the resolution[4]. Zone

3 is much smaller region on the stability diagram and for this reason a constant DC scan line was used to make it easier to find the mass spectra shown in figure 3.20.

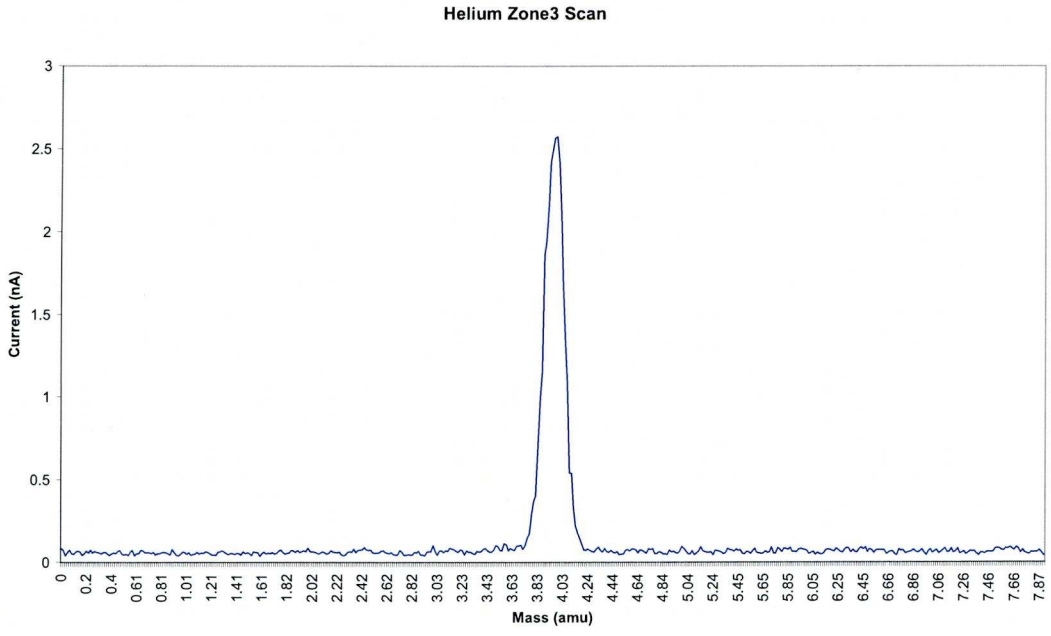

Figure 3.20: Helium zone3 scan for EDM hyperbolic QMF. Pressure = $9.87x10^{-5}$ mbar, ion energy 15eV, electrode offset voltage 0.8V, multiplier 900V, emission current 0.9mA.

The width for the Helium peak shown in figure 3.21 was 0.35 amu and the resolution was calculated to be 11.3. Significant is the absence of the long tail on the low mass side of the spectrum which is characteristic of zone 3 operation. As previously for zone 1 results, a baseline drift correction was employed. This result shows the feasibility of operation in zone 3; further changes to the scan line are expected to result in much higher resolutions.

3.5.1.3 Comparison of experimental and simulated mass spectra for EDM QMF

For single mass spectral peaks it is possible to tune the QMS so as to obtain best case resolution. Figure 3.22 shows the experimental mass spectrum for $^{40}Ar^{+}$ ions obtained from the EDM QMF tuned to optimum performance. The ion source emission current is 0.5 mA, the operating pressure is $8x10^{-5}$ mbar. For this particular mass spectrum the ion source cage voltage and the first lens were set at 3 V, the extract potential was -10 V, the focusing potential is at -25 V and the exit lens is grounded. The QMF was driven with 63.6 V zero-to-peak RF amplitude at 3.6864 MHz. The DC scan voltage was 10.67 V. The QMF resolution at 50% of the peak height is 90.

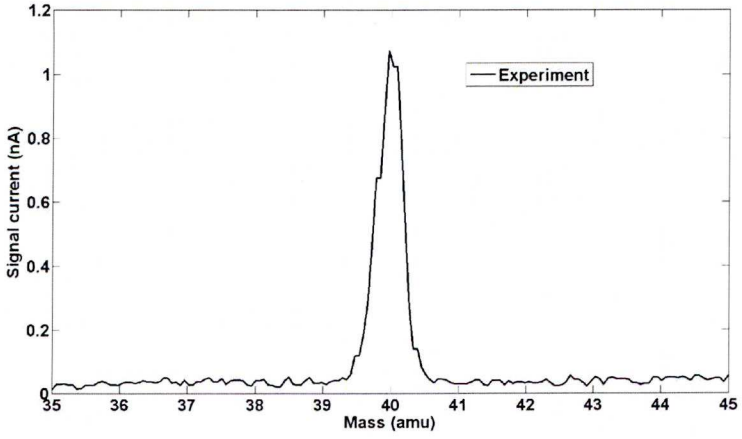

Figure 3.21: Experimental mass spectrum for Argon using the EDM hyperbolic QMS.

Figure 3.22 shows the simulated mass spectra for $^{40}Ar^{+}$ ions in the EDM hyperbolic QMS. This spectrum was generated using QMS-2H with the ion source conditions simulated using CPO to include the effect of space charge. Input parameters for the ion source and the QMF are the same as in the experiment (Figure 3.21). The simulated U/V ratio was set to be 99.3% which provided the best match to the experimental one. The average ion energy when entering the QMF,

determined from CPO was 3.75eV with ion-to-ion space charge included within the ion source. Ion transmission through the QMF was 38.42%. The QMF resolution at 50% of the peak height is 100 and it can be seen from Figure 3.22 that simulated mass spectrum has a good agreement in shape with the experimental spectrum from Figure 3.21.

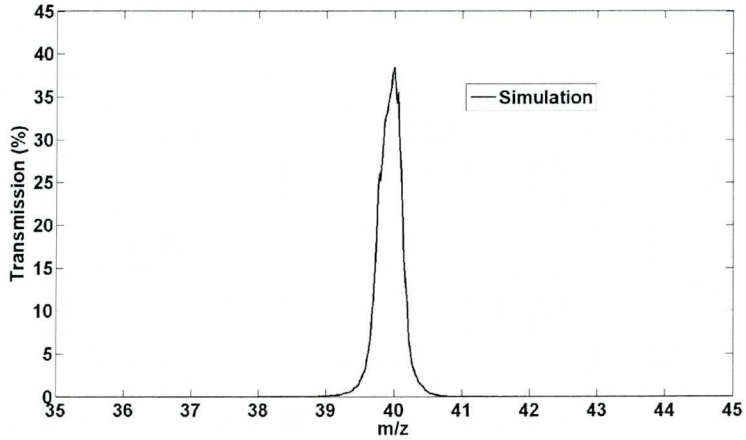

Figure 3.22 Simulated mass spectrum for $^{40}Ar^{+}$ ions in the EDM hyperbolic QMS.

3.5.2 Hyperbolic RP QMF Results

3.5.2.1 DLP QMF fabrication and assembly

The technique used for fabrication of a second hyperbolic QMF is digital light processing (DLP). This was initially invented by Texas Instruments (TI) for video applications. DLP is based on TI digital micromirror device (DMD), which is a MEMS semiconductor chip that contains microscopic mirrors aligned on a matrix. The purpose of micro mirrors is to enable precise control of the laser beams to achieve high resolution video projection. Such DLP laser beams can also be used to cut materials like PMMA (polymethyl methacrylate) and produce any 3D shape with low fabrication errors at micro scale. DLP was used to fabricate PMMA hyperbolic electrodes for a QMF and housing for them. The QMF electrodes were coated with gold by vacuum thermal evaporation to provide electrical conductivity. The resulting surface roughness was at the nanoscale level for PMMA rods and coating.

The advantages of DLP for QMF fabrication are:

(i) 3D polymer structures of any shape can be made at small dimensions (micro-scale)

and coated with metal (e.g. gold) to provide conductivity. (ii) DLP is a low cost technology that offers good tolerances and smooth surfaces for miniature electrode structures, which significantly reduces distortion of ion motion. (iii) DLP can be used for making segmented structures by coating only segments that need to be conductive and leaving the rest of the structure to be insulated. (iv) The DLP technique also has potential for realising a fully integrated mass spectrometer with all of its components built from a minimal number of parts.

Figure 3.23: Coated and uncoated QMF rod after DLP fabrication. The thickness of the gold coating is approximately 1μm. Resistance of the conducting electrode from one end to another is approximately 40Ω.

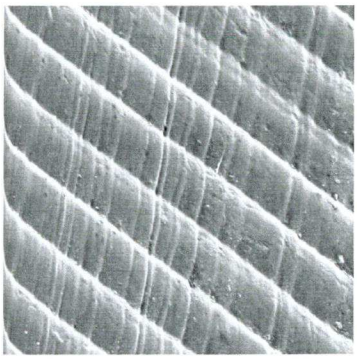

Figure 3.24: Enlarged part of the PMMA rod, taken by scanning electron microscope (SEM). The surface roughness of the DLP rods is 1.5 μm.

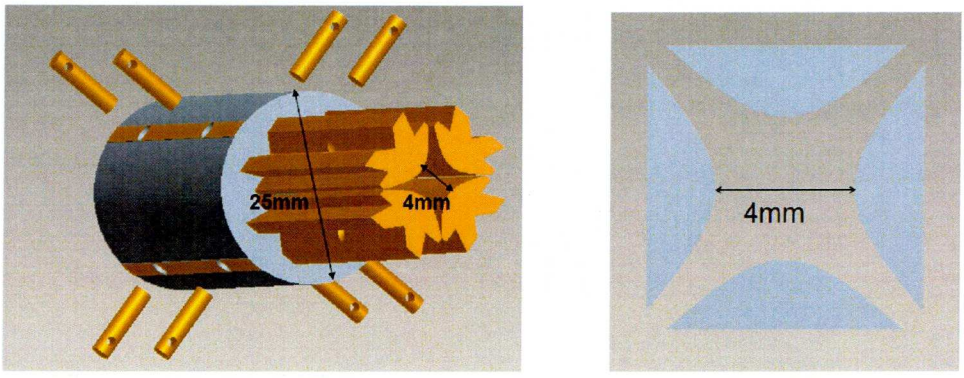

Figure 3.25: PRO/ENGINEER CAD design drawing for the hyperbolic DLP QMF showing the design for the electrode grooves and housing and complete assembly of the QMF with conducting and securing

3.5.2.2 Experimental results from DLP QMS

Testing of the DLP QMF was undertaken, first using RF only QMF excitation, with an ion source extraction potential of -40V, emission current 0.6mA and ion energies in the range 3-8eV. The results are shown in figure 3.26.

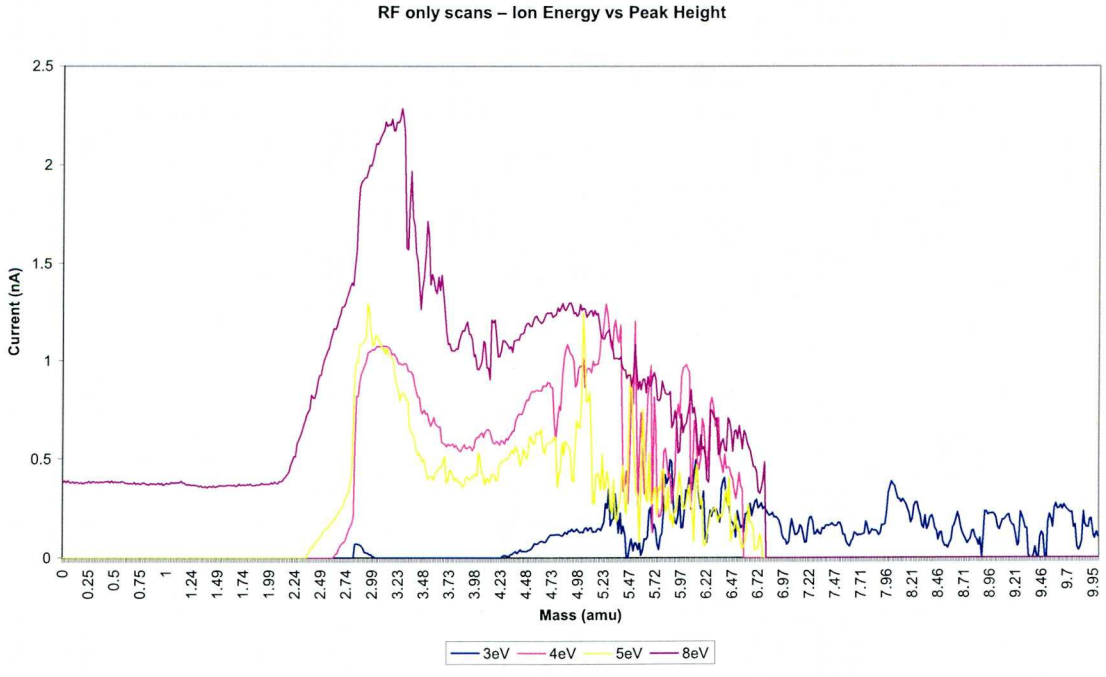

Figure 3.26: RF only scan for DLP QMF – total ion current against ion energy Pressure = $8x10^{-5}$ mbar (Helium).

Figure 3.27 shows the detector current measured with the variation of ion energy for RF only scans shown in figure 3.26.

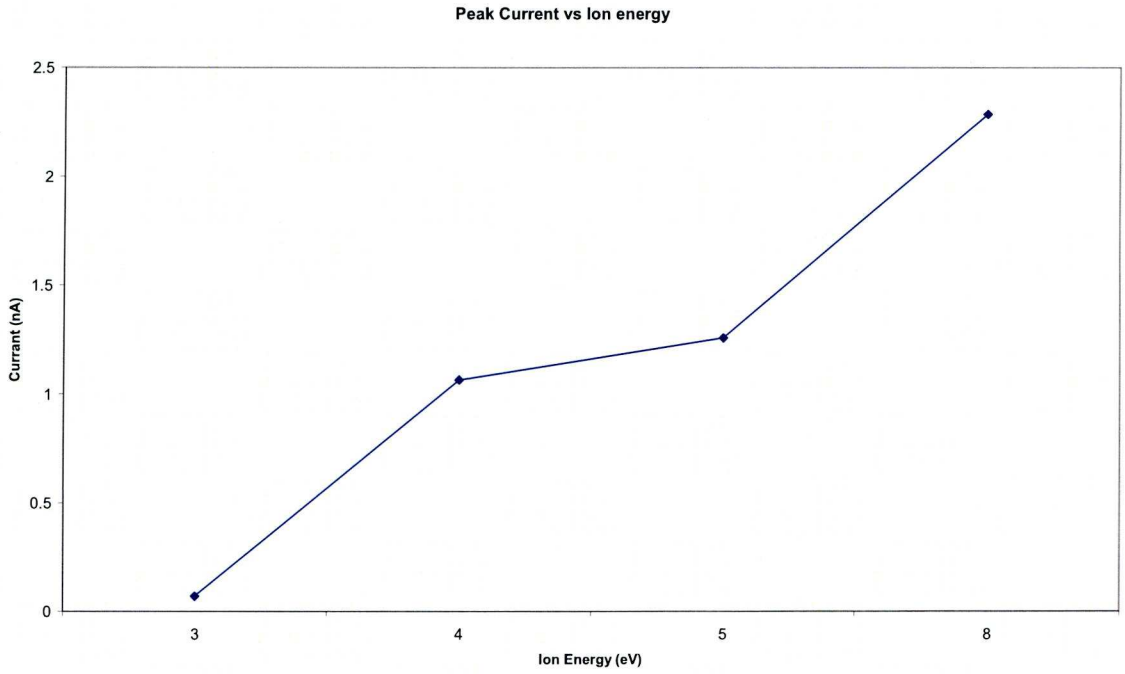

Figure 3.27: Total ion current versus ion energy for the DLP QMF.

As the energy is increased more ions are injected and of those injected more are transmitted through the filter to the detector with consequent increase in measured ion current. This behaviour is as expected and entirely in line with conventional QMF operation.

The next test was to operate the DLP QMF with DC voltage and to observe whether mass filtering occurs. Figure 3.28 shows the results obtained with emission current of 1mA and extract potential -40V for Helium gas.

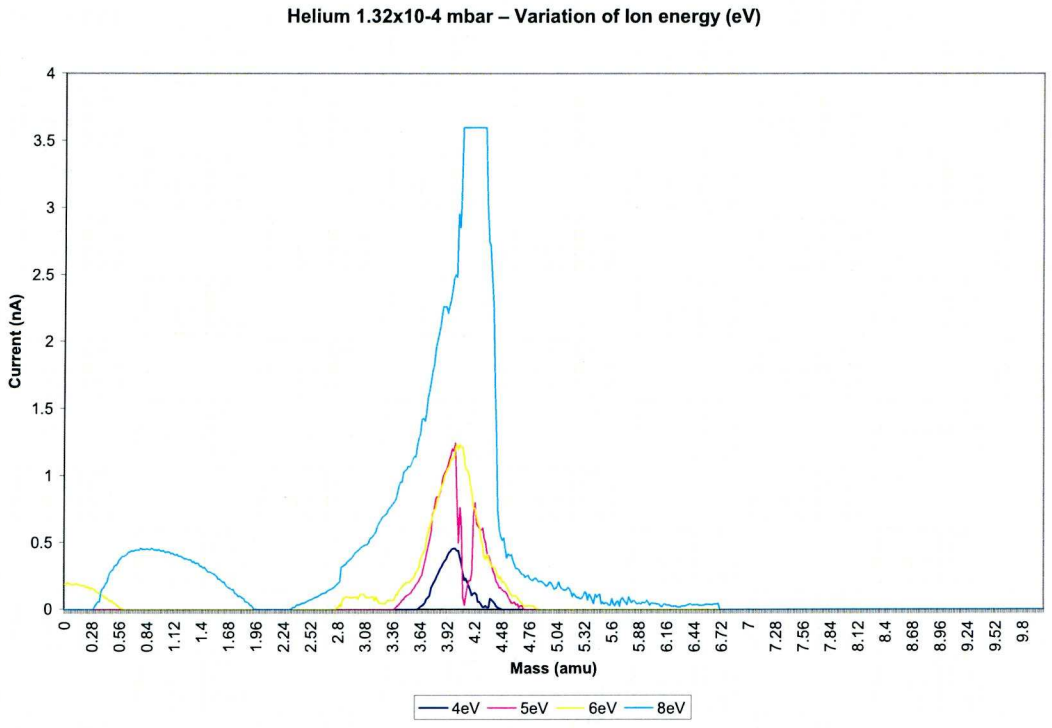

Figure 3.28: Variation of ion current with ion energy for Helium spectra (DLP QMF).

As observed for the previous RF only scans, as the ion energy in increased there is an increase in ion transmission (peak height) and the expected widening of the peak because the ions are moving faster through the filter and therefore experience less RF cycles, at 8eV the peak current saturated the picoammeter which resulted in a clipping effect. Figure 3.29 shows the peak current versus ion energy for the data presented in figure 3.28.

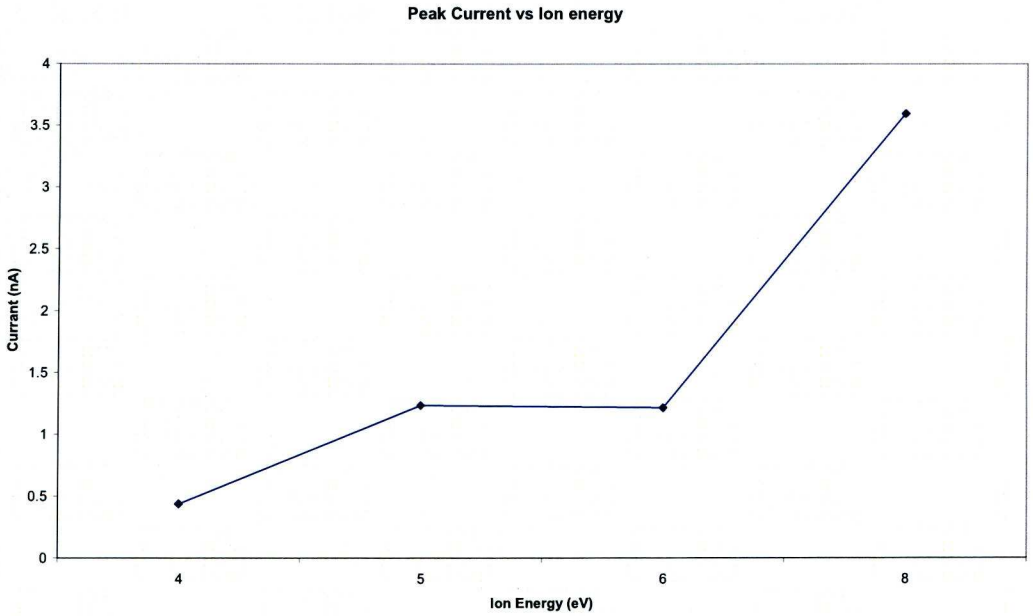

Figure 3.29: Peak Current against ion energy for data shown in figure 3.28.

Figure 3.30 shows the performance of the DLP QMF with pressure over the range $4x10^{-5}$ to $3.2\ x10^{-4}$ mbar.

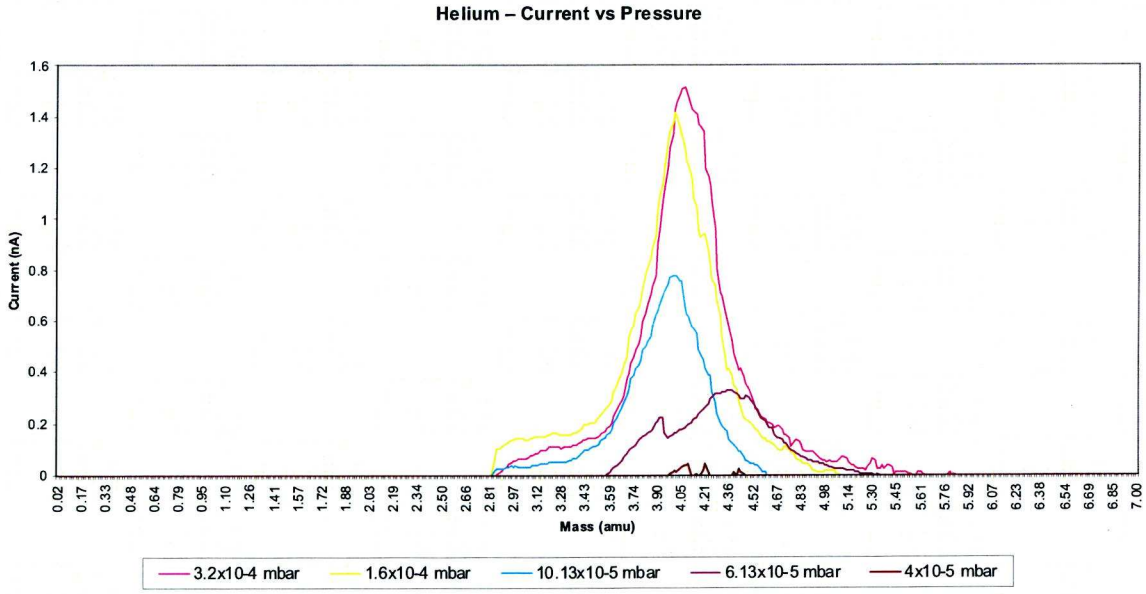

Figure 3.30: Ion current versus pressure for the DLP QMS. Emission Current:1.2 mA, ion energy: 6eV, extract Voltage: -40V.

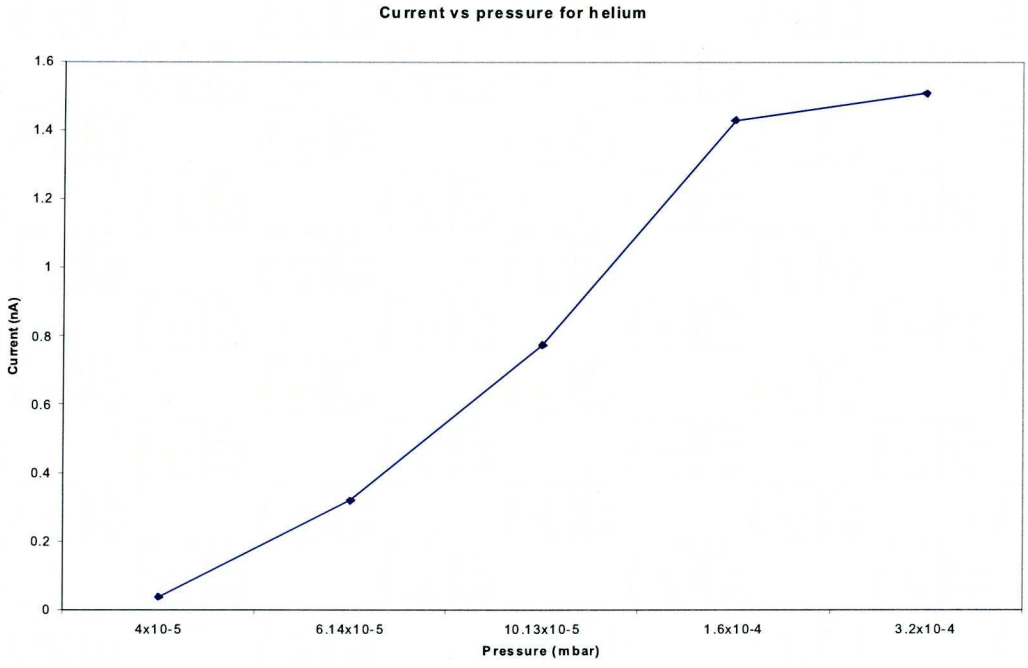

Figure 3.31: Ion current versus pressure for DLP QMS.

As expected, as more of the helium gas is present more helium ions are produced and therefore more ions are available to enter the mass filter. The general linear trend is seen up to $1.6x10^{-4}$ mbar at which point the curve begins to saturate possibly due to the decrease in mean free path leading to increased ion –neutral collisions in the QMF and fewer ions being transmitted.

To obtain the best possible resolution the DC/RF ratio was varied from 0.04 – 0.115 and the results are shown in Figure 3.32 at a Helium pressure of $1.33x10^{-4}$ mbar.

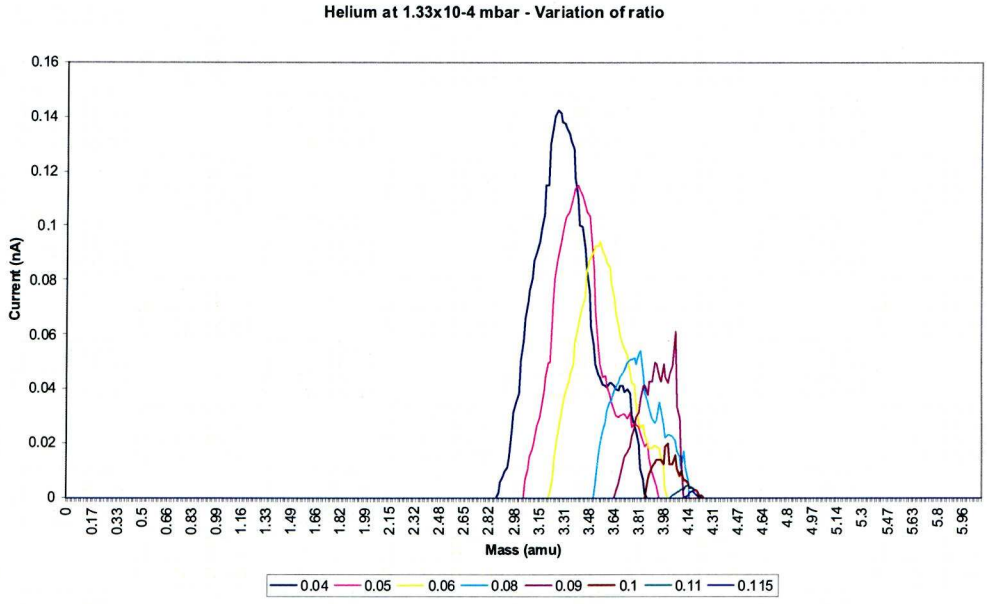

Figure 3.32: Variation of RF/DC ratio and effect on peak height and shape.

As the ratio is increased the resolution increases but there is a slight peak shift along the mass scale further to the right. This shift in the mass scale would need to be corrected in any real instrument. The DC/RF ratio versus instrument resolution is shown in Figure 3.33. A maximum resolution of 70 was the best obtained at this pressure.

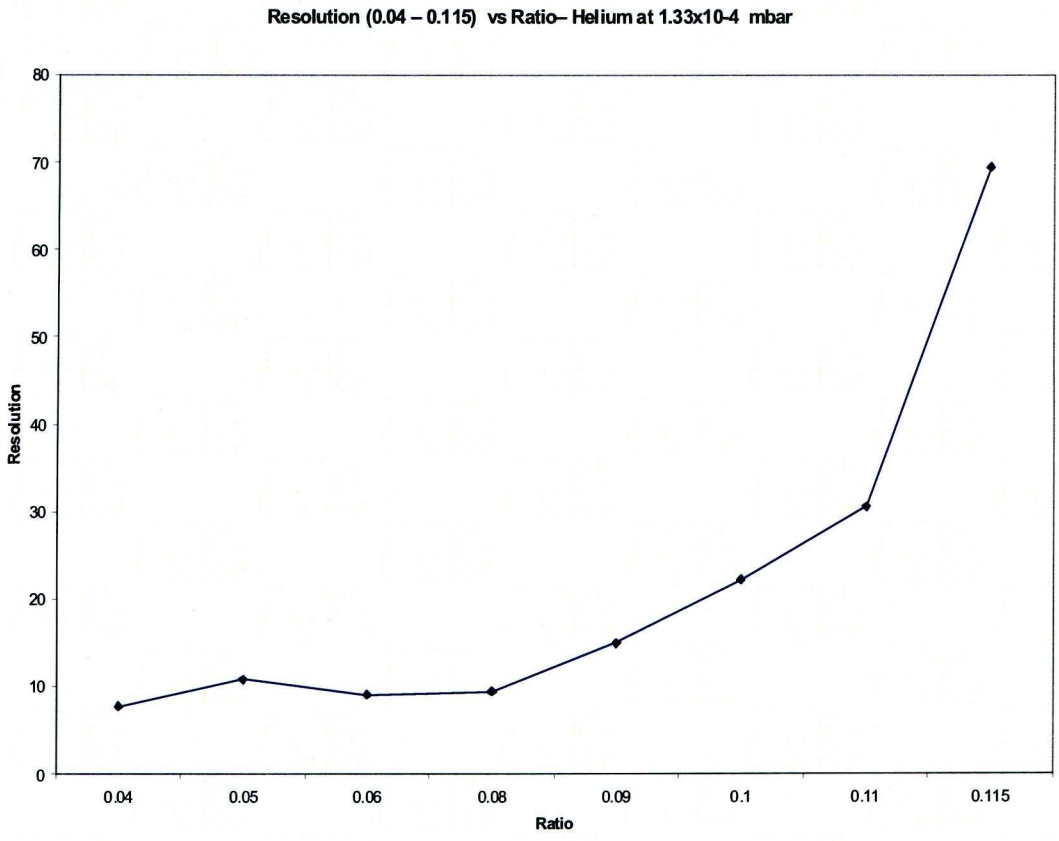

Figure 3.33: DC/RF voltage ratio versus instrument resolution for DLP QMF.

As expected from the QMF theory earlier described, as the ratio is increased (i.e. the scan line moving further up the stability curve) the resolution also increases. There is a corresponding decrease in ion current (transmission) and this is shown plotted in figure 3.34.

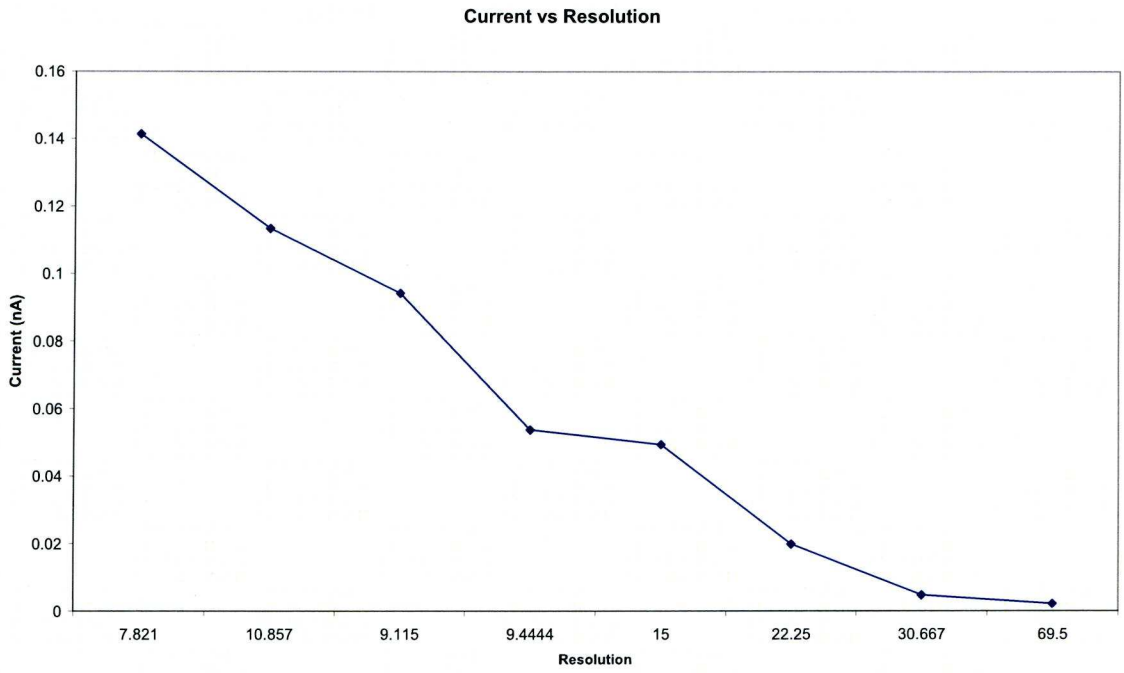

Figure 3.34: Decrease in ion transmission with increasing sensitivity for DLP QMF.

Figure 3.35(a) shows the experimental mass spectra obtained from the DLP QMF optimised for repeatable operation with excitation voltages of V_{RF} of 17.66V (peak) and U_{DC} = 2.96V, the ion energy = 3V, extract potential -40V, emission current 0.6mA and pressure 1.32×10^{-4} mbar. Figure 3.35(b) shows the experimental mass spectrum for He/Ne gas mixture with 50:50 ratio, with resolution of 13 for $^{4}He^{+}$ ions and resolution of 30 for $^{20}Ne^{+}$ ions at 50% of the peak height.

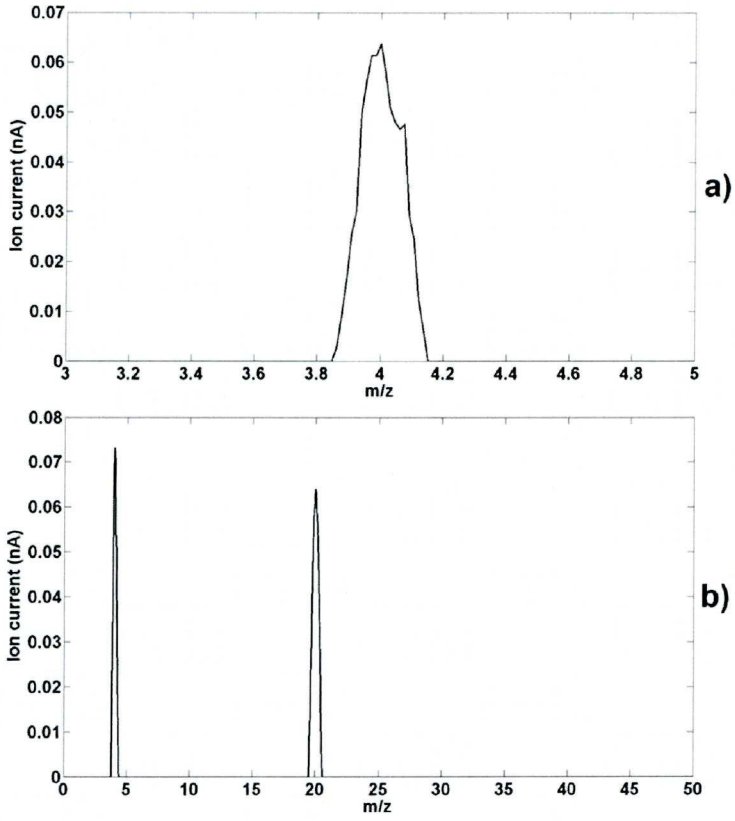

Figure 3.35 (a) Experimental mass peak for $^{4}He^{+}$ ions with resolution of 25 at 50% of the peak height, which is the maximum resolution achieved (b)Mass spectrum for He/Ne gas mixture with 50:50 ratio.

The ECU in this case of the above spectra were operated with zero noise on the baseline which may account for the absence of the $^{22}Ne^{+}$ ion (should be 2% of peak value at m/z =20). These are not the maximum measured resolutions that could be obtained, but rather resolutions that can easily be repeated each time when running the experiment. By improving the coating on the electrodes to increase conductively and surface finish, the resolution can further be improved.

3.6 Conclusions

In this chapter the theory underlying the hyperbolic QMF has been rehearsed. Two novel types of hyperbolic form QMF have been described (i) a metal hyperbolic mass filter fabricated using EDM and (ii) a DLP produced mass filter. Both QMFs are suitable for use in portable QMS systems. QMS instruments made with both types have been realised and tested. A QMS numerical simulation has been used to optimise ion coupling into the miniature EDM QMF and to predict mass spectral peak shapes in this case. The results for each novel QMF have been presented and explained and shown to be in line both with the theoretical description and also with the QMS simulation program. The DLP method is a true microfabrication technology and offers the potential to obtain smaller QMF geometries than have been obtained so far.

References

[1] P.H. Dawson, *Quadrupole Mass Spectrometry and its Applications.* Elsevier, Amsterdam, (1976).

[2] T.J.Hogan and S.Taylor, *'Performance simulation of a quadrupole mass filter operating in the first and third stability zones'* IEEE Trans. on Instrumentation and Measurement, **57** (3) pp.498-508 (2008)

[3] J.R.Gibson and S.Taylor, *'Asymmetrical features of mass spectra peaks produced by Quadrupole Mass Filters'* Rapid Communications in Mass Spectrometry, **17**, pp.1051-1055, (2003)

[4] S. Hiroki, T. Ebe and Y. Murakami, *Development of a high-resolution quadrupole mass spectrometer capable of detecting ^{3}He and ^{4}He in a hydrogen isotope atmosphere,* J. Vac. Sci. Technol. **A 12**, (5), pp.2711-2715, (1994).

[5] J.R.Gibson, S.Taylor and J.H.Leck, *'Detailed simulation of mass spectra for quadrupole mass spectrometers',* J.Vac. Sci and Tech. **A18** (1), pp.237-243, (2000)

[6] J.R.Gibson and S.Taylor, *'Prediction of Quadrupole Mass filter performance for hyperbolic and circular cross section electrodes*, Rapid Communications in Mass Spectrometry, **14**, pp. 1669-1673 (2000).

[7] S.Taylor and J.R.Gibson, *'Prediction of the effects of imperfect construction of a QMS mass filter*', J. Mass Spectrometry, **43,** pp. 609-616 (2008)

[8] T.J. Hogan and S.Taylor, *'Effects of mechanical tolerances on QMF performance for operation in the third stability zone'*, submitted to IEEE Trans. on Instrumentation and Measurement (2009)

Chapter 4

Ion source design using Carbon nanotubes

In this chapter nanotubes are investigated as a possible electron emission sources. The main areas of investigation are how effective the nanotubes are as electron emitters when subject to high electric fields and how they degrade over time.

4.1 Brief History of Carbon Nanotubes

Metals, such as molybdenum, were originally used for field emission (FE) sources [1] but problems during FE arose due to the cathode tips becoming extremely hot and causing local melting, damaging the geometric characteristics (sharp points) needed to create the electric field required for FE. The heating of the metal cathodes also leads to chemical reactions with the residual gases in the vacuum further reducing their FE capabilities [1]. The biggest problem in using metals for FE is that the metal must be mechanically shaped in order to obtain effective FE. These problems where solved by Sumio Ijima in 1991 [2], when he discovered multiwalled carbon nanotubes [CNT]. A further solution was presented two years later when he and Donald Bethune at IBM independently observed single-wall nanotubes [3]. This was an idea originally devised in 1990 by Dr. Richard Smalley who commented on the possibility of tubular 'buckyballs', (sixty carbon atoms arranged in a soccer ball shape, also known as Fullerene Spheres, which was discovered in 1985), as shown in Figure 4.1 [4].

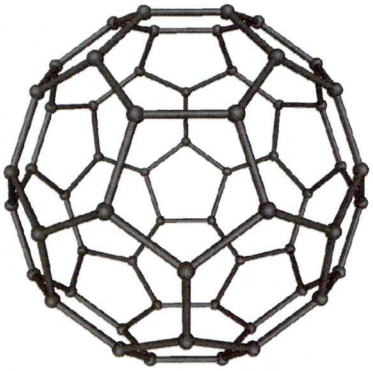

Figure 4.1: Buckminsterfullerene C_{60} [9].

CNTs are created when a sheet of graphene (a single layer of graphite atoms) is cut with the hexagons aligned parallel to the tubes circumference [5]. When the width approaches 30nm it becomes more energetically favourable for this very narrow strip of graphite to curl up into a cylinder [1]. It is easier to produce nanotubes from strips which are three to eight sheets thick. This type of nanotube is known as a Multiwalled Nanotube (MWNT). Single Walled Nanotubes (SWNTs), which are produced from a single sheet of grapheme are not as easy to manufacture. However, they will be used in this project as they have been shown to be much better field emitters compared to MWNTs [6].

MWNTs typically have a diameter in the range of 10 to 50 nm, and a length more than 10μm, whereas SWNTs are much thinner with a diameter of around 1.0 to 1.4nm and generally have a length of around 100μm. This higher aspect ratio is vital for good field emission [6]. In addition to coming in SW and MW nanotubes can also be capped or open ended. The tubes are terminated at the bottom using hydrogen to saturate the carbon dangling bonds; they can be seen in Figure 4.2. The capped nanotubes are made up of open ended nanotube cylinders with a Fullerene hemisphere capping the top [7]. These tubes have high aspect ratio and small radii of curvature at their caps.

Carbon nanotubes are composed entirely of sp^2 bonds, similar to graphite, these bonds are stronger than the sp^3 bonds found in diamond. This bonding

structure provides them with unique strength. The geometric characteristic of nanotubes, together with high chemical stability and high mechanical strength [8], is advantageous for field electron emitters [5]. CNTs are capable of either display metallic like conducting properties or semi conducting properties. Capped nanotubes have been shown to have metallic like characteristics displaying almost perfect metallic like screening of external electric fields. The field induced polarization of electrons in the tube results in charge accumulation at the tube tips. This contributes to an increased concentration of the external electric field around the tip of the tube [5, 8].

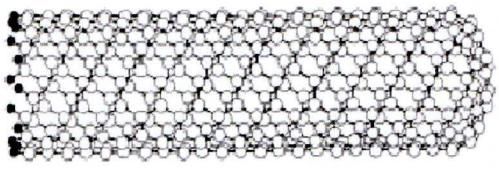

Figure 4.2: Example of a Single Walled Nanotube. The hydrogen is shown as the solid spheres at the end. It can be seen that the tube is capped and much longer than it is wide [5].

As mentioned earlier, the tubes have a high aspect ratio and as charge concentrates at the places of greatest curvature, more charge will be found at the tip or cap of the conductor, effectively concentrating the electric field [1], shown in Figure 4.3. This is known as the field enhancement factor γ, which should reduce the magnitude of the external electric field required to commence FE [5]. This is one of the main advantages of carbon nanotubes as field emitters over metals, as nanotubes naturally have this desired shape, whereas metals must be manufactured to this more pointed shape.

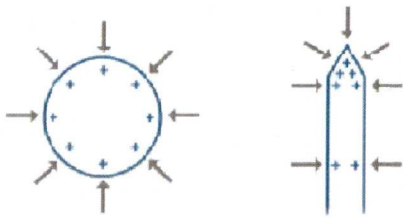

Figure 4.3: Concentrated charge distribution at a point compared to uniform charge on a surface. [1]

The current density produced by a given electric field is governed by the Fowler-Nordheim equation:

$$J = 6.2\times10^{-12}\frac{\sqrt{f/\phi}}{f+\phi}\varepsilon^2\exp\left(-6.8\times10^3\frac{\phi^{3/2}}{\gamma\varepsilon}\right), \tag{4.1}$$

where ε is the applied electric field in $V/\mu m$, while ϕ and f are the work function and energy difference between the top of the valence band and the Fermi level, respectively, and are both measured in eV [9]. This is a detailed equation which has been calculated for electrons with kinetic energies in the range $0 \leq E \leq \phi$ [5]. The work function ϕ is the most important parameter in FE, as it represents the energy needed to excite an electron from the Fermi level to the field free vacuum outside the surface of the material, and is influenced by two factors: the potential difference between the state of the electron in the material and the vacuum, and the electrostatic surface to the emitted electron, known as image potential [5]. Taking these effects into account, equation (4.1) can be modified to:

$$J = S\frac{1.54\times10^2(\beta V)^2}{\phi}\exp\left(-\frac{6.83\times10^3\phi^{3/2}}{\gamma V}\right) \tag{4.2}$$

where S is the fraction of the area emitting electrons, the electric field (in μm) will be $F = \gamma V$, and γ is the field enhancement factor, which reflects the geometry of the emitting area [9].

4.2 Experimental

The nanotubes where produced using a carbon arc submerged in liquid nitrogen and stored in xylene [10]. Before drop casting onto an aluminium plate to cover an area of $1cm^2$, the nanotubes are mixed with P3HT which is a regioregular conducting polymer to help them bond with the aluminium plate being used. The composite is produced by first melting the polymer Poly (3-Hexylthiophene), and adding the xylene/nanotube solution to the liquid polymer. The nanotube composite is shown in Figure 4.4.

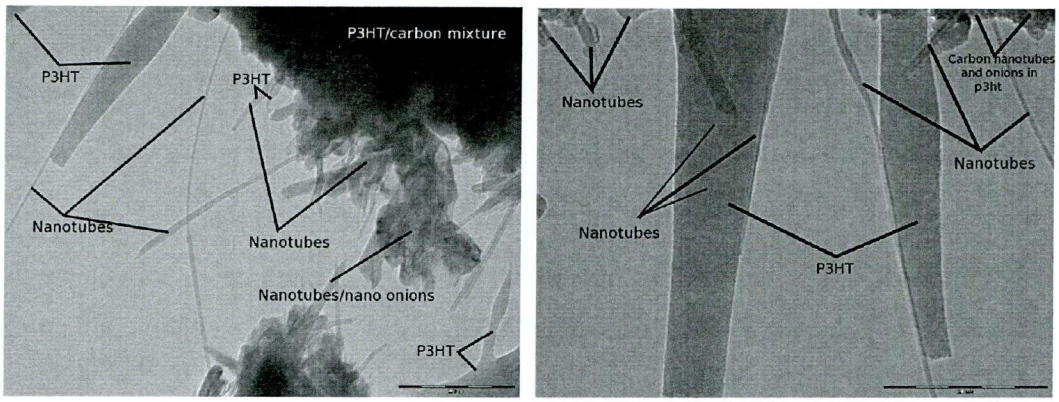

Figure 4.4: SEM image of composite carbon nanotube and Poly (3-Hexylthiophene) mixture, 200nm scale.

Figure 4.5 below shows the basic setup for testing the nanotubes. It consists of two aluminium plates: the bottom one, which is coated with carbon nanotubes and is the emitter, and the top one, which is used to detect the emitted electrons. A high voltage power supply is used to supply voltages in the range of 50-1500V and the voltage measured across the 1.8M Ohm resistor is recorded so that the emission current can be obtained.

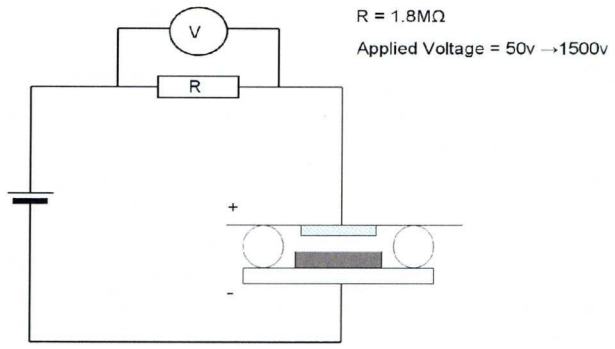

Figure 4.5: Schematic diagram of basic test circuit for CNT field emission tests

The device holder used to mount the aluminium plates is shown in Figure 4.6. It consists of a thick aluminium base with an adjustable PTFE top that holds the two plates shown in Figure 4.5 together. The coated aluminium plate is placed on the base of the device holder; two 0.1mm glass fibres are used as spacers; a second aluminium plate is placed on top of the fibres and clamped down with the PTFE top to ensure no movement can occur.

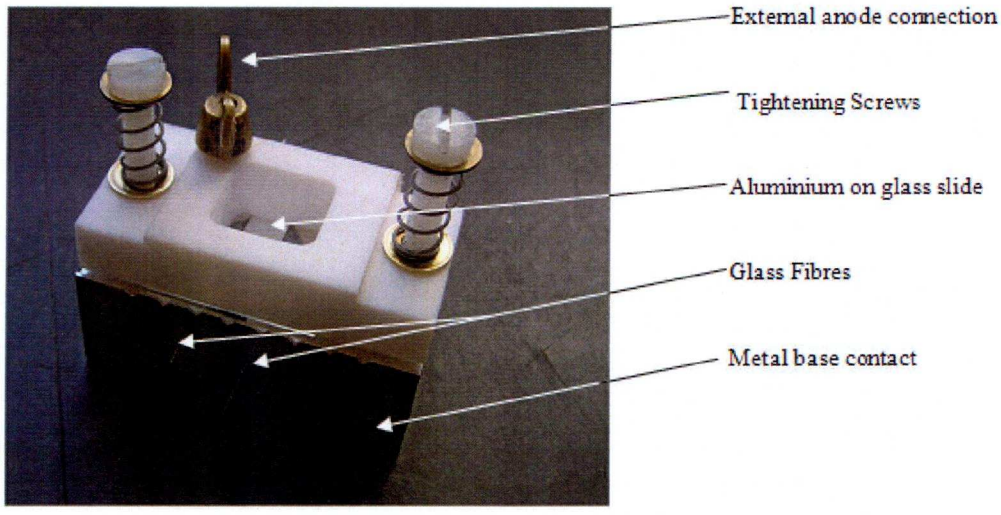

Figure 4.6: Device holder for CNT FE tests

Before results can be taken, the two plate assembly is placed into a vacuum chamber, and using a rotary and turbo molecular pump, a pressure of $8x10^{-6}$ mbar is achieved. Figure 4.7 shows a photograph of the experimental apparatus consisting of the vacuum chamber, power supply, multimeter etc.

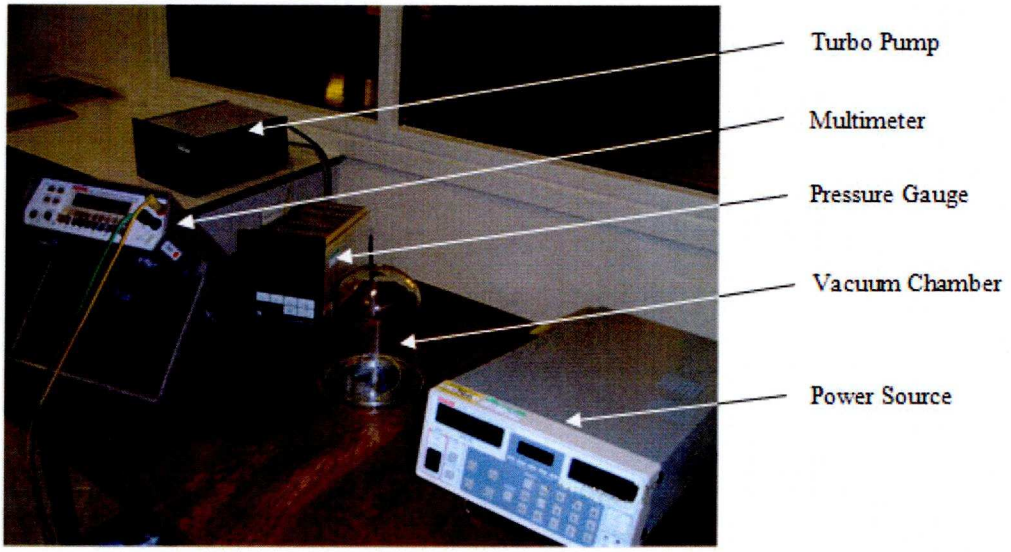

Figure 4.7: Test apparatus including power supply, multimeter, and pressure gauge.

4.3 Results

The initial emission tests were unsuccessful since the nanotubes did not bond well to the aluminium plate. As a result, once the applied voltage of around 300V was applied, the nanotubes were dislodged from the plate and were attracted to glass fibres, which resulted in a short circuit between the two plates.

A new composite nanotube mixture was produced to improve the bonding between the nanotubes and the aluminium plate. This solved the bonding issue and a few tests were done to ensure the nanotubes were emitting. The next step was to use a laptop running the LabVIEW, a software package to automatically ramp the

voltage in fixed steps and record the reading from the digital multimeter. The schematic diagram for this experimental setup is shown in Figure 4.8.

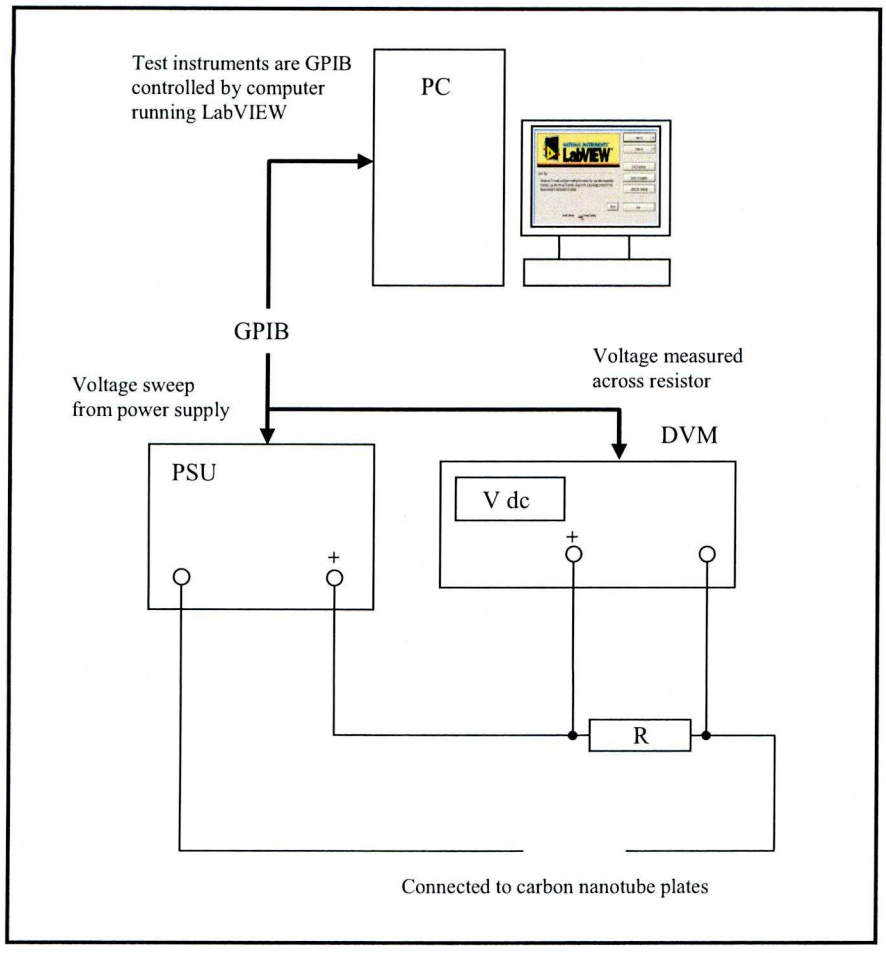

Figure 4.8 Schematic diagram of test setup.

LabVIEW is a programming environment in which programs are created by manipulating graphical objects. This approach differs from traditional programs which use code written in text, on a line-by-line basis. Traditional programs involve data being acted upon by a sequence of program instructions. LabVIEW, however, operates on a principle of 'dataflow' whereby data can be seen to flow pictorially along the connections made between objects in a block diagram. LabVIEW [11] was originally developed by National Instruments around the 1980's specifically for data acquisition and instrument control.

A powerful aspect of this approach is that a Virtual Instrument could be customised to satisfy the specific requirements of any measurement system. Front panels can be created with dials, controls and indicators etc, all designed with a particular function in mind. Each adjustment of a control using 'mouse and keyboard' will have a real effect on a corresponding valve, sensor or item of test equipment within an actual system.

Figure 4.9 below shows the functions responsible for incrementing the high voltage power supply and recording the data from the digital multimeter. The actual interface that allows the user to control the start and end voltages (GUI) as well as the sweep rate and step voltage can be seen in Figure 4.10.

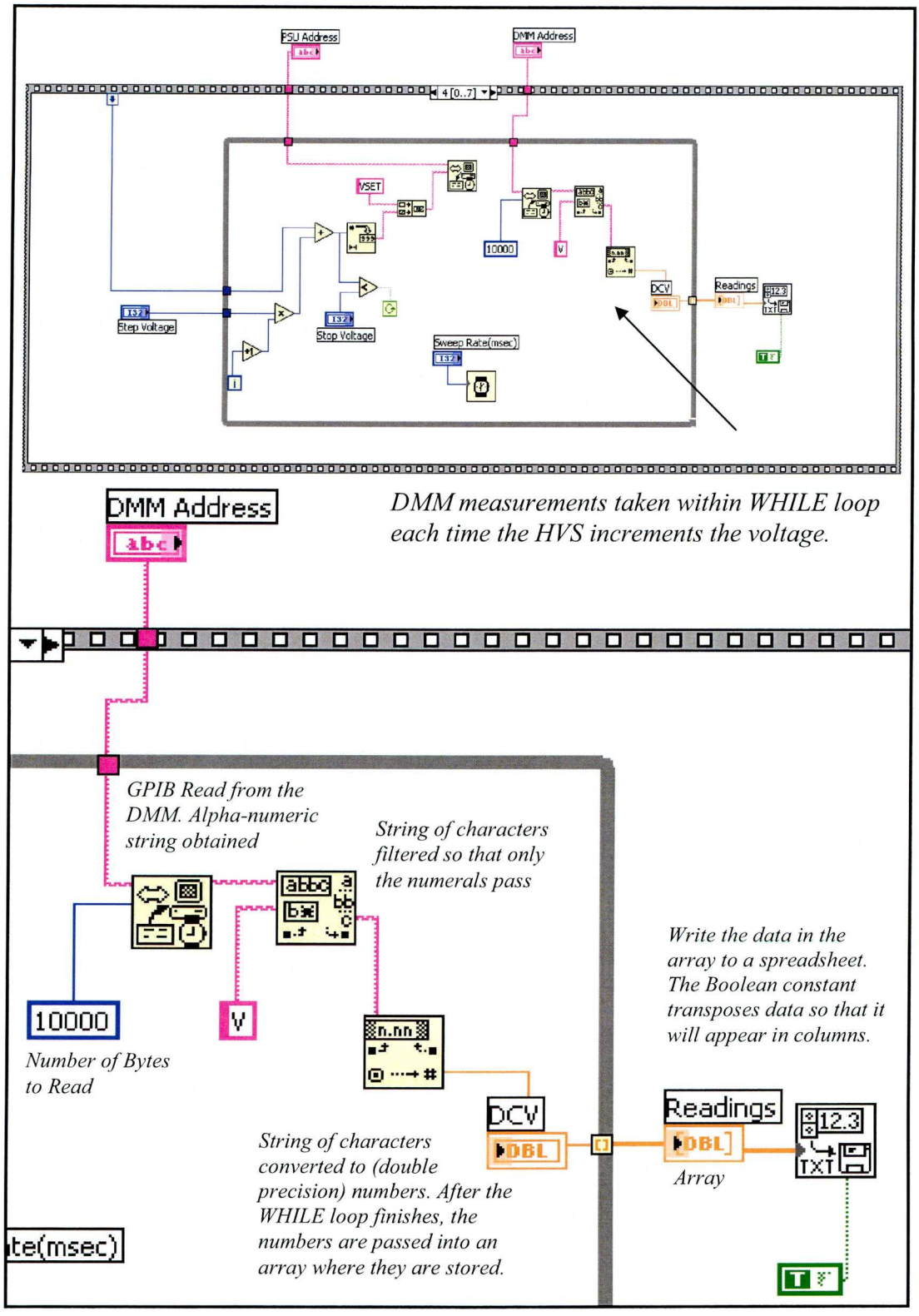

Figure 4.9: Block Diagram of LabVIEW model for controlling the high voltage source and digital multimeter.

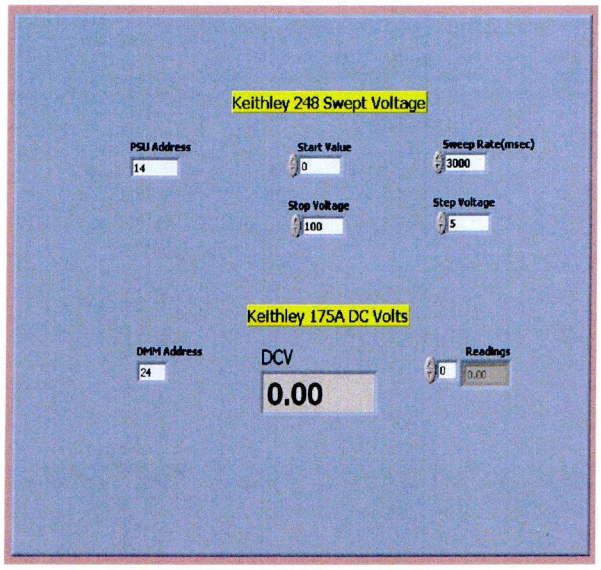

Figure 4.10: LabVIEW GUI for stepping the high voltage source

The results of the FE tests from the CNTs are shown in figures 4.11 to 4.17 below. The LabVIEW software was setup to increment the voltage by 5V every 10 seconds; the following data was obtained using these settings.

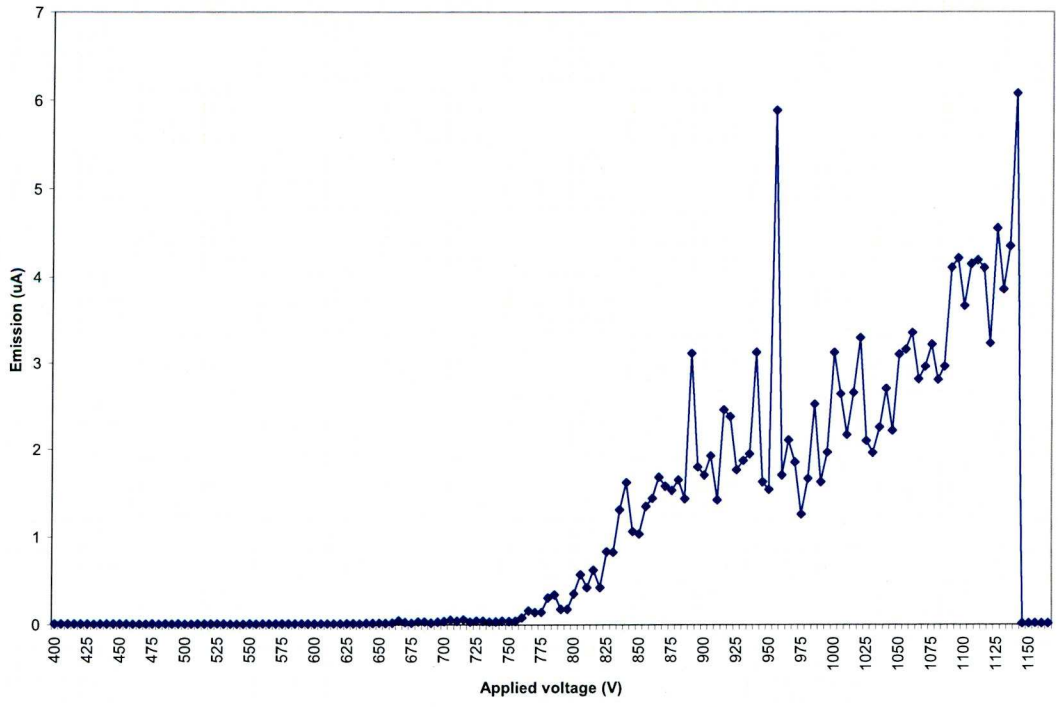

Figure 4.11: First run, applied voltage 400-1150V.

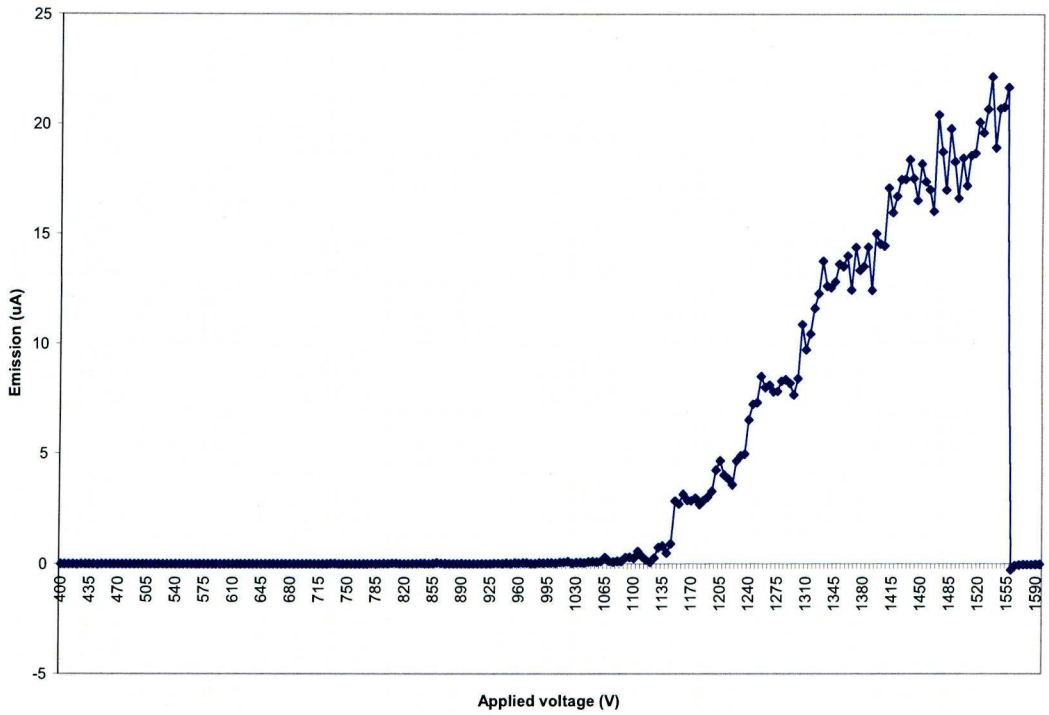

Figure 4.12: Second run, applied voltage 400-1555V.

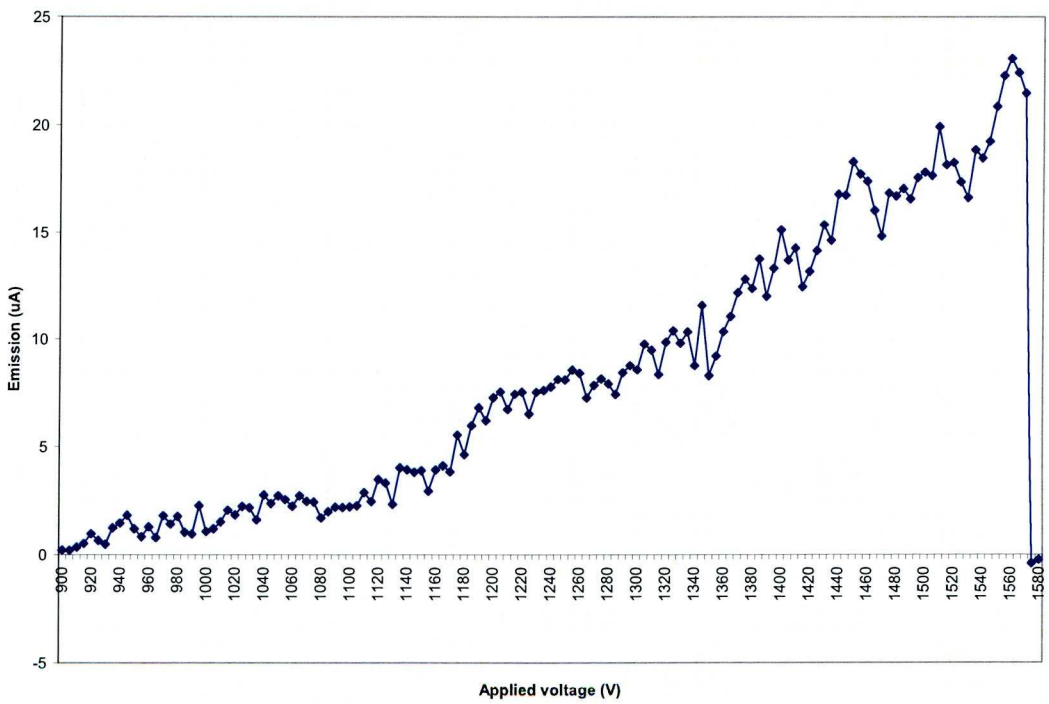

Figure 4.13: Third run, applied voltage 900-1660V

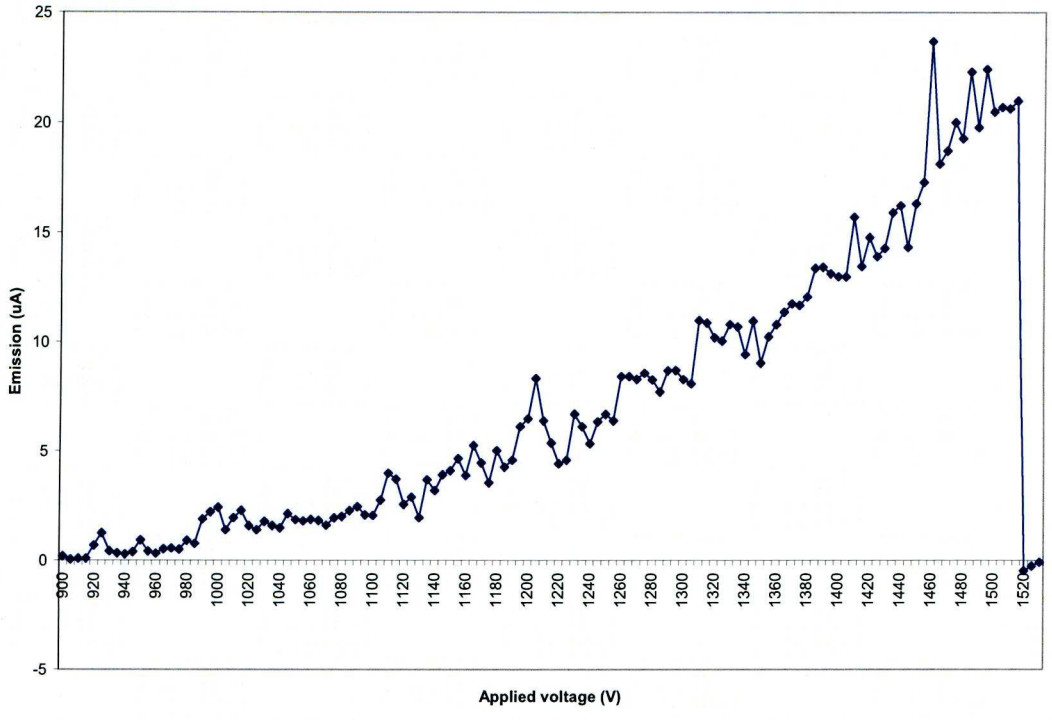

Figure 4.14: Fourth run, applied voltage 900-1520V

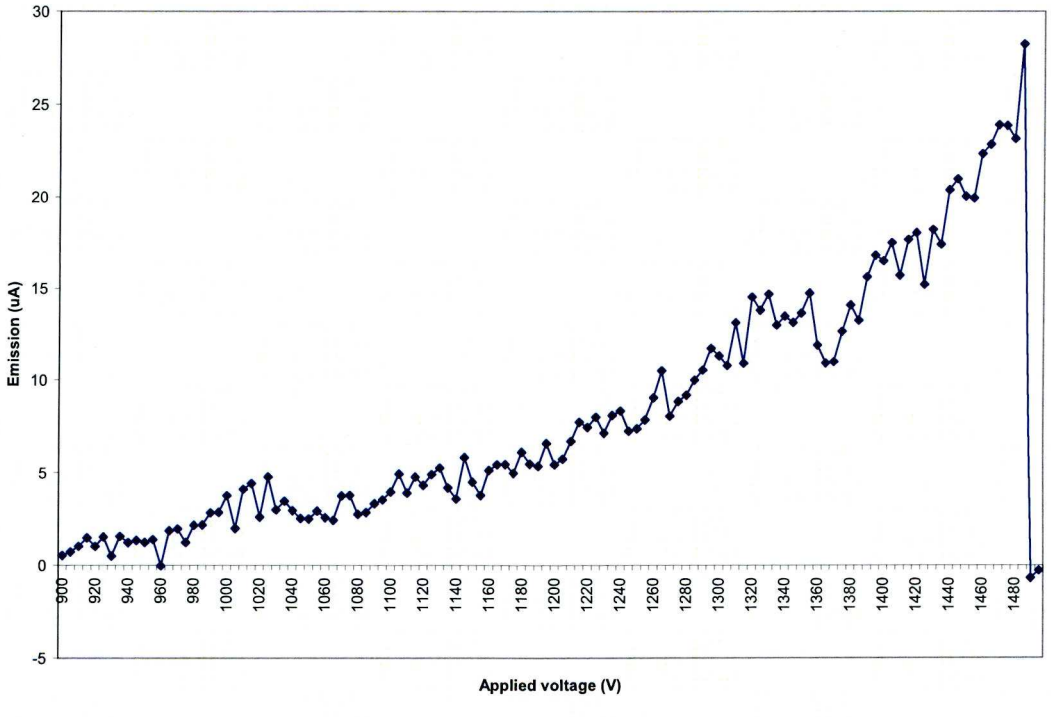

Figure 4.15: Fifth run, applied voltage 900-1480V

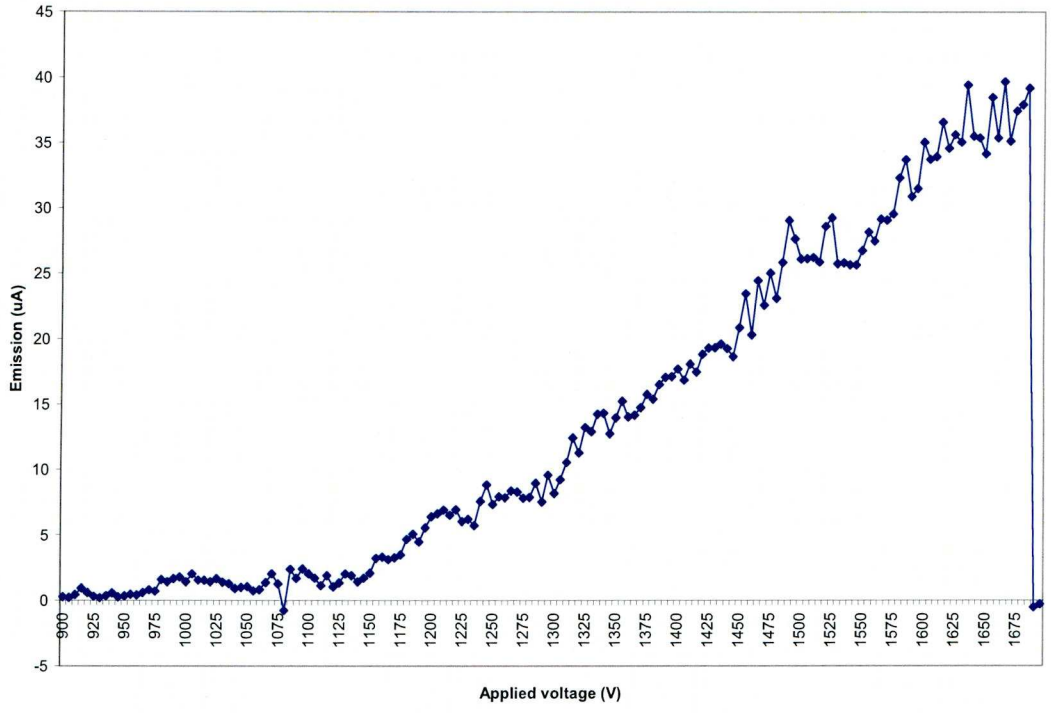

Figure 4.16: Sixth run, applied voltage 900-1675V

After the first few runs, the nanotubes were conditioned and the emission from them was much more linear over the tested voltage range. This can be seen in Figures 4.13-4.16. The peak emission current also increased from 6uA to around 40uA. This level of electron emission current is comparable to that obtained from a hot filament EI source at low emission (typically 10uA up to 100uA)

The results of the last test, shown in Figure 4.17, involved running the nanotubes with a constant voltage applied and monitoring their emission to see how stable they are over time and how they degrade.

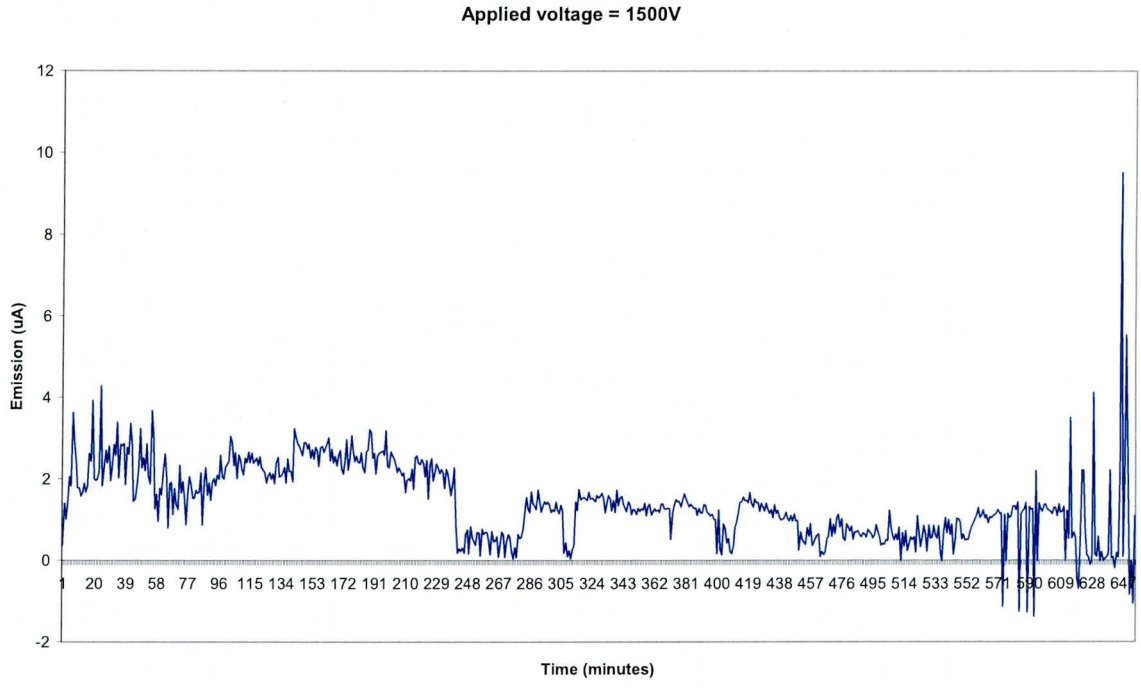

Figure 4.17: Results and stability test

As can be seen from Figure 4.17, there are a number of significant drops in emission. This implies that to be of any practical commercial use on long term basis, a feedback system would need to be used to monitor the emission of the nanotubes and adjust the applied voltage to compensate and stabilize the output.

4.4 Conclusions

Successful tests where carried out using a composite nanotube mixture which consisted of nanotubes and a polymer called Poly (3-Hexylthiophene). An emission current of 40uA was achieved which would be suitable for an ion source.

The nanotubes produced by the method described in this thesis are of variable dimensions (width and height) as shown in fig 4.4. Clearly the initiation of current flow from a nanotube 'forest' will occur from those nanotubes which are longer and closer to the anode, since in these cases the voltage required to produce the onset of field emission is lower. However as time progresses those nanotubes

first responsible for current flow will 'burn out' and emission from them will cease. A higher voltage is required to produce the same field from physically shorter nanotubes since the tips of these are further from the anode. There are however a greater number of these shorter nanotubes so the total current from the nanotube 'forest' is greater as time progresses. As with electron emission from sharp metallic tips the tip profile can degrade with time which results in a field reduction at the tip with consequent reduction in current. This effect (tip degradation) is more pronounced at higher pressures possibly due to reaction of the nanotube tips with excited chemical species in the vacuum ambient.

Due to the stability issues that were experienced, it is clear that further research and development work needs to be carried out before nanotubes could be used as a viable commercial alternative to other ionisation methods. In particular, further work needs to be done to investigate methods of extending the life of the nanotubes and to look at the most efficient method of producing and extracting ions created using the nanotube source. A possible approach would be use an existing electron impact ion source arrangement whereby the wire mesh cage would be enclosed by another cylinder having the interior coated with carbon nanotubes. In this arrangement the field applied between the cage (anode) and nanotube coated cylinder (cathode) will result in acceleration of electrons into the cage region and cause ion generation.

References

[1] Xinghui Li, Chongfeng Yang, Jinjun Feng, E*ffect of ageing process on performance of molybdenum field emission arrays*, Vacuum Electron Sources Conference, 2004. Proceedings. IVESC 2004

[2] S. Ijima, Nature **354**, *56 (1991)*

[3] *Donald S. Bethune, 2001,* "Carbon and metals: a path to single-wall carbon nanotubes", Physica B **323** (1-4), 90-96

[4] H. W. Kroto, J. R. Heath, S. C. O'Brien, R. F. Curl and R. E. Smalley (1985). *C^{60}: Buckminsterfullerene*. Nature **318***: 162–163.*

[5] L. Lou, P. Nordlander, R.E. Smalley, *Fullerene nanotubes in electric fields*, Vol **53**, Num 3

[6] Yahachi Saito, 1998, Ultramicroscopy, **73**, 1-6.

[7] L. Lou, P.Nordlander and R.E. Smalley, July 1995, Physical Review B Vol **52**, N° 3, pg 1429

[8] M.M.J. Treacy, T.W. Ebbesen, J.M. Gibson, Nature **381** (1996) 678.

[9] Kevin L. Jensen, *Electron emission theory and its application: Fowler–Nordheim equation and beyond*, J. Vac. Sci. Technol. B Volume 21, Issue 4, 1528-1544 (July 2003)

[10] I. Alexandroua, H. Wang, N. Sano, G. A. J. Amaratunga, Jan 2004, *"Structure of carbon onions and nanotubes formed by arc in liquids"*, Journal of Chemical Physics Volume 120, Number 2

[11] National Instruments, Nov. 2001, *'Getting Started with LabVIEW'*, part No. 321527E-01

Chapter 5
Application Studies using a portable QMS

5.1 Investigation using a portable QMS method for detecting Helicobacter pylori

Helicobacter pylori is a gram-negative, microaerophilic bacterium that inhabits various areas of the stomach and duodenum. It causes a chronic low-level inflammation of the stomach lining and is strongly linked to the development of duodenal and gastric ulcers and stomach cancer [1].

The diagnosis of infection is usually made by checking for dyspeptic symptoms and by tests which can indicate H. pylori infection. One can test noninvasively for H. pylori infection with a blood antibody test, stool antigen test, or with the carbon urea breath test (in which the patient drinks 14C- or 13C-labelled urea, which the bacterium metabolizes, producing labelled carbon dioxide that can be detected in the breath) [2]. However, the most reliable method for detecting H. pylori infection is a biopsy check during endoscopy with a rapid urease test, histological examination, and microbial culture. None of the test methods is completely failsafe. Even biopsy is dependent on the location of the biopsy. Blood antibody tests, for example, range from 76% to 84% sensitivity. Some drugs can affect H. pylori urease activity and give false negatives with the urea-based tests [3].

There are two different forms of urea and different instrumentation is required for each: carbon-14 is normally measured by scintillation and carbon-13 by isotope ratio mass spectrometry (IRMS) [4].

In the urease breath test, patients swallow urea labelled with an uncommon isotope, either radioactive carbon-14 or non-radioactive carbon-13. In the subsequent 10-30 minutes, the detection of isotope-labelled carbon dioxide in exhaled breath indicates that the urea was split. This indicates that urease (the enzyme that H. pylori uses to metabolize urea) is present in the stomach and hence that H. pylori bacteria are present [4]. Antibiotic treatments for removal of the H.Pylori bacteria are relatively simple and cheap once diagnosis is confirmed via the urease test.

5.1 Experimental

A portable QMS system with a triple filter, closed ion source and heated capillary inlet (MKS Cirrus [5]) was used to identify patients with Helicobacter pylori using the non-invasive carbon-13 Urea breath test. The following tests were conducted upon a number of patients at the Royal Liverpool University Hospital over a period of 4 months from August 2007. Samples of patient breath were collected in gas sample bags [6]. CEL Scientific Tedlar gas sampling bags are made of 2mm PVF (Tedlar) film as shown in Figure 5.1(a):

a)

b)

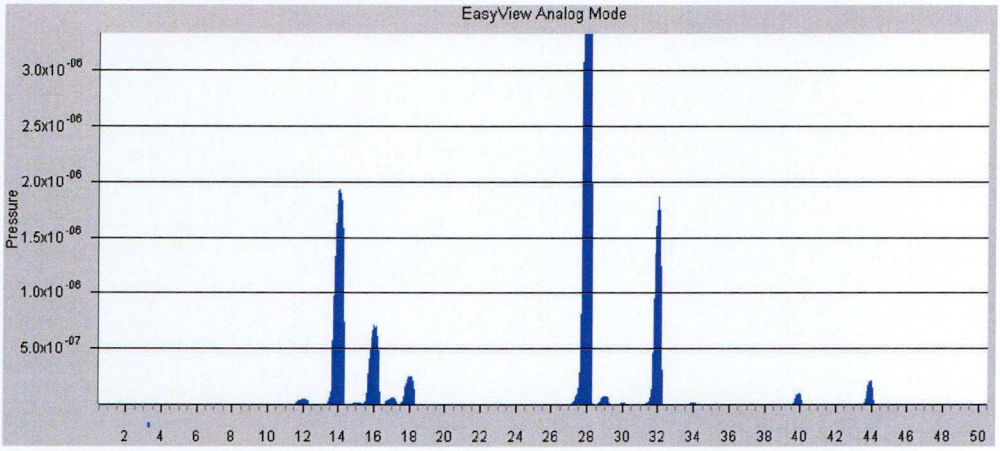

Figure 5.1 Tedlar gas sampling bag used for QMS urease breath testing(a, upper) and QMS output of analysis taken from patient breath samples using the MKS Cirrus portable QMS system (linear scale)(b,lower).

Tedlar is tough, durable, and considered chemically inert to a wide range of compounds. Tedlar bags are used for indoor air sampling, breath sampling, hazardous waste sites, leaking underground storage tanks, stack sampling, soil gas sampling, gas blending, calibration test standards and most other gas sampling needs. Samples of patient breath can conveniently be taken in 0.5 litre bags fitted with a polypropylene inlet. Gas from the bags was sampled by inserting the QMS capillary.

Figure 5.1(b) above shows a mass spectrum of exhaled patient breath taken from one of the sample bags. The main area of interest is in the mass range from 40 to 45. Peaks at m/z =44 and m/z= 45 correspond to exhaled carbon dioxide with carbon 12 and 13 isotopes present respectively. On this linear graph, the

concentration of mass 45 is too low compared to the other spectra to be seen, however, by using a log plot as shown in Figure 5.2, a peak at m/z = 45 can be seen.

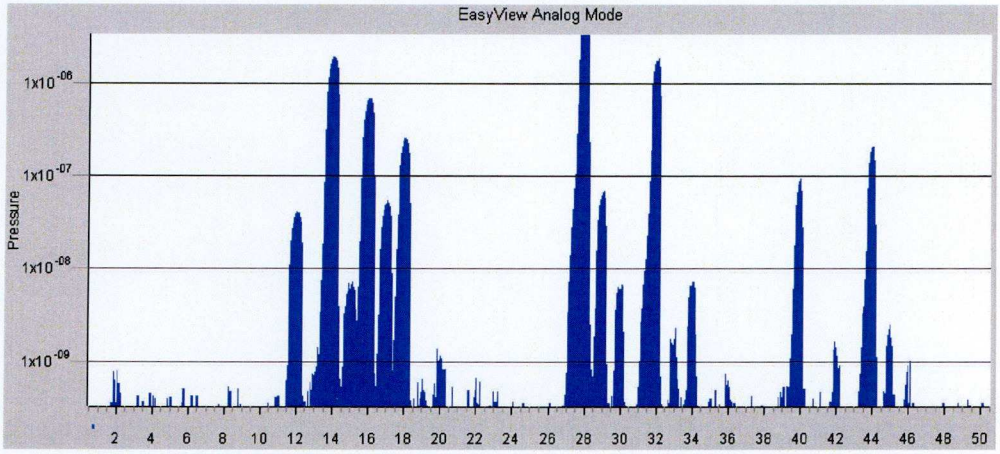

Figure 5.2: QMS spectral peaks at m/z 44 and 45 corresponding to $^{12}CO_2$ and $^{13}CO_2$, log scale.

5.1.1 Sampling procedure followed (at RLUH hospital)

(i) Patient provides a baseline breath sample (pre-bag).

(ii) Patient given a urea tablet.

(iii) After 30 minutes the patient gives a second breath sample (post-bag).

5.1.2 Sampling procedure in the QMS laboratory

The breath samples were received from the hospital at random intervals (usually a few days), depending on when they where able to collect the samples from patents. Using the MKS Cirrus QMS system, the following procedure was used to obtain the mass spectrum that is later analysed:

(i) First the baseline sample bag (pre-Urea tablet) was connected to the capillary inlet of the mass spectrometer. Once connected the bag valve was opened and 10 seconds allowed to elapse before recording the sample data, this ensures the sample has passed through the capillary inlet and has reached the mass spectrometer.

(ii) The mass spectrometer was configured to take six consecutive scans of the sample bag. These six scans were combined and averaged, this was to reduce the effect of any minor variations in the peak height that occur while scanning samples.

(iii) Once the data has been recorded the value on the sample bag is closed and the bag removed from the capillary inlet.

(iv) Steps 1-3 are then repeated for the post bag.

(v) The next step is to use a MATLAB script [7] to compare the pre and post data and calculate the percentage change between mass 44 and 45 for the pre and post bags and therefore determine if a patient has Helicobacter pylori. The MATLAB source code is shown in Appendix 5.1

5.1.3 Explanation of MATLAB script

(i) Determine the maximum spectral height of m/z = 44 and m/z = 45 for a single pre-bag sampled 6 times.

(ii) Calculate the ratio mass 44 / mass 45.

(iii) Determine the mean value of the m(44)/m(45) pre-bag ratios.

(iv) Repeat steps 1,2 and 3 for the post-bag ratio results.

(v) Compare pre and post ratios to give diagnosis:

If [Post-ratio/Pre-Ratio]> 0.03 then a positive diagnosis is assumed (H-Pylori present)

If [Post-ratio/Pre-Ratio] < 0.03 then a negative diagnosis is assumed (H-Pylori absent)

Figures 5.3 and 5.4 below show a single scan from the pre and post bags for Patient 4.

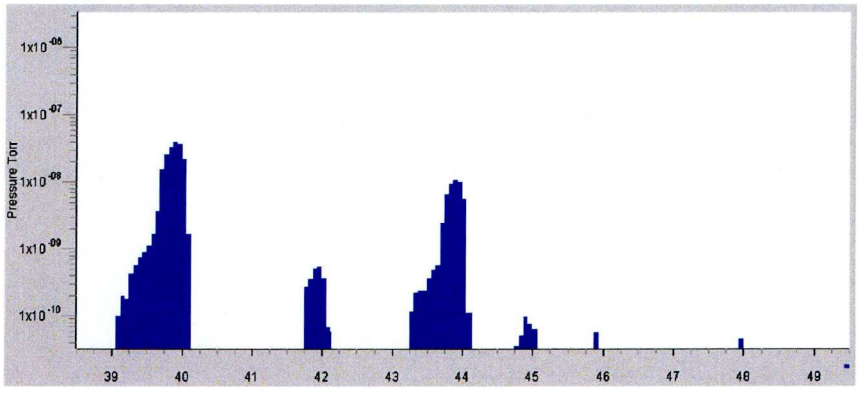

Figure 5.3: Patient 4- pre bag sample (before taking Urea tablet).

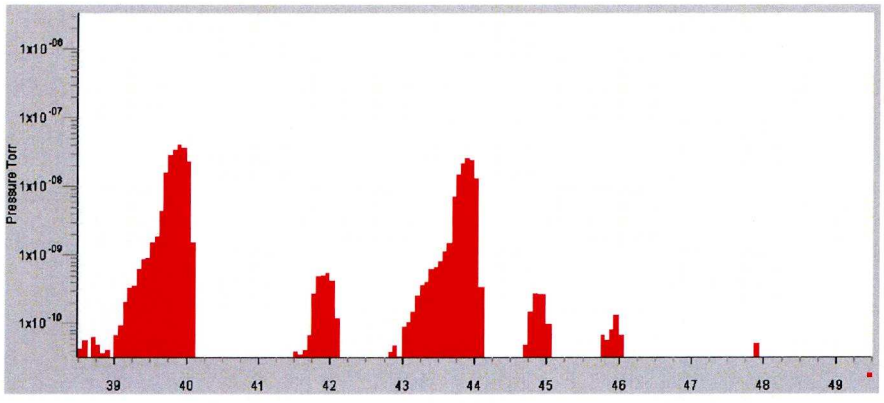

Figure 5.4: Patient 4 - post bag sample (30 minutes after taking Urea tablet)

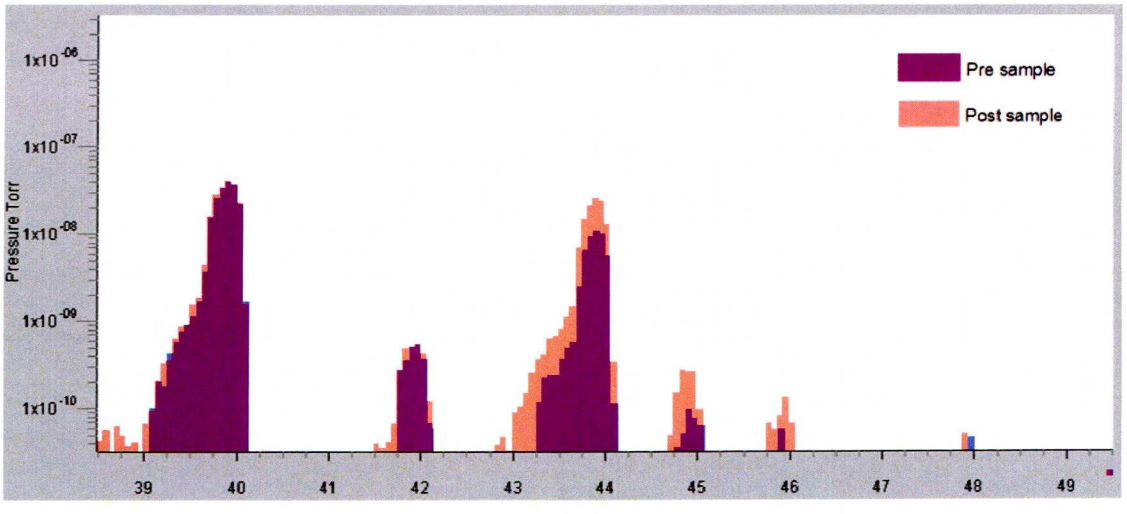

Figure 5.5: Superimposed spectra of pre and post sample bags for patient 4.

Figure 5.5 shows the pre and post breath samples superimposed. In this case, there is a 3.3% increase in the ratio of the peak heights for the m/z =44 and m/z =45 i.e. (m/z=44/ m/z=45 > 0.03) after taking the urea tablet, therefore, by the criteria given in 5.1.3, a positive diagnosis (presence of H pylori in the stomach) is assumed. The patient has the symptoms of a duodenal and/or gastric ulcer.

Figures 5.6 and 5.7 below show a single scan from the pre and post bags for another patient (Patient 5).

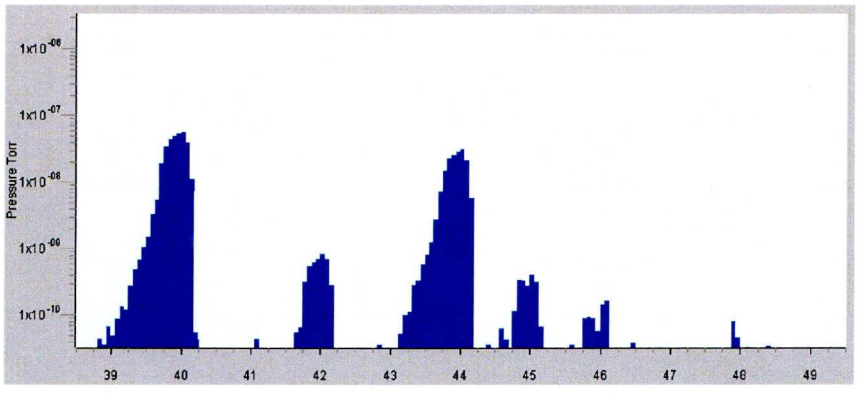

Figure 5.6: Patient 5 pre sample before taking Urea tablet.

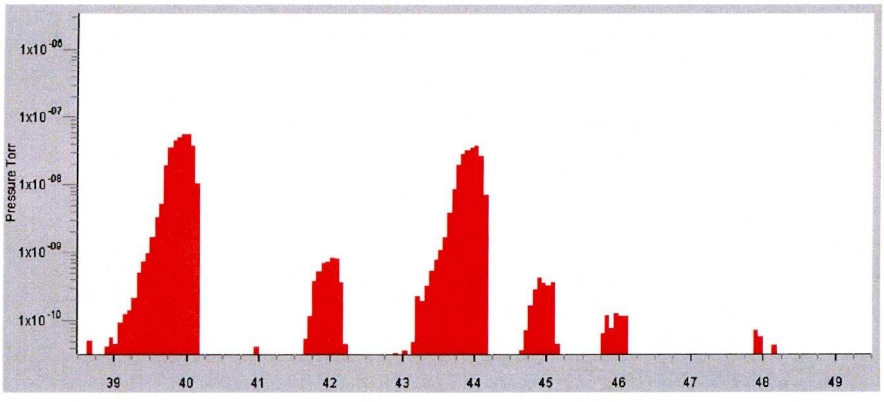

Figure 5.7: Patient 5 post sample, 30 minutes after taking Urea tablet.

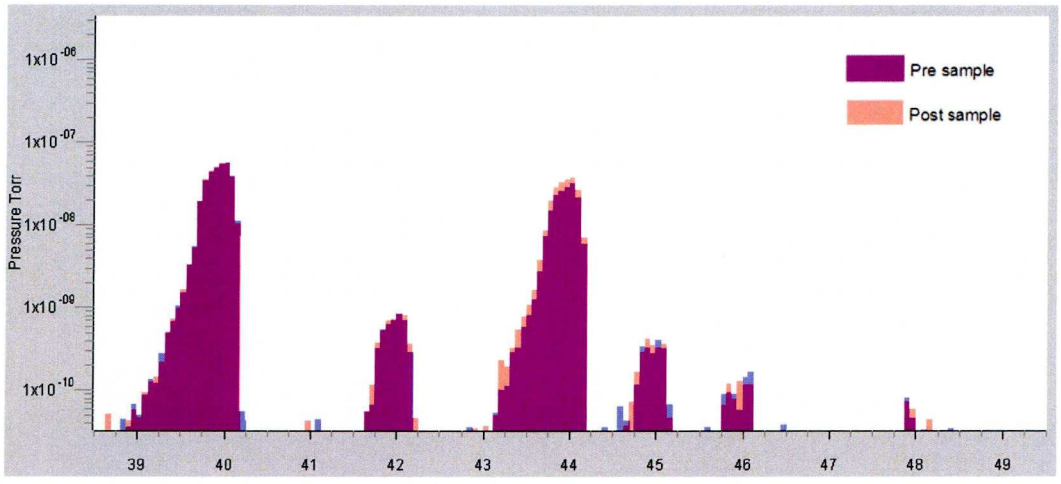

Figure 5.8: Superimposed spectra of pre and post sample bags for patient 5.

Figure 5.8 shows the pre and post samples superimposed. In this case, there is a 1.5% increase for the mass 44/45 ratio after taking the urea tablet, therefore, by the criteria of 5.1.3 above, a negative diagnosis is assumed. The patient is not showing symptoms of a gastric or duodenal ulcer. A full set of results for the patient trials can be seen in Table 1 compared with the results obtained using the conventional H-Pylori breath test method (Table 1, final column 'termed hospital' result). In the conventional method (hospital result) samples of patient breath are sent in test tubes off-site through the post to a central laboratory elsewhere in the UK for analysis on a large magnetic sector mass spectrometer. Results are made available to the clinicians between 2 and 3 weeks after the tests on the patient. If positive, this normally necessitates another visit to the hospital by the patient. In the case of the results listed in Table 1, these bags were tested in the laboratory as soon as they were obtained from the hospital.

Patient	Date tested - First Run	Percentage change	Our Result	Hospital result
1	1st August 2007	2.3805	negative	negative
2	1st August	2.6119	negative	negative
3	4th August	-0.27153	negative	negative
4	4th August	3.3088	positive	positive
5	4th August	1.5157	negative	negative
6	14th August	-0.41268	negative	negative
7	14th August	3.2864	positive	negative
8	14th August	-0.6307	negative	negative
9	14th August	5.0282	positive	negative
10	23rd August	-7.4317	negative	negative
11	23rd August	-1.3585	negative	negative
12	23rd August	-1.392	negative	negative
13	23rd August	1.7658	negative	negative
14	14th August	-1.4281	negative	negative
15	28th November	0.90435	negative	negative
16	28th November	0.057905	negative	positive
17	28th November	-6.1336	negative	negative
18	28th November	1.2009	negative	negative

Table 1: Results obtained on the same date as the breath sample bags were received from the RLUH.

In principle, with a QMS instrument present in the patient clinic at the RLUH, the QMS tests could be carried out on the same day with a consequent saving in time between test and diagnosis. The table shows that out of 18 patient cases considered, 15 agree with hospital results with 2 false positives and 1 false negative. False positive diagnosis may be due to a greater sensitivity obtained using the QMS method compared to the conventional method.

Patient	Date tested - Second Run	Percentage change	Our Result	Hospital result
1	30th of November	0.1687	negative	negative
2	30th of November	-6.2098	negative	negative
3	30th of November	10.191	positive	negative
4	30th of November	9.4424	positive	positive
5	30th of November	-0.0367	negative	negative
6	30th of November	-3.1568	negative	negative
7	30th of November	-0.95781	negative	negative
8	30th of November	-4.9903	negative	negative
9	30th of November	-10.592	negative	negative
10	30th of November	-32.116	negative	negative
11	30th of November	-2.3588	negative	negative
12	30th of November	0.008042	negative	negative
13	30th of November	7.0914	positive	negative
14	30th of November	0.09228	negative	negative
15	30th of November	2.4801	negative	negative
16	30th of November	7.0488	positive	positive
17	30th of November	2.3903	negative	negative
18	30th of November	2.0653	negative	negative

Table 2: Results of retesting all the sample bags at the end of the initial trial period.

The results obtained during the second test run produced slightly different results with 16 out the 18 cases agree with the hospital with 2 false positives. This indicates that the methodology employed is robust and that the breath samples remain largely stable with time, though not in every single case.

5.2 Conclusions

The results of these experiments show that it is possible to use a portable QMS system in the field of residual gas analysis to detect the presence of H-Pylori via the urease breath test. The definite prospect thus emerges of patient testing 'on the spot' with positively diagnosed patients able to take their antibiotic treatment home with them on the same day as their urease breath test. This allows consequent saving in clinician time (no need for a second patient visit) and often less chance of sample confusion that sometimes occurs when samples are sent through the post for centralised analysis elsewhere.

Specificity (Sp) for a diagnostic test may be defined as:

$$Sp = \frac{\text{number of True Negatives}}{\text{number of True Negatives + number of False Positives}}$$

The usual method of implementing the Urease breath test is by sending samples away for MS analysis using isotope ratio mass spectrometry (IRMS) [8] which commonly uses magnetic sector instrumentation. The reported specificity of the conventional (IRMS) breath test is 93% [9]. The specificity of the QMS based urease breath test from the results in table 1 was 87.5 which compares well with that reported [9]. The number patients testing positive for HBP was low since in this batch of trials the patients had already undergone treatment. Therefore it was not possible to obtain reliable estimates of sensitivity since the sample size was too low.

The Negative Predictive Value (NPV) of a diagnostic test is the proportion of patients with negative test results who are correctly diagnosed and is defined as:

$$NPV = \frac{\text{number of True Negatives}}{\text{number of True Negatives + number of False Negatives}}$$

The negative predictive value using the QMS was 93.3 which is high. Positive predictive values could not be obtained for the reasons given previously.

The QMS version of the urease test described in this chapter does however necessitate the use of an accurate QMS system (e.g. triple filter QMS) with resolution and sensitivity greater than that usually obtained with microengineered versions. Using the QMS method, the diagnosis was found to agree with that obtained by the usual hospital method for 83.3% of the time. These results indicate QMS could be a viable alternative for the detections of Helicobacter pylori. However, a wider study with more patient trials is needed to verify these initial results.

References

[1] Sutton, F. M, '*Diagnosis of H. pylori Infection'*, Infectious Medicine 15, no. 5, pp.331-336. (1998)

[2] Suganuma M, Yamaguchi K, Ono Y, et al, *'TNF-alpha-inducing protein, a carcinogenic factor secreted from H. pylori, enters gastric cancer cells.'* Int. J. Cancer **123** 1, pp.117–22 (2008).

[3] Stenström B, Mendis A, Marshall B, '*Helicobacter pylori - The latest in diagnosis and treatment.* Aust Fam Physician, **37** 8, pp.608–12 (2008)

[4] C.-C. Liao, C.-L. Lee, '*The 13C-urea breath test to detect Helicobacter pylori infection: a validated simple methodology with 50 mg 13C-urea*, Aliment Pharmacol Ther. ,16, pp.787–792, (2002)

[5] MKS Cirrus, Data sheets available from: http://www.mksinst.com/docs/UR/CirrusDS.pdf

[6] http://www.celscientific.com/index.html

[7] Private communication with Dr P.G. Turner (AWE, Aldermaston)

[8] F.Stellaard and H.Elzinga, '*Analytical techniques in biomedical stable isotope applications: (isotope ratio) mass spectrometry or infrared spectrometry?'*, Isotopes in Environmental and Health Studies, **41**, Issue 4, pp.345 – 36, (Dec. 2005) ,

[9] Surveyor I, Goodwin CS, Mullan BP, '*The 14C-urea breath-test for the detection of gastric Campylobacter pylori infection'*, Med. J Australia. pp.435-9 (Oct. 1989)

Chapter 6
Conclusions and suggestions for further work

The development of mass spectrometers has advanced rapidly in the last decade of years with a focus on building instruments that can be made portable whilst maintaining good performance. To achieve this, miniaturisation of mass spectrometer component parts has been pursued, especially in the case of mass analysers. The reduction in size of analysers offers several advantages:

1. Lower manufacturing costs because the implementation technologies that are being used offer mass production not only for separate components, but also for complete devices.
2. Operation at higher pressures due to shorter length of the ion mean free path.
3. Usage of less robust and less expensive vacuum systems due to smaller device size and higher pressure operation.
4. Lower power consumption with possibility to operate with low power battery since lower electrode voltages are needed to generate the required electric fields.
5. Potential for the whole mass spectrometry system being portable and/or mounted on autonomous vehicles (e.g. for underwater MS).

The above advantages will further increase the number of mass spectrometry applications, particularly for 'in the field' RGA applications such as instant medical diagnosis, water and environmental analysis and detection of oil, natural gas, and explosives.

Miniaturization of mass spectrometers is often done by using microelectromechanical systems (MEMS) technology, which is mainly based on semiconductor processing technologies and with metal and dielectric deposition. However it is difficult to produce the ideal hyperbolic form QMS electrodes using these methods. Two novel types of hyperbolic form QMF have been described: (i) a metal hyperbolic mass filter fabricated using EDM and (ii) a DLP produced mass filter. Both QMFs are suitable for use in portable QMS systems. QMS instruments made with both types have been realised and tested. The EDM formed QMF performed well and a number of tests were carried out using different ion energies (3eV, 5eV, and 7eV) and different voltages applied to the extract and focus plates to achieve the optimal resolution, -25V for the extract and -20V for the focus was found to provide optimal results.

An alternative novel approach for QMS miniaturisation was proposed using rapid prototyping techniques. DLP has also been used to fabricate hyperbolic form electrodes in PMMA for both a QMF and the housing. The QMF electrodes were coated with gold by thermal evaporation to provide low electrical conductivity and yet maintain nanoscale surface roughness. Mass spectra have been obtained using this approach and show good agreement with theoretically simulated mass spectra predicted by our model (QMS2-H).

Two commercially obtained software suites, SIMION and CPO were compared to determine which one would be suitable for the simulation of RGA QMS ion sources. Both packages performed well and produced similar results but SIMION was both easier to use and faster providing simulated ion trajectories in minutes rather than hours. The results subsequently obtained using SIMION for the 4 plate ion source show that greater control over the beam collimation and as a result improved the extraction efficiency.

Successful tests were carried out using a composite nanotube mixture, which consisted of nanotubes and a polymer called Poly (3-Hexylthiophene). Electron emission currents up to 40uA were achieved, which render this material suitable for use as a cold cathode ion source. Future work that would need to be carried out before nanotubes would be a viable alternative is to investigate the stability issues that were experienced and also to look at methods of extending the life of the nanotubes. Further work needs to be done to investigate the most efficient method of producing and extracting ions created using the nanotube arrangement.

Successful patient trials were carried out using a portable QMS system to detect the presence of H-Pylori via the urease breath test. A novel methodology for H-Pylori detection was implemented. The tests were conducted on a number of patients at the Royal Liverpool University Hospital over a period of 4-month period. The results obtained using the QMS agreed with the hospital results 83.3% of the time, indicating that this approach using a portable QMS could be a viable alternative to the conventional method of using a centralised testing facility. More tests are required with larger patient sample to determine specificity and accuracy of diagnosis and this is recommended as an avenue for future research. A commercially available QMS was used for the patient trials since the sensitivity of the DLP and EDM QMS systems were not adequate. However with future improvements to these systems (e.g. by the use of a prefilter and /or higher frequency RF excitation, and/or better detection), it would be possible to increase the performance of these novel miniature hyperbolic QMS instruments and thus deploy them for H-pylori detection and/or other medical applications.

List of Publications

1. B.Brkic, S.Taylor, J.F.Ralph and N.France,
   High Fidelity simulations of ion trajectories in miniature ion traps using the boundary element method, Phys Rev A, **73** (1), 012326 (2006) and selected for publication in Virtual Journal of Quantum Information, **6** (2), (Feb 2006).

2. N.France, T.Hogan, B.Brkić, R.Hathaway, S.Shannon and S.Taylor,
   Ion source for a miniature RGA: results and simulation for Zone 1 and Zone 3 operation, presented at the IOP 7th RGA Users Group meeting, Warrington (2006).

3. T.J.Hogan, N.France, J.R.Gibson and S.Taylor,
   A design and simulation tool for miniature mass spectrometers, presented at 6th Workshop on Harsh Environment Mass Spectrometry HEMS Workshop, Cocoa Beach, (2007).

4. B.Brkic. N.France, T.J.Hogan and S.Taylor,
   3d Modeling of miniature ion sources for RGA, presented at the IOP 8th RGA Users Group meeting, Culham (2008).

5. B.Brkic. N.France, T.J.Hogan and S.Taylor,
   Advanced modelling of a miniature QMS, presented at the 56th ASMS Conference on Mass Spectrometry, Denver (June, 2008).

6. B.Brkić, N.France, S.Taylor, A.T. Clare, C.J. Sutcliffe and P.R. Chalker
   Towards portable mass spectrometry: design, simulations, fabrication and testing of a miniature quadrupole mass spectrometer, presented at the British Mass Spectrometry Society (BMSS) Conference, York (Sept 2008)

7. J. Sreekumar, B.Brkić, N.France, T.J.Hogan, J.R.Gibson and S.Taylor,
   Simulation of a QMS with an electron impact ion source including pressure dependence, presented at the British Mass Spectrometry Society (BMSS) Conference, York (2008).

8. B.Brkić, N.France, A. T. Clare, CJ. Sutcliffe, P.R. Chalker, and S. Taylor
   Development of Quadrupole Mass Spectrometers using Rapid Prototyping, submitted to J. American Society of Mass Spectrometry (2008).

9. B.Brkić, N.France, and S. Taylor, *Performance simulations of a mass spectrometer ion source using the boundary element method*, in preparation for submission to Review of Scientific Instruments (2008).

Appendices

Appendix 2.1 – MATLAB source code used to determine Ion secular frequencies

```
clear
filename = 'ENDCAPTRAP.txt'

%=============
% Extract data
%=============
XYZTData=load(filename);

datapoints = size(XYZTData,1);

x=XYZTData(1:datapoints,1);
y=XYZTData(1:datapoints,2);
z=XYZTData(1:datapoints,3);
t=XYZTData(1:datapoints,4)*1e-3; % to convert from miliseconds to seconds
%=============

%=============
% Process Data
%=============

% FREQUENCY AXIS
%---------------
half_datapoints = floor(datapoints/2)
sampling_time = abs( mean( t(1:datapoints-1) - t(2:datapoints) ) );

sampling_freq = 1/sampling_time;
```

```
f = sampling_freq * (0:half_datapoints-1)/datapoints;

% FFT
%----
fft_x = fft(x,datapoints);
fft_y = fft(y,datapoints);
%fft_r = fft(r,datapoints);
fft_z = fft(z,datapoints);

% POWER
%------
Pfft_x = fft_x.* conj(fft_x) / datapoints;
Pfft_y = fft_y.* conj(fft_y) / datapoints;
%Pfft_r = fft_r.* conj(fft_r) / datapoints;
Pfft_z = fft_z.* conj(fft_z) / datapoints;
%============

%============
% Draw graphs
%============

%--------------
% X - Frequency plot
figure
subplot(2,1,1)
plot(f/(1e+6),20*log10(Pfft_x(1:half_datapoints)))
%axis([0 20 -180 70])
%title('"Power" spectrum of X,Y position')
xlabel('Radial (X,Y) frequencies (MHz)')
ylabel('Power spectrum')
%-------------
```

```
% Y - Frequency plot
%figure
%subplot(2,1,2)
%plot(f/(1e+6),20*log10(Pfft_y(1:half_datapoints)))
%axis([0 10 -175 75])
%title('"Power" spectrum of X,Y position')
%xlabel('Radial (X,Y) frequencies (MHz)')
%ylabel('Power spectrum')
%-------------

% Z - Frequency plot
subplot(2,1,2)
plot(f/(1e+6),20*log10(Pfft_z(1:half_datapoints)))
%axis([0 40 -190 70])
%title('"Power" spectrum of Z position')
xlabel('Axial (Z) frequencies (MHz)')
ylabel('Power spectrum')
%-------------
```

Appendix 2.2

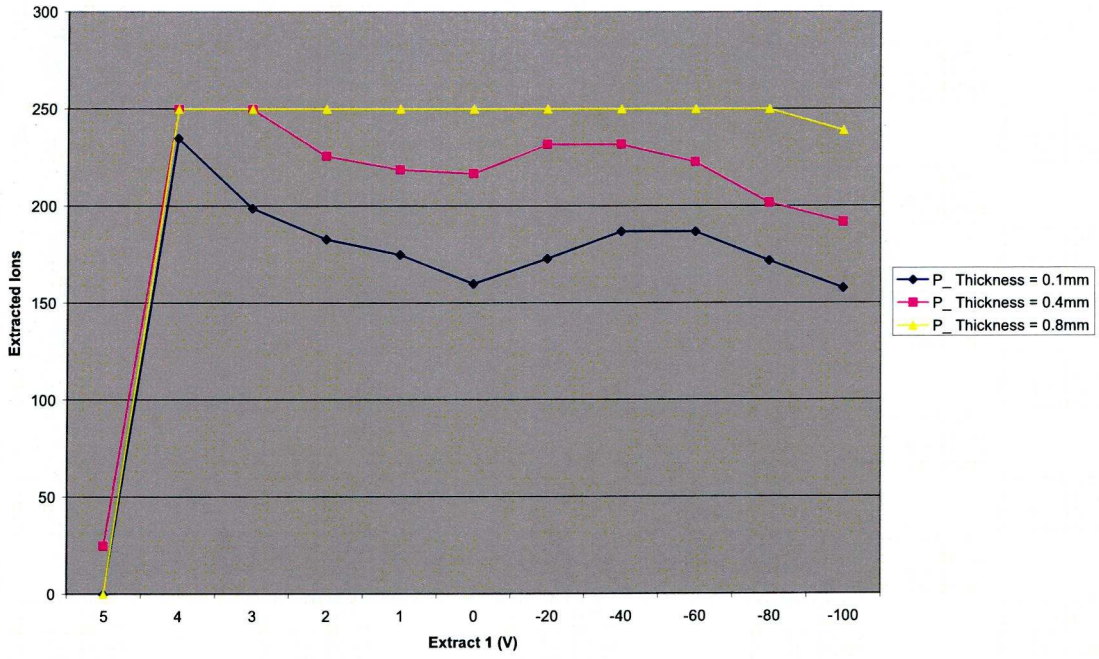

Variation of plate thickness versus Extract1. Extract2 fixed at 0V.

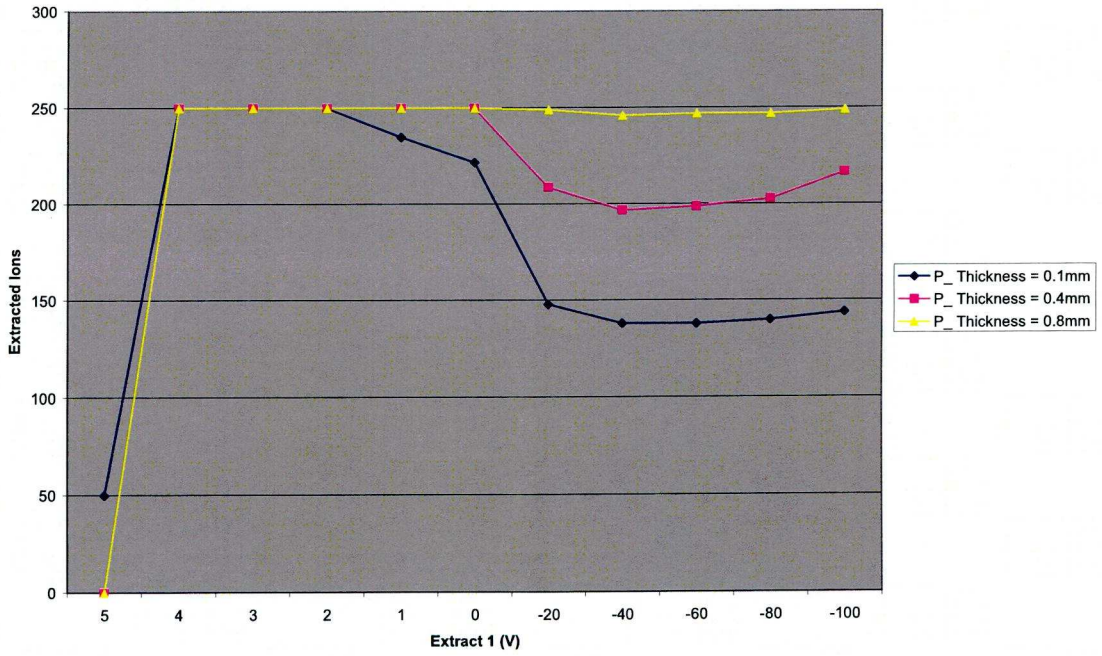

Variation of plate thickness versus Extract1. Extract2 fixed at -20V.

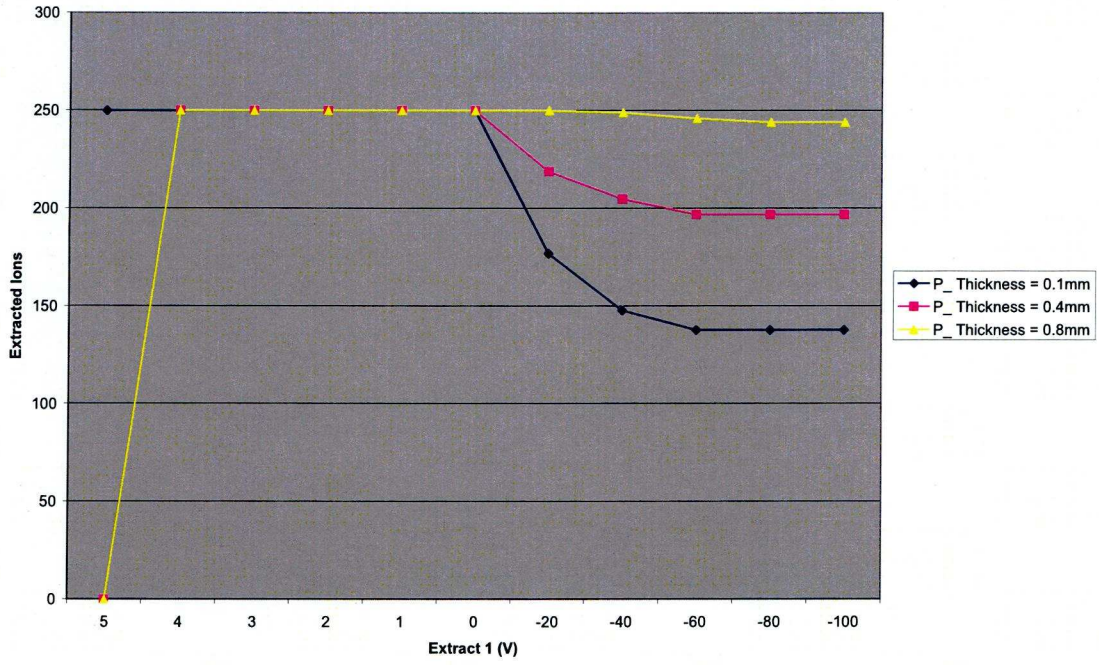

Variation of plate thickness versus Extract1. Extract2 fixed at -40V.

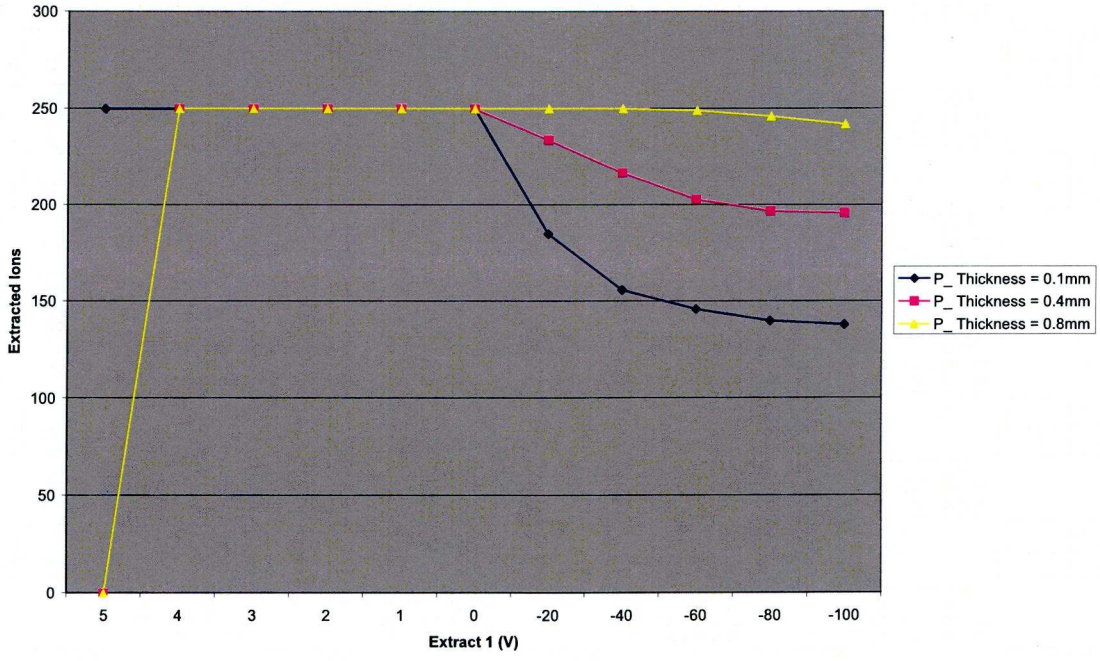

Variation of plate thickness versus Extract1. Extract2 fixed at -60V.

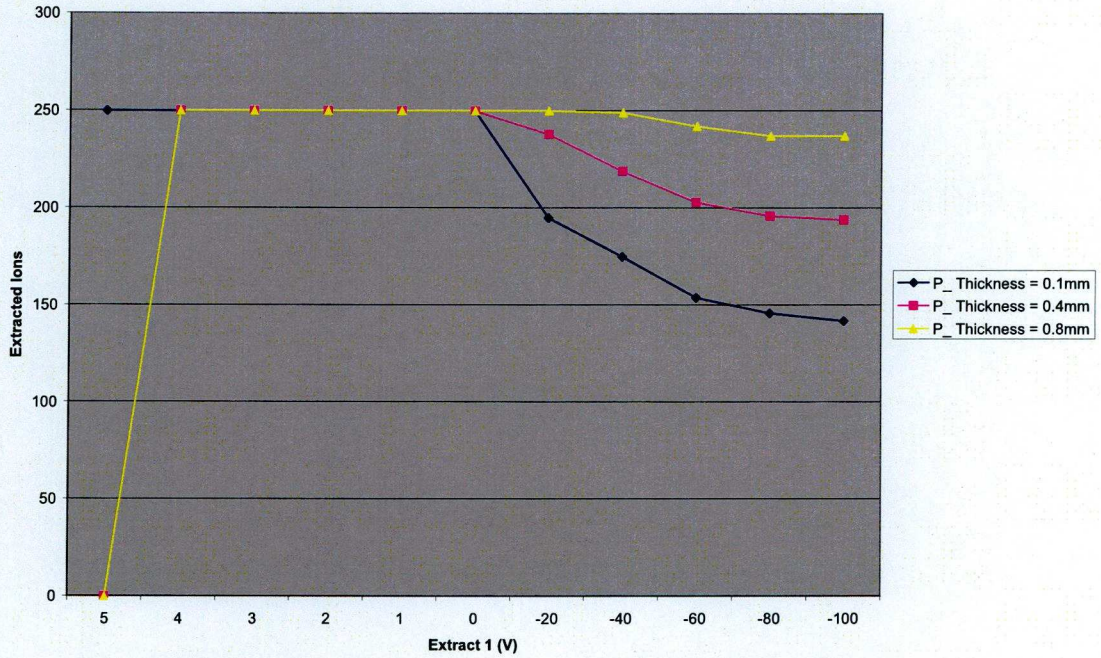

Variation of plate thickness versus Extract1. Extract2 fixed at -80V.

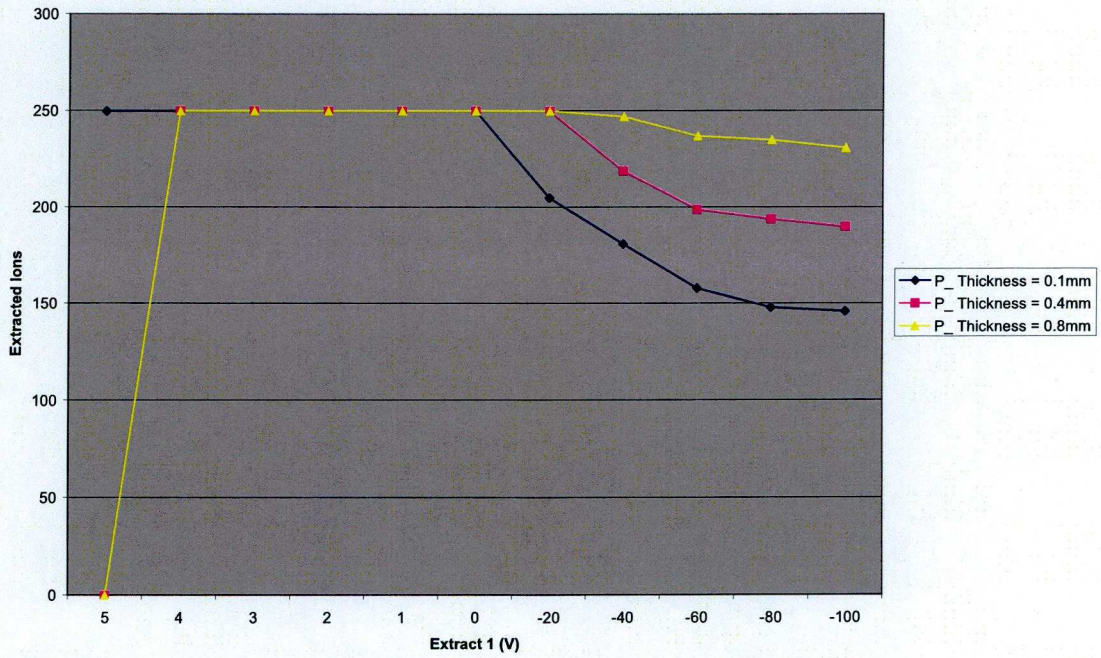

Variation of plate thickness versus Extract1. Extract2 fixed at -100V.

Appendix 2.3

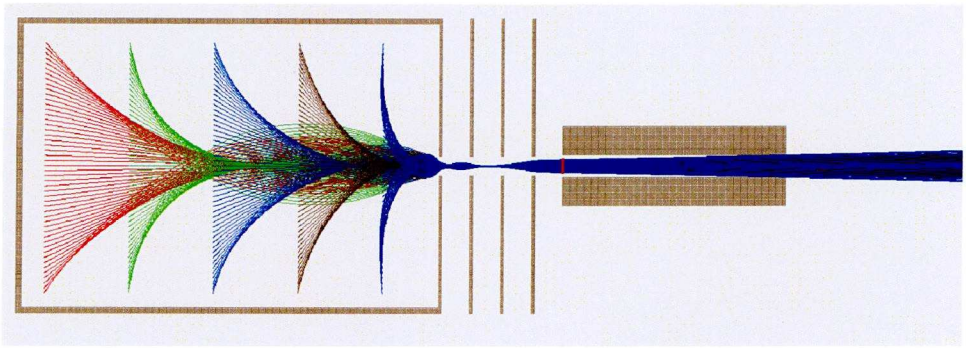

Figure 1: SIMION output showing ion trajectories (rays) and beam profile for Index Number 1 of Table 2.2 (Cage = 0.1mm, Extract1 = 0.1mm, Extract2 = 0.1mm, Earth = 0.1mm) with potentials: Cage = +5V Extract 1 = +4V Extract 2 = -40V

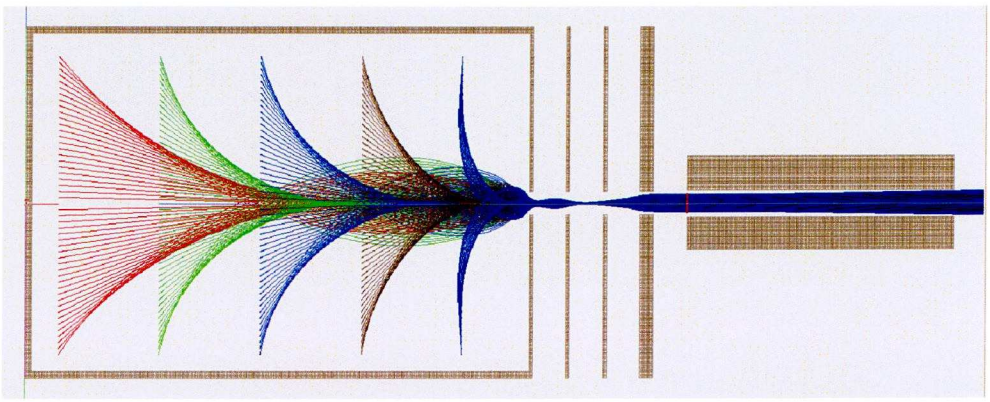

Figure 2: SIMION output showing ion trajectories (rays) and beam profile for Index Number 2 of Table 2.2 (Cage = 0.1mm, Extract1 = 0.1mm, Extract2 = 0.1mm, Earth = 0.4mm) with potentials: Cage = +5V Extract 1 = +4V Extract 2 = -40V

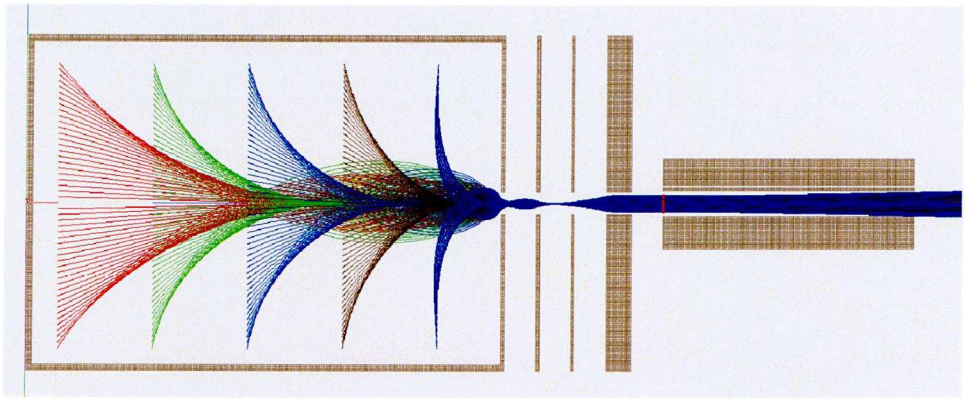

Figure 3: SIMION output showing ion trajectories (rays) and beam profile for Index Number 3 of Table 2.2 (Cage = 0.1mm, Extract1 = 0.1mm, Extract2 = 0.1mm, Earth = 0.8mm) with potentials: Cage = +5V Extract 1 = +4V Extract 2 = -40V

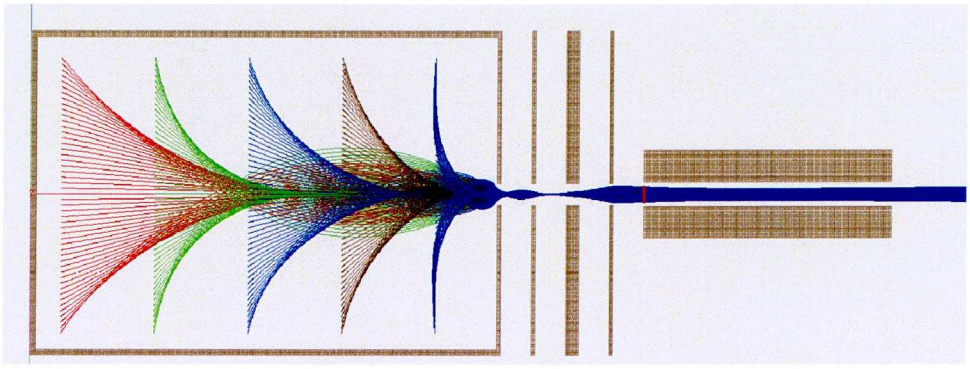

Figure 4: SIMION output showing ion trajectories (rays) and beam profile for Index Number 4 of Table 2.2 (Cage = 0.1mm, Extract1 = 0.1mm, Extract2 = 0.4mm, Earth = 0.1mm) with potentials: Cage = +5V Extract 1 = +4V Extract 2 = -40V

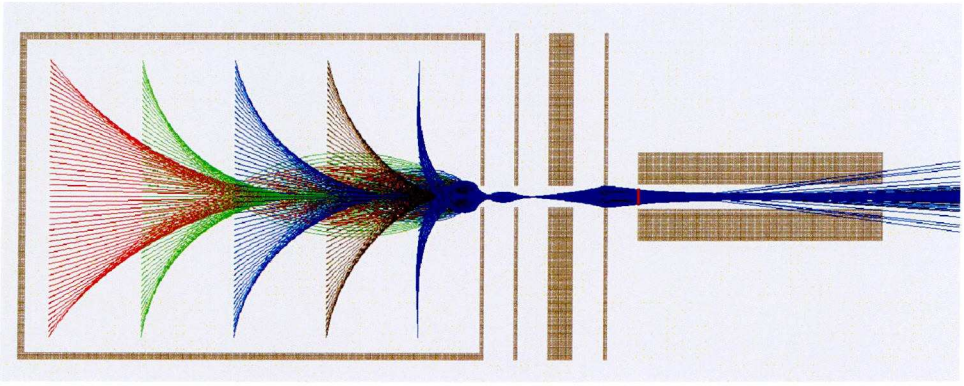

Figure 5: SIMION output showing ion trajectories (rays) and beam profile for Index Number 5 of Table 2.2 (Cage = 0.1mm, Extract1 = 0.1mm, Extract2 = 0.8mm, Earth = 0.1mm) with potentials: Cage = +5V Extract 1 = +4V Extract 2 = -40V

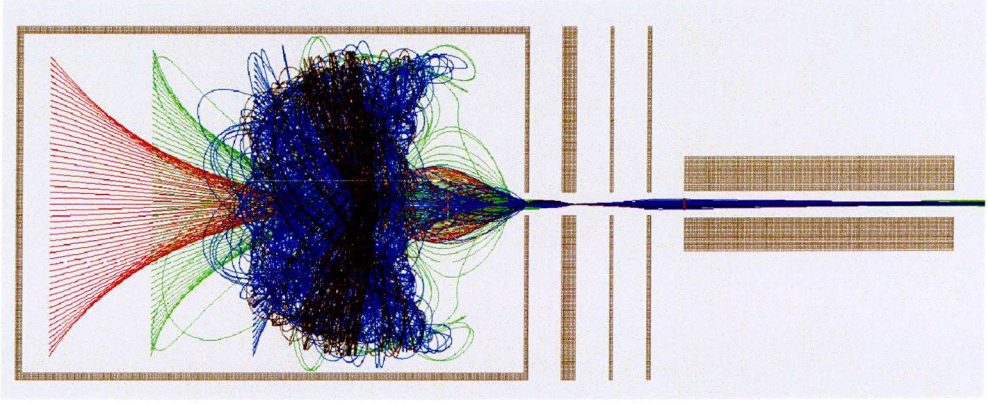

Figure 6: SIMION output showing ion trajectories (rays) and beam profile for Index Number 6 of Table 2.2 (Cage = 0.1mm, Extract1 = 0.4mm, Extract2 = 0.1mm, Earth = 0.1mm) with potentials: Cage = +5V Extract 1 = +4V Extract 2 = -40V

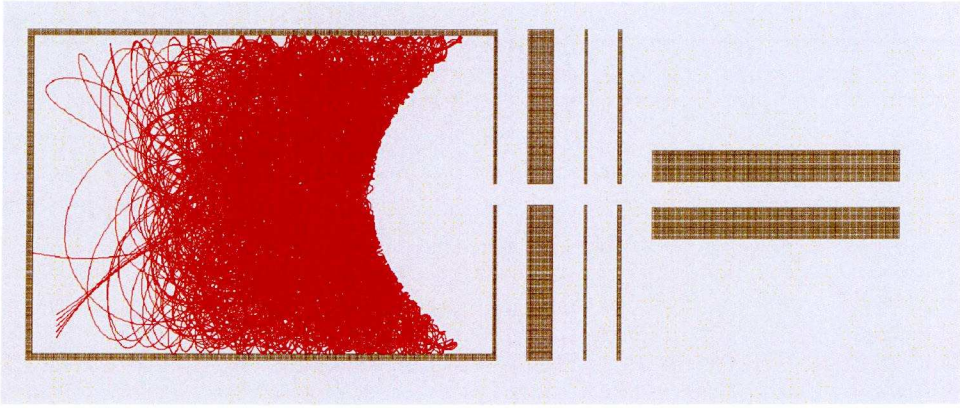

Figure 6: SIMION output showing ion trajectories (rays) and beam profile for Index Number 7 of Table 2.2 (Cage = 0.1mm, Extract1 = 0.8mm, Extract2 = 0.1mm, Earth = 0.1mm) with potentials: Cage = +5V Extract 1 = +4V Extract 2 = -40V

Appendix 3.1 - Specifications for QMS drive ECU and software

1. Mass filter RF and DC drive voltage: U(t) + V(t) where U is a variable DC (Ramp) voltage $U(t) = U_{DC}\, t$ and V is a variable amplitude RF voltage $V(t) = V_{RF} \cos \omega t$

2. V should be a clean sine wave (no excessive harmonics) at frequency fixed in the range f = 6 to 7MHz..
   Variable U/V ratio adjustable in 2 operating zones:
   Zone 1: U_{max} / V_{max} = 0 to 0.35, U = 0 to ±10V, V_{max} = 60V peak to peak (mass range to 200 amu);
   Zone 2: U_{max} / V_{max} = 0.45 to 1.05, U = 0 to ±10V, V_{max} = 20V peak to peak (mass range to 65 amu, but with high resolution),

3. U - Vcosωt and its antiphase -U + Vcosωt are supplied to alternate pairs of electrodes in a quadrupole arrangement.
   Impedance to be driven mostly capacitive (electrode to ground) in range 20-200pF
   Drive voltage to be controlled by a 0-10V DC control voltage ramp so that V_{RF} is swept from 0 to V_{max} in about 200 seconds (programmable)
   Adjustable V offset 0-2V DC (i.e. V does not have to start from 0V) in 100mV steps. Adjustable electrode bias –5 to +5V DC to all electrodes in 1V steps

4. Ion source controller
   Voltage on filament – 65 to –70V (i.e 5V dropped across filament)
   Filament current 0 –3A DC
   Filament electron emission current stable and controllable in range 0.01mA – 5mA in 5 steps (0.01, 0.1, 1 , 2, 5 mA) with overcurrent protection limit
   Cage voltage Vc = 0 – 20V +ve DC (provides current return path for filament emission current monitoring) in 10 steps

Focus voltage Vf1 = 0- 20V +ve DC (no current) in 10 steps

Focus voltage Vf2 = 0- 150V –ve DC (no current) in 10 steps

5. Detector

   Picoammeter capable of detecting ion currents down to 0.01pA supplied to PC

   via 16 bit ADC

   Multiplier output 0, ±500V, ±750V, ±1000V, ±1250V, ±1500V DC voltage (no current)

6. Software

   All the above to be software controllable via a USB link to a PC.

7. Packaging

   To be mounted in a screened metal enclosure on a 3" vacuum flange with attention given to ensure zero interference of picoammeter signal and RF drive voltages (important): example to be made available to copy.

Appendix 3.2 – Plots for 4 plate Ion source characterization.

5eV plots

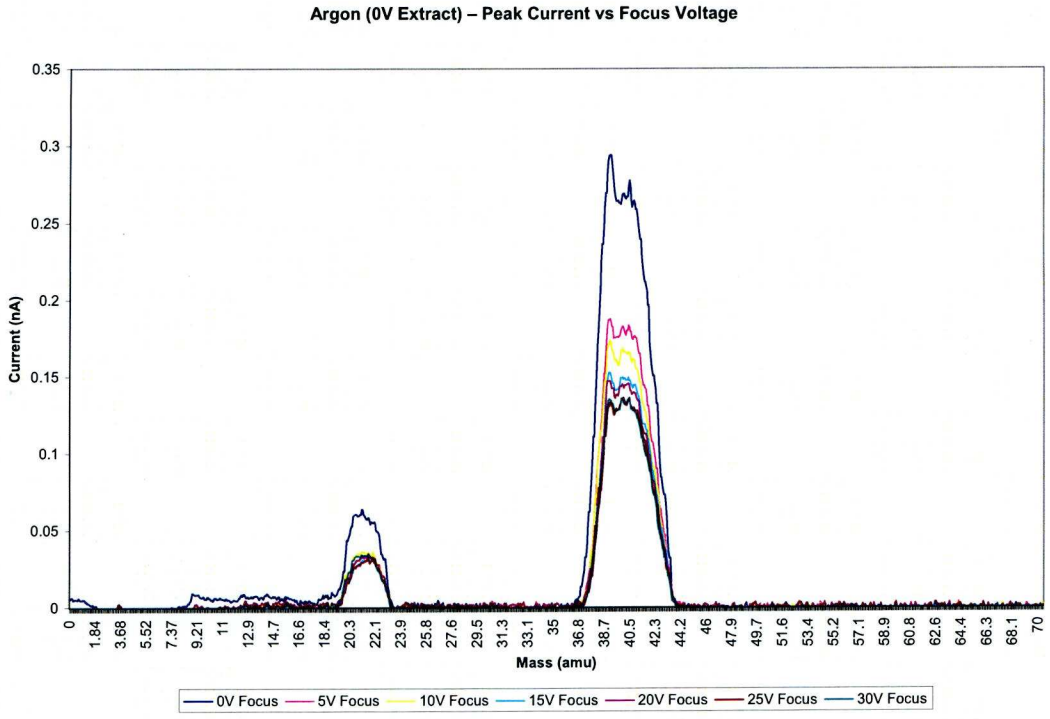

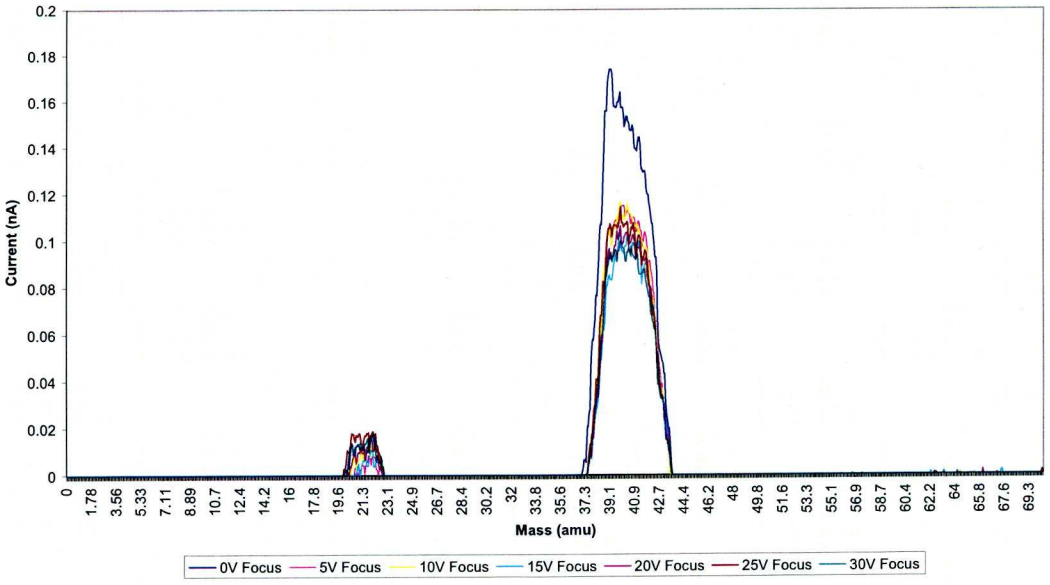

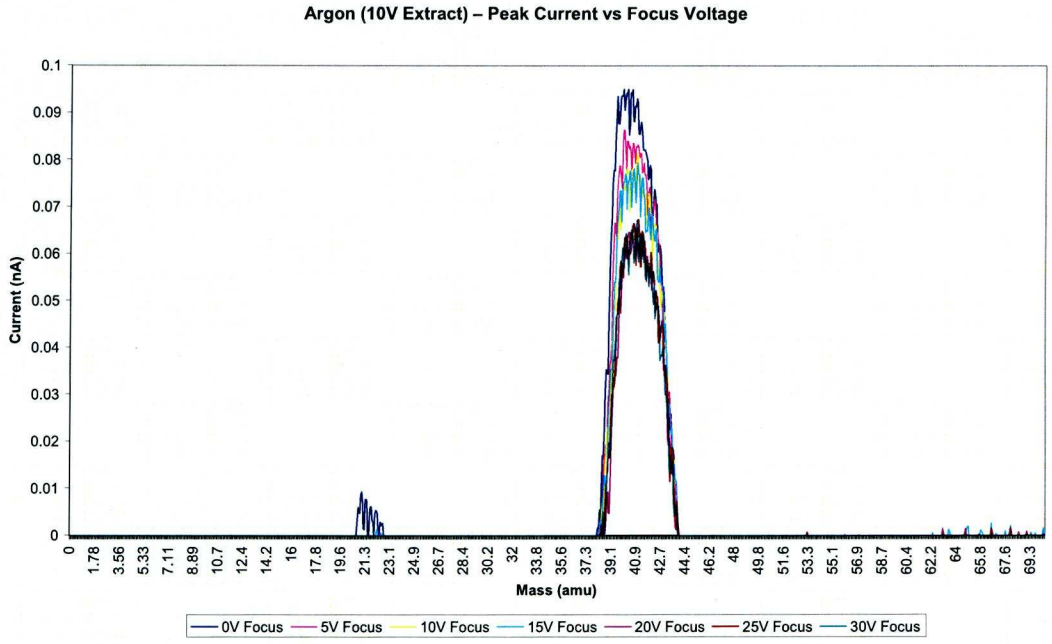
Argon (10V Extract) – Peak Current vs Focus Voltage
Current (nA)
0.1
0.09
0.08
0.07
0.06
0.05
0.04
0.03
0.02
0.01
0
0 1.78 3.56 5.33 7.11 8.89 10.7 12.4 14.2 16 17.8 19.6 21.3 23.1 24.9 26.7 28.4 30.2 32 33.8 35.6 37.3 39.1 40.9 42.7 44.4 46.2 48 49.8 51.6 53.3 55.1 56.9 58.7 60.4 62.2 64 65.8 67.6 69.3
Mass (amu)
0V Focus
5V Focus
10V Focus
15V Focus
20V Focus
25V Focus
30V Focus

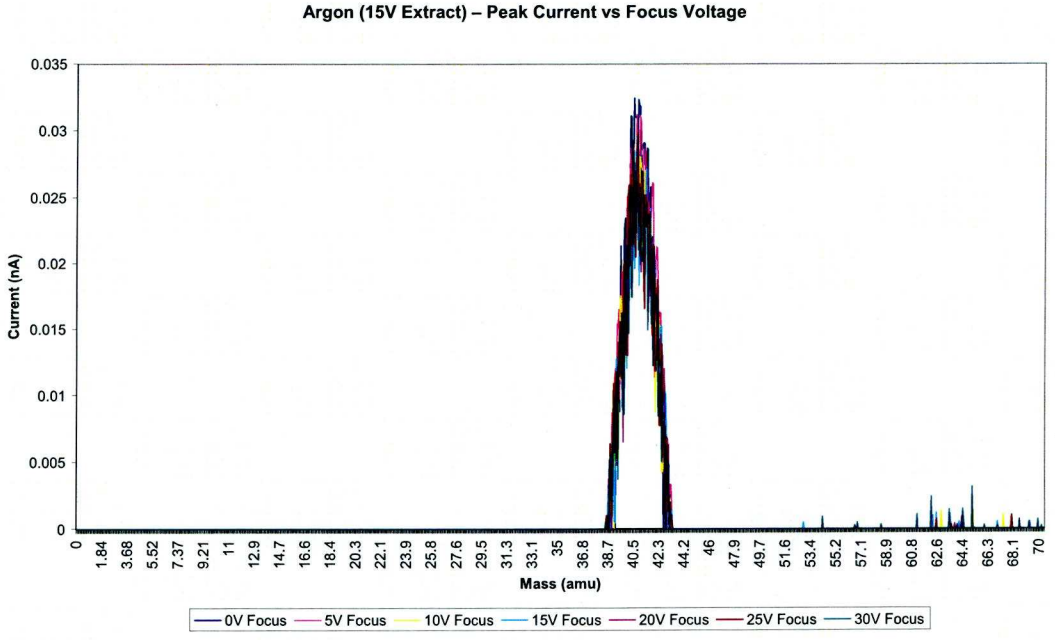
Argon (15V Extract) – Peak Current vs Focus Voltage
Current (nA)
0.035
0.03
0.025
0.02
0.015
0.01
0.005
0
0 1.84 3.68 5.52 7.37 9.21 11 12.9 14.7 16.6 18.4 20.3 22.1 23.9 25.8 27.6 29.5 31.3 33.1 35 36.8 38.7 40.5 42.3 44.2 46 47.9 49.7 51.6 53.4 55.2 57.1 58.9 60.8 62.6 64.4 66.3 68.1 70
Mass (amu)
0V Focus
5V Focus
10V Focus
15V Focus
20V Focus
25V Focus
30V Focus

Argon (20V Extract) – Peak Current vs Focus Voltage

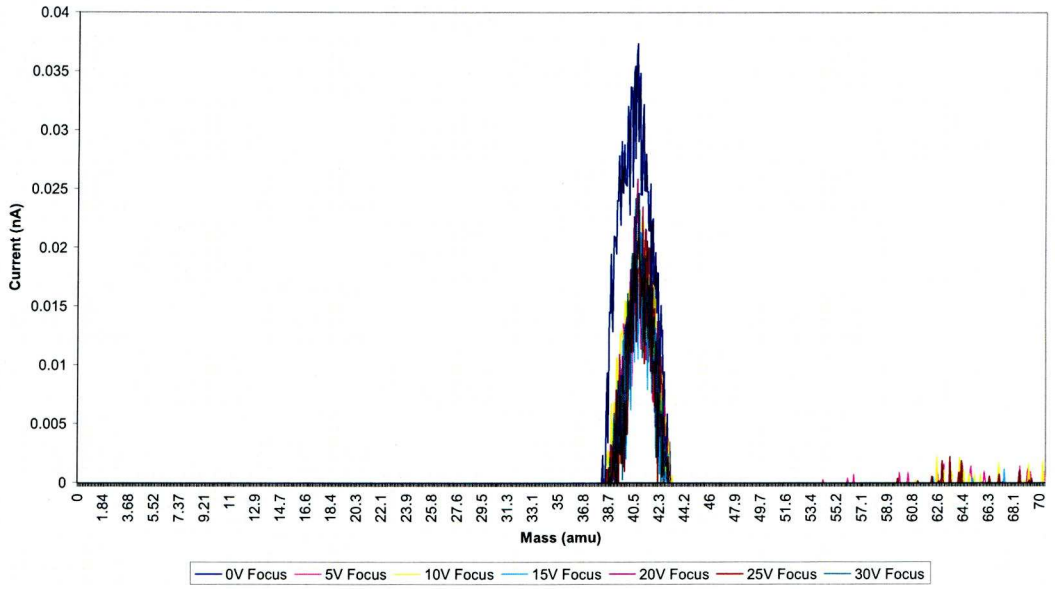

Argon (25V Extract) – Peak Current vs Focus Voltage

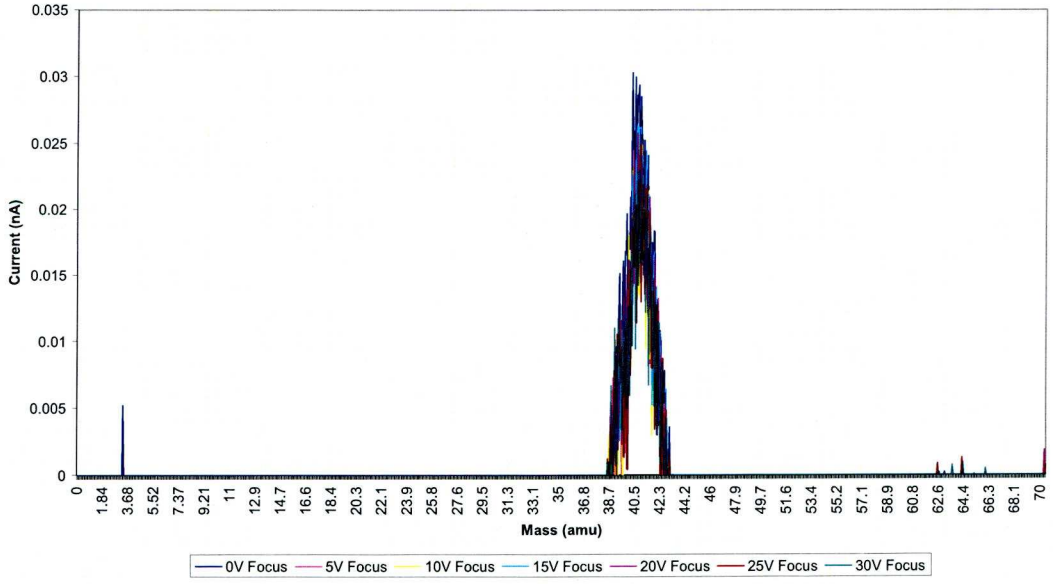

7eV plots

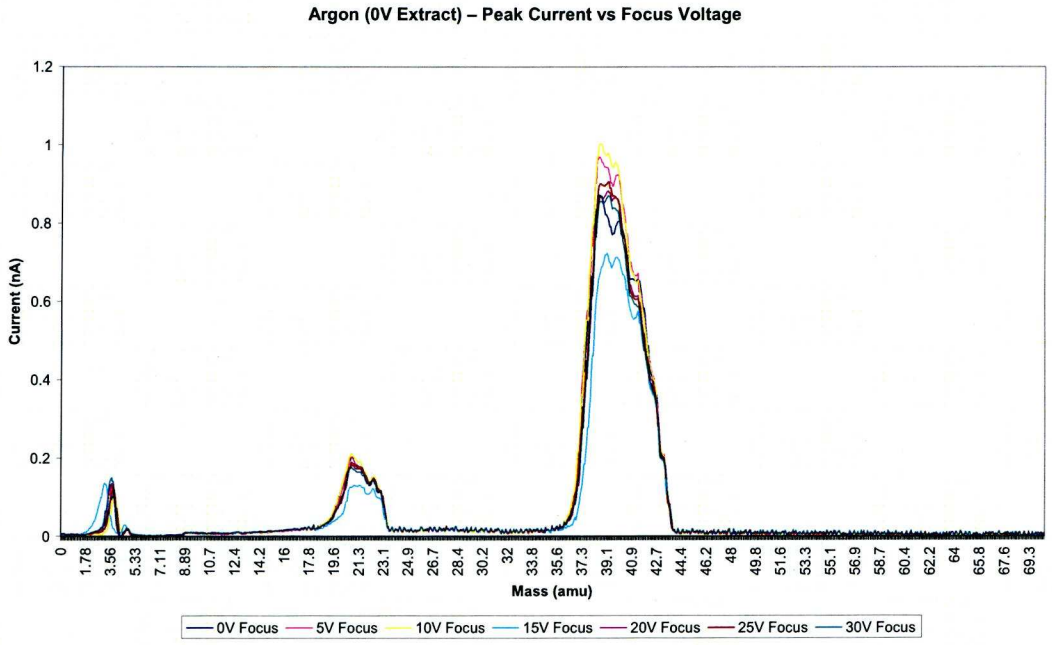
Argon (0V Extract) – Peak Current vs Focus Voltage
Current (nA)
Mass (amu)
0V Focus
5V Focus
10V Focus
15V Focus
20V Focus
25V Focus
30V Focus

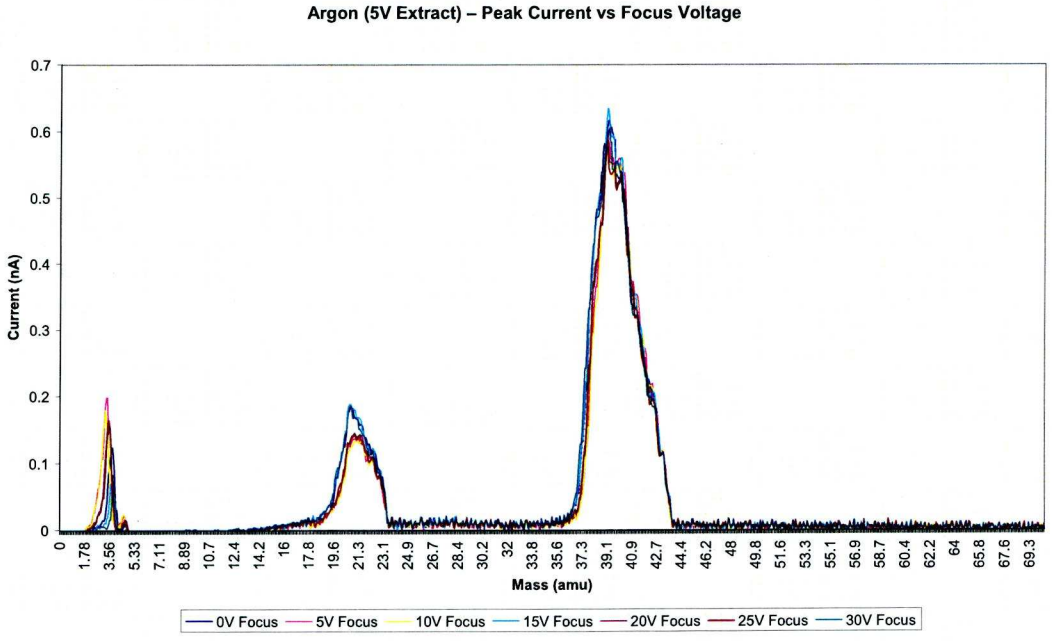
Argon (5V Extract) – Peak Current vs Focus Voltage
Current (nA)
Mass (amu)
0V Focus
5V Focus
10V Focus
15V Focus
20V Focus
25V Focus
30V Focus

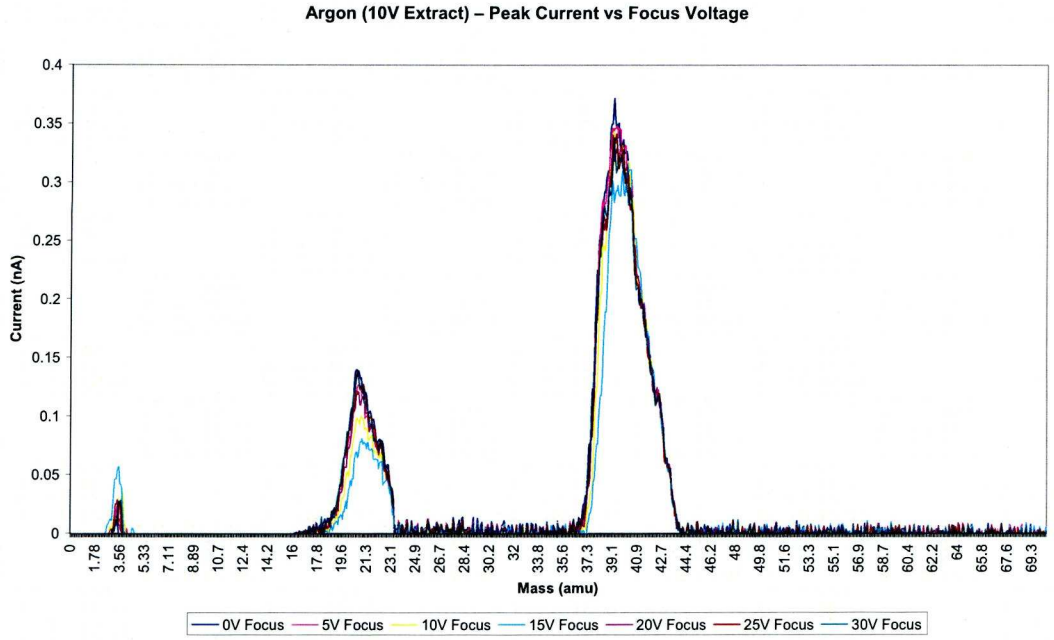
Argon (10V Extract) – Peak Current vs Focus Voltage
Current (nA)
0.4
0.35
0.3
0.25
0.2
0.15
0.1
0.05
0
0 1.78 3.56 5.33 7.11 8.89 10.7 12.4 14.2 16 17.8 19.6 21.3 23.1 24.9 26.7 28.4 30.2 32 33.8 35.6 37.3 39.1 40.9 42.7 44.4 46.2 48 49.8 51.6 53.3 55.1 56.9 58.7 60.4 62.2 64 65.8 67.6 69.3
Mass (amu)
0V Focus
5V Focus
10V Focus
15V Focus
20V Focus
25V Focus
30V Focus

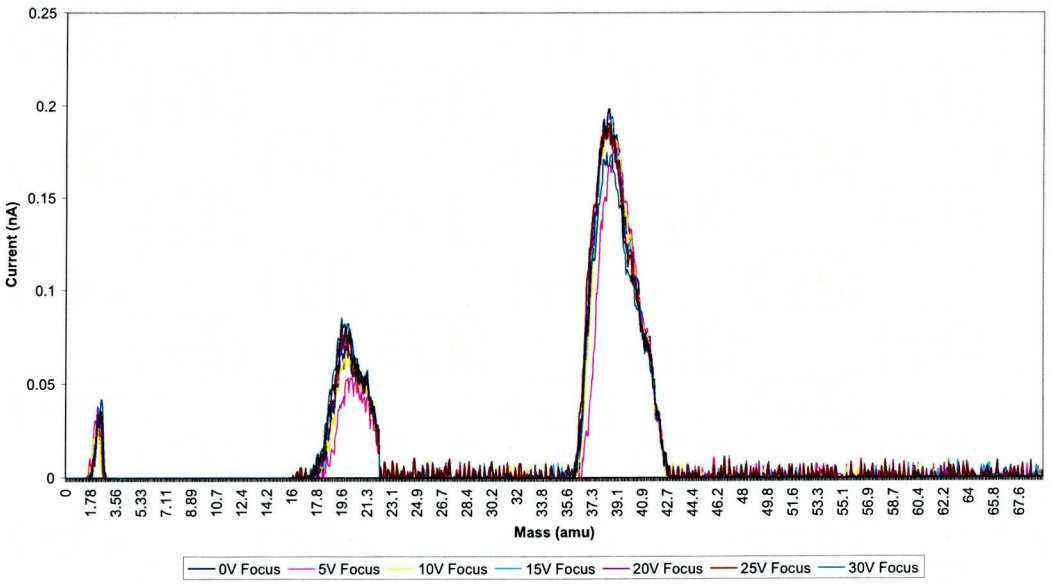
Argon (15V Extract) – Peak Current vs Focus Voltage
Current (nA)
0.25
0.2
0.15
0.1
0.05
0
0 1.78 3.56 5.33 7.11 8.89 10.7 12.4 14.2 16 17.8 19.6 21.3 23.1 24.9 26.7 28.4 30.2 32 33.8 35.6 37.3 39.1 40.9 42.7 44.4 46.2 48 49.8 51.6 53.3 55.1 56.9 58.7 60.4 62.2 64 65.8 67.6
Mass (amu)
0V Focus
5V Focus
10V Focus
15V Focus
20V Focus
25V Focus
30V Focus

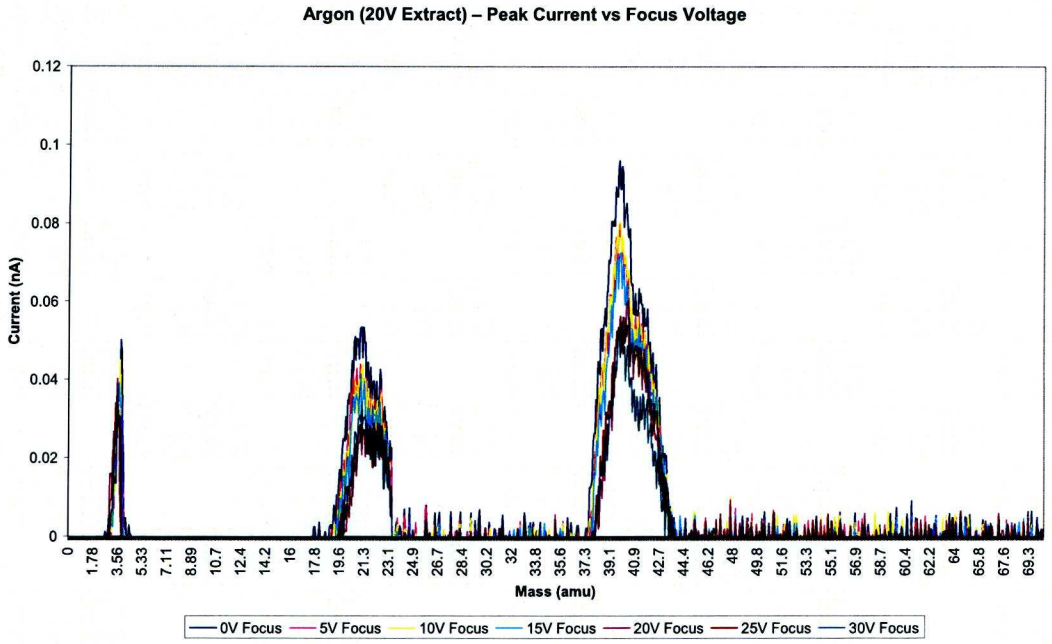
Argon (20V Extract) – Peak Current vs Focus Voltage
Current (nA)
0.12
0.1
0.08
0.06
0.04
0.02
0
0
1.78
3.56
5.33
7.11
8.89
10.7
12.4
14.2
16
17.8
19.6
21.3
23.1
24.9
26.7
28.4
30.2
32
33.8
35.6
37.3
39.1
40.9
42.7
44.4
46.2
48
49.8
51.6
53.3
55.1
56.9
58.7
60.4
62.2
64
65.8
67.6
69.3
Mass (amu)
0V Focus
5V Focus
10V Focus
15V Focus
20V Focus
25V Focus
30V Focus

Appendix 5.1 – MATLAB source code for HBP test.

```
format short g;
curDir=cd

% load the file file
DefaultPath = [ cd '\*.txt'];
[name, path] = uigetfile(DefaultPath,'Load Pre-tablet sample *.txt ');
fullName = fullfile(path, name);    % Full file name including extension
[path, name, ext, version] = fileparts(fullName);
baseName = fullfile(path, [name '.txt']);

[data] = textread(baseName,'%n','delimiter',',','headerlines',2);
data1=data(1:176);
data2=data(177:352);
data3=data(353:528);
data4=data(529:704);
data5=data(705:880);
data6=data(881:1056);

maxdata44=[ max(data1(85:95)), max(data2(85:95)),
max(data3(85:95)),max(data4(85:95)),max(data5(85:95)),max(data6(85:95)), ];
results(1,1)=mean(maxdata44);
results(1,2)= std(maxdata44);

maxdata45=[ max(data1(101:111)), max(data2(101:111)),
max(data3(101:111)),max(data4(101:111)),max(data5(101:111)),max(data6(101:11
1)) ];
results(1,3)=mean(maxdata45);
results(1,4)= std(maxdata45);
```

```
if (results(1,2)/results(1,1)) > 0.1
   disp('Signal Variation! >10% within set')
   else
end

for icount=1:length(maxdata44)
   ratio1(icount)=maxdata45(icount)/maxdata44(icount);
end

results(1,5)=mean(ratio1)

%%%
```

```
maxdata44post=[ max(datapost1(85:95)), max(datapost2(85:95)),
max(datapost3(85:95)),max(datapost4(85:95)),max(datapost5(85:95)),max(datapost
6(85:95)), ];
;

maxdata45post=[ max(datapost1(101:111)), max(datapost2(101:111)),
max(datapost3(101:111)),max(datapost4(101:111)),max(datapost5(101:111)),max(d
atapost6(101:111)) ];


results(2,1)=mean(maxdata44post);
results(2,2)= std(maxdata44post);
results(2,3)=mean(maxdata45post);
results(2,4)= std(maxdata45post);

if (results(2,2)/results(2,1)) > 0.1
   disp('Signal Variation! >10% within set')
else
end

for icount=1:length(maxdata44)
   ratio1(icount)=maxdata45post(icount)/maxdata44post(icount);
end

results(2,5)=mean(ratio1);

disp ( 'mean 44  std dev   mean 45   std dev  44/45')
results

disp('pecentage increase')
```

```
percent_change=(results(2,5)/results(1,5)*100)-100

masses;
offset=0;%1e-10 % prevents negative values in Log plot
figure(151);
hold on;

%semilogy(mass_scale,data1+offset,'g-',mass_scale,data2+offset,'g-
',mass_scale,data3+offset,'g-',);
semilogy(mass_scale,data1/maxdata44(1),'g-',mass_scale,data2/maxdata44(2),'g-
',mass_scale,data3/maxdata44(3),'g-',mass_scale,data4/maxdata44(4),'g-
',mass_scale,data5/maxdata44(5),'g-',mass_scale,data6/maxdata44(6),'g-');
%semilogy(mass_scale,datapost1+offset,'r-',mass_scale,datapost2+offset,'r-
',mass_scale,datapost3+offset,'r-');
semilogy(mass_scale,datapost1/maxdata44post(1),'r-
',mass_scale,datapost2/maxdata44post(2),'r-
',mass_scale,datapost3/maxdata44post(3),'r-
',mass_scale,datapost4/maxdata44post(4),'r-
',mass_scale,datapost5/maxdata44post(5),'r-
',mass_scale,datapost6/maxdata44post(6),'r-');
H=title('Pre (green) Post-(red) Tablet Data');
x1=xlabel('mass scale m/z');
x2=ylabel('signal intensity A');

figure(3);
plot(1:176,data1/maxdata44(1),'g-',1:176,data2/maxdata44(2),'g-
',1:176,data3/maxdata44(3),'g-',1:176,data4/maxdata44(4),'g-
',1:176,data5/maxdata44(5),'g-',1:176,data6/maxdata44(6),'g-');
H=title('check sampling position mass 44=89 and mass 45=105');

figure(151);
```